POLITECNICO DI MILANO

School of Industrial and Information Engineering

Master of Science Degree in Mathematical Engineering

Electromechanical modelling of the human heart in bi-ventricle geometries

---

Submitted by

Luca Azzolin (ID: 854786)

Advisors

Alfio Quarteroni (École Polytechnique Fédérale de Lausanne)
Luca Dedè (Politecnico di Milano)

Co-Advisor

Antonello Gerbi (École Polytechnique Fédérale de Lausanne)

Academic Year 2017-2018

Abstract

Mathematical and numerical modelling of the heart are receiving a growing attention in recent years due to the significant amount of natural deaths caused by cardiac diseases and the considerable cost for the social and healthcare systems. In this thesis, we consider a mathematical and numerical model for cardiac electromechanics, with focus on both the ventricles. We model the propagation of the electrical signal through the monodomain equation and we use the Bueno–Orovio minimal ionic model to capture the main features of the electrophysiology in the myocardial tissue. Since the distribution of the electric signal is dependent on the fibres orientation of the ventricles, we use a Laplace-Dirichlet Rule-Based algorithm to determine the myocardial fibres and sheets configuration in the whole bi-ventricle. Assuming the same mechanical behaviour for both the left and right ventricles, we consider the Holzapfel-Ogden strain energy function for the passive myocardial tissue modelling together with the active strain approach combined with a model for the transmurally heterogeneous thickening of the myocardium. In this thesis, we propose tackling the electromechanical modelling of the bi-ventricle geometry by carefully addressing the systolic phases, which is comprised of two isovolumic stages and ejection; as these phases are not aligned for the ventricles, modelling them is particularly challenging. The coupled electromechanical problem is addressed by means of a monolithic scheme. The numerical discretization consists in Finite Element Method for the spatial discretization and Backward Differentiation Formulas for the time discretization. The non-linear system coming from application of the implicit scheme is solved through the Newton method. A broad range of numerical simulation is carried out in patient-specific bi-ventricle geometries to highlight the most relevant results of both electrophysiology and mechanics and to compare them with physiological data and measurements. We investigate different scenarios, in particular, we highlight the role of the fibres and their impact on the cardiac cycle.

Keywords: heart modelling; electromechanics; coupled problem; monolothic scheme; fibres orientation; cardiac cycle; high performance computing.

Sommario

La modellistica matematica e numerica del cuore sta recentemente ricevendo un'attenzione crescente dato il significativo numero di morti naturali causate da patologie cardiache e il considerevole costo per la società e il sistema sanitario. In questa tesi, noi consideriamo un modello matematico e numerico per l'elettromeccanica cardiaca, con un una particolare attenzione ad entrambi i ventricoli. Modellizziamo la propagazione del segnale elettrico grazie all'equazione del monodominio e usiamo il modello ionico minimale di Bueno–Orovio per catturare le principali caratteristiche dell'elettrofisiologia nel miocardio. Poichè la distribuzione dell'impulso elettrico dipende dall'orientazione delle fibre nei ventricoli, usiamo un algoritmo Laplace-Dirichlet Rule-based per determinare la configurazione delle fibre e dei foglietti del miocardio in tutto il biventricolo. Assumendo lo stesso comportamento meccanico per entrambi i ventricoli sinistro e destro, consideriamo la funzione energia di deformazione di Holzapfel–Ogden per modellizzare il tessuto miocardiaco passivo assieme ad un approccio di sforzo attivo in combinazione con un modello per l'ispessimento transmurale eterogeneo del miocardio. In questa tesi, proponiamo di trattare la modellistica elettromeccanica della geometria del biventricolo dedicandoci in particolare alle fasi sistoliche, che comprendono due stadi isovolumetrici e l'eiezione; poichè queste fasi non sono allineate per i ventricoli, modellizzarle è particolarmente complesso. Il problema accoppiato elettromeccanico è affrontato tramite uno schema monolitico. La discretizzazione numerica consiste nel metodo agli elementi finiti per la discretizzazione spaziale e le formule di differenziazione all'indietro per la discretizzazione temporale. Il sistema non lineare derivante dall'applicazione dello schema implicito è risolto grazie al metodo di Newton. Una vasta gamma di simulazioni numeriche è eseguita su geometrie rappresentanti biventricoli patient-specific per evidenziare i risultati più rilevanti sia riguardo l'elettrofisiologia sia riguardo la meccanica e per confrontare tali risultati con misurazioni e dati fisiologici. Investighiamo scenari differenti, in particolare, evidenziamo il ruolo delle fibre e il loro impatto nel ciclo cardiaco.

Parole chiave: modellistica del cuore; elettromeccanica; problema accoppiato; schema monolitico; orientazione delle fibre; ciclo cardiaco; calcolo ad alte prestazioni.

Acknowledgements

In the first place, I would like to my thesis advisors, Prof. Alfio Quarteroni and Prof. Luca Dedè, for the outstanding opportunity they gave me to convert into work my passions. Especially, I want to say thank you to Prof. Quarteroni for accepting me in the framework of the ERC project iHeart and for allowing me to spend some months at the École Polytechnique Fédérale de Lausanne (EPFL) in which I had the possibility to meet a great team of colleagues. It has been both an honour and a pleasure to be part of this team. Prof. Dedè has always been by my side in this hard period, with a lot of patience and enthusiasm he supported me and my work at all stages and at all hours of the day and, sometimes, of the night. Both of them encouraged me providing plenty of advices and stimulated in me continuous interest in what I was doing. I am really grateful to them and I am glad of having chosen them to end my academic path.

I would like to thank, the nearly doctor, Antonello Gerbi, I have to admit that all I did in these months would not have been possible without his guidance, I would be still stuck in compiling LifeV. We struggled together since the first day and if I had some problem I had always known in who I could count on. The fact of working at the same time in similar topics fed reciprocal enthusiasm and discussions on the subject. From this experience I leave with a friend, more than a colleague.

I would also to thank all the Chair of Modelling and Scientific Computing (CMCS) team in Lausanne for having introduced me in the PhD world, for the lifev-coffee time, for the coffee-breaks, for the various groups in Telegram, for the help and support given me when needed.

Several other people contributed to the achievements of this thesis. In first place, I wish to thank Dr. Jason Bayer from The Johns Hopkins University, Baltimore, for the unexpected kindness and for the collaboration we had for the implementation of the fibres configuration code. Secondly, Prof. Aine Kelly from Trinity College Dublin, for providing me the reference in which to find the irretrievable Wiggers diagram of both the ventricles. I would like to thank MER Simone Deparis for the support he gave me regarding the LifeV library and for his grant to send my simulation on the Swiss National Supercomputing Centre (CSCS). I also gratefully acknowledge the CSCS for providing the CPU resources for the numerical simulations under project ID s796.

I wish to thank the girls who put a roof over my head in Lausanne, without Marie, Luisa, Jordane and Natacha, my months at the Epfl would surely have been less hilarious and interesting, we spent fantastic moments and I sincerely hope to meet you again in the future.

I would like to thank all the colleagues and friends I have met all over the world for the cheerful moments we have spent together, sometimes a smile can be the only thing I need.

A special thank goes to my family, mamma Paola, Sergio and Alberto, for their everlasting support and inspiration, their monumental patience and presence, their guidance and advices. This piece of work is also dedicated to all of you.

Contents

List of Figures

List of Tables

1 Introduction

The heart plays the crucial role of pumping the blood through the circulatory system to provide all sort of vital substances to the cells. Moreover, cardiovascular diseases represent one of the most important problems in public health, affecting millions of people each year (the World Health Organization, cf. http://www.who.int, gave an estimate of 8.76 million deaths in 2015). A progress in the experimental, theoretical, and computational understanding of the cardiac function may be of great help in the development and improvement of novel therapies and diagnostic approaches. However, many difficulties arise when approaching the modelling of cardiac function (including e.g. the mismatch of model parameters and spatio-temporal scales, associated to the extremely tough task of retrieving in vivo measurements from the tissue) and when trying to simulate their joint electromechanical behaviour as a coupled multi-physics and multi-scale problem [40]. Advances in the fields of experimental and theoretical biology, physics, computer science and clinical data feed, as inputs, the mathematical models, allowing numerical simulations in patient-specific framework [28, 60].

The mathematical modelling of the heart involves several challenges intrinsically related to the complexity of its function [22, 26, 35]. At the moment, several cardiac modelling studies at the whole heart level are still restricted to simulating particular components, such as, e.g., the electrophysiology or the electromechanics.

The physiological function of the heart can be summarized as follows: an electric potential propagates across the membrane of the heart muscle cells (cardiomyocytes) and induces complex biochemical reactions inside the cytosol that release calcium from the sarcoplasmic reticulum, resulting in the generation of force within the sarcomeres (the basic contractile units within cardiac muscle cells), finally causing the individual cells to contract and the muscle to deform. The contraction of the muscle yields a rapid increase of pressure inside the ventricular cavities, which allows the heart valves to open and close in careful sequence and induces the periodic filling and ejection of blood from the ventricles and the atria [33, 76, 82, 83, 102, 107, 108]. This physiological process is intrinsically of multi-scale nature and therefore the equations that govern each mechanism will combine terms of different length/time scales. As a matter of fact, ion channels on the cell membrane and the excitation-contraction mechanism are typically modelled through systems of ODEs to be solved for each individual cell (length scales of µm) and can have time scales of 10^{-4} ms. On the other hand, the description of fluid dynamics and solid mechanics of the tissue at the organ level (length scales of cm) and of the propagation of the electrical signal (monodomain) are translated in non-linear partial differential equations of either parabolic or parabolic-hyperbolic type with time scales of 0.1 ms (for the fluid dynamics and solid mechanics) [82].

In this thesis, we propose an electromechanical model for both the left and right ventricles, which extends the model presented in [38] for the left ventricle only. We use state-of-the-art models in passive myocardial tissue modelling (the Holzapfel-Ogden model [48]) together with the active strain approach [3, 4] in combination with a recently proposed model for the transmurally heterogeneous thickening of the myocardium [10];

the latter is used in the integrated electromechanics context for both the left (LV) and the right (RV) human ventricles. Once established, the active mechanics is coupled with the electrophysiology through a model describing the shortening of the myocardial fibres [94], which is in turn triggered by a change in the ionic concentrations in the cardiac cells. We use a Laplace-Dirichlet Rule-Based algorithm [11] to reproduce the ventricles fibres and sheets configuration. We will discuss about the great importance of choosing their orientation. In this thesis, we propose to address the electromechanical modelling of the bi-ventricle by deeply focusing on the systolic phases, which is constituted of two isovolumic stages and ejection; modelling them will be particularly challenging, since these phases are not synchronous for the ventricles.

From the numerical point of view, we discretize in space the models by means of the Finite Element Method (FEM) with piecewise linear polynomials of degree one ($\mathbb{P}^1$), while the time discretization is carried out with Backward Differentiation Formulas (BDFs) of order 2 [84]. We then formulate a monolithic algebraic problem to enforce the coupling and interface conditions among the single core cardiac models for both the LV and RV, contrarily to several works where the electrophysiology and the mechanics problems are solved with a staggered approach [7, 8, 23, 44, 58, 91, 115]. It is however known that, in general, staggered approaches do not guarantee unconditional stability, similarly to the case of segregated algorithms [21]. In this work we successfully use a monolithic scheme for the simulation of the isovolumic contraction and the ventricular ejection phases of an heartbeat, by realizing pressure-volume loops patient-specific bi-ventricles. The fluid-structure interaction (FSI) between the blood contained in each chamber and the endocardial wall is addressed through a simple 0D model (spatially independent) for the pressure variable tailored for the different phases of the heartbeat [31, 91, 115]; a prestress technique is also applied to both the patient–specific LV and RV in order to estimate the internal stresses of the myocardium at the initial time [51, 109], i.e. in the reference configuration of the muscle. It is relevant to notice that at telediastole the endocardial pressure is different in the LV and RV chambers, thus this method has to be able to compute the response of the tissue to the fluid in the corresponding chamber. We solve the large, sparse block monolithic linear system arising from the approximation of the continuous model by means of the GMRES method [95] and, in order to speed–up the convergence of the linear solver, we employ a preconditioner based on the one developed in [38] for the electromechanics problem in the LV. This preconditioning strategy is based on the factorization of a block Gauss–Seidel preconditioner which exposes the multiphysics nature of the integrated problem, thus allowing to adapt its action on each single factor of the preconditioner. All the solvers are implemented in the open source finite element library LifeV (www.lifev.org).

The simulations are carried out on two different bi-ventricle geometries taken from a patient-specific full heart atlas. On each of them, a broad range of tests is performed to determine, on one hand, the influence of the fibres and sheets orientation on the mechanical behaviour, and on the other hand, the impact of the most characteristic parameters belonging to the models on the pressure-volume diagram. Finally, the numerical results are compared against physiological data and clinical measurements.

The thesis is organized as follows: at the beginning in Chapter 2 we briefly present the cardiac physiology, in Chapter 3 we introduce the mathematical models for the electrophysiology, the mechanics and the activation of the myocardium; we then integrate

them thus obtaining a continuous integrated model. In Chapter 4 we carry on the space and time numerical approximations of the single core models projecting them in a finite discrete space; in Section 4.7 we introduce the characteristics of the cardiac cycle illustrating the various phases performed by the ventricles composing a single heartbeat, in Section 5.2 we describe the method used to generate the bi-ventricle's fibres and sheets. In Chapter 6 we report and discuss the numerical results obtained with the proposed methods, subdividing in electrophysiology (Section 6.2) and mechanical results (Section 6.3). Finally we draw our conclusions in Chapter 7, suggesting future improvements.

2 Overview of cardiac physiology

The human heart is an organ that pumps blood throughout the body via the circulatory system, supplying oxygen and nutrients to the tissues and removing carbon dioxide and other leavings. This task is accomplished efficiently through a complex regulatory system that varies the cardiac output in response to experienced changes in the physiological conditions such as stress, physical exercise, and illness. The healthy human heart maintains a pace of roughly 60–100 beats per minute and achieves a cardiac output between 5-6 litres of blood per minute for healthy adults. Unlike skeletal muscle in the limbs, the highly specialized muscle tissue of the heart requires a constant supply of oxygen itself and may be easily damaged (infarcted) if the supply of oxygen is even temporarily reduced, but does not grow tired under stress.

The human heart has four chambers: two upper chambers (the atria) and two lower ones (the ventricles). The right atrium and right ventricle together make up the "right heart", and the left atrium and left ventricle make up the "left heart". A wall of muscle called the septum separates the two sides of the heart (see Figure 2.1). A double-walled sac called the pericardium encases the heart, which serves to protect the heart and anchor it inside the chest. The heart's outer wall consists of three layers. The outermost wall layer, or epicardium, is the inner wall of the pericardium. The middle layer, or myocardium, contains the muscle that contracts. The inner layer, or endocardium, is the lining that contacts the blood.

The tricuspid valve and the mitral valve make up the atrioventricular (AV) valves, which connect the atria and the ventricles. The pulmonary semi-lunar valve separates the right ventricle from the pulmonary artery, and the aortic valve separates the left ventricle from the aorta. The heartstrings, or chordae tendinae, anchor the valves to heart muscles. The sinoatrial node produces the electrical pulses that drive heart contractions [34].

The heart pumps blood through two pathways: the pulmonary circuit and the systemic circuit. In the pulmonary circuit, deoxygenated blood leaves the right ventricle of the heart via the pulmonary artery and travels to the lungs, then returns as oxygenated blood to the left atrium of the heart via the pulmonary vein. In the systemic circuit, oxygenated blood leaves the body via the left ventricle to the aorta, and from there enters the arteries and capillaries where it supplies the body's tissues with oxygen. Deoxygenated blood returns via veins to the venae cavae, re-entering the heart's right atrium.

The ventricles of the heart receive the blood from the atria and pump it to the entire body. During the diastole phase of the cardiac cycle, the atria and ventricles are relaxed and the heart fills with blood. During the systole phase, the ventricles contract pumping blood to the major arteries (pulmonary and aorta). The heart valves open and close to direct the flow of blood between the heart chambers and between the ventricles and major arteries. Papillary muscles in the ventricle walls control the opening and closing of the tricuspid valve and mitral valve.

- Right ventricle: Receives blood from the right atrium and pumps it to the main pulmonary artery. Blood passes from the right atrium through the tricuspid valve into the right ventricle. Blood is then forced into the main pulmonary artery as the
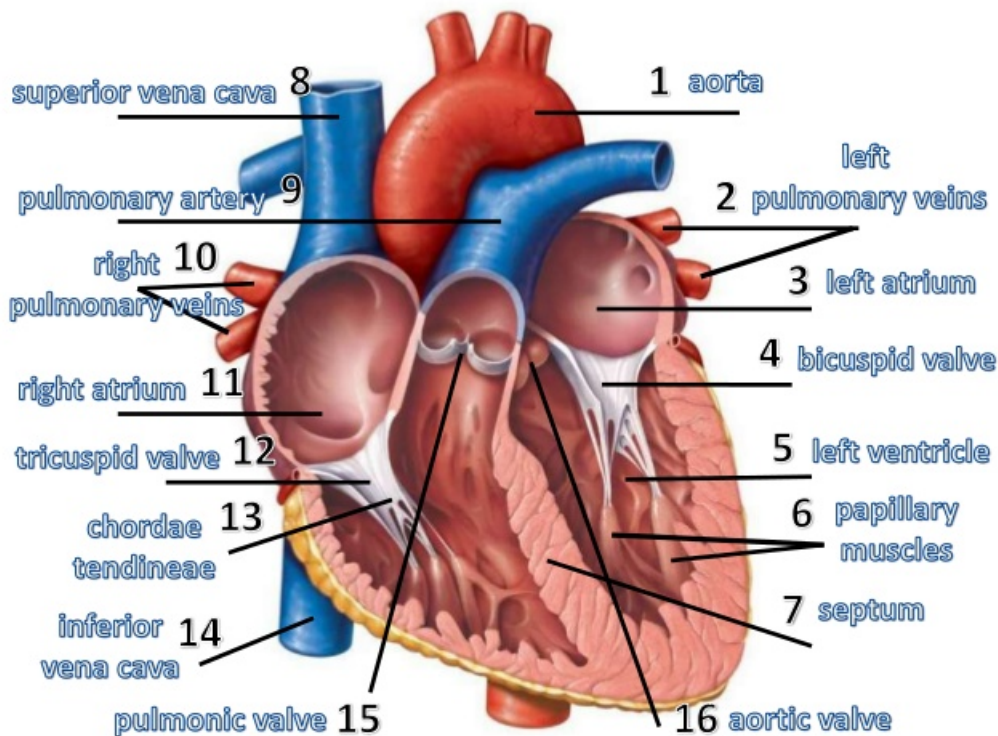
Figure 2.1: Human heart. Image taken from http://anatomyorgan.com/.

ventricles contract and pulmonary valve opens. The pulmonary artery extends from the right ventricle and branches into left and right pulmonary arteries. These arteries extend to the lungs. Here, oxygen-poor blood picks up oxygen and is returned to the heart via the pulmonary veins.

- Left ventricle: Receives blood from the left atrium and pumps it to the aorta. Blood returning to the heart from the lungs enters the left atrium and passes through the mitral valve to the left ventricle. Blood in the left ventricle is then pumped to the aorta as the ventricles contract and the aortic valve opens. The aorta carries and distributes oxygen-rich blood to the rest of the body.

2.1 Structure and mechanical function of cardiac tissue

The heart has a three-layered wall composed of connective tissue, endothelium, and cardiac muscle. It is the muscular middle layer termed as myocardium that enables the heart to contract. The majority of cardiac tissue volume is occupied by cardiomyocytes. These are striated muscle cells specialized for the function of the heart. The cardiomyocytes are joined one to the other in linear arrays by intercalated discs. Being muscle cells means that they are excitable cells (see [55]). The gap junctions between individual cardiomyocytes permit an electrical potential to travel on the cellular membranes from cell to cell similarly if slightly more slowly than in other cells, such as nerve cells. Muscle cells are embedded in a fibrous extracellular matrix formed mainly of collagen protein
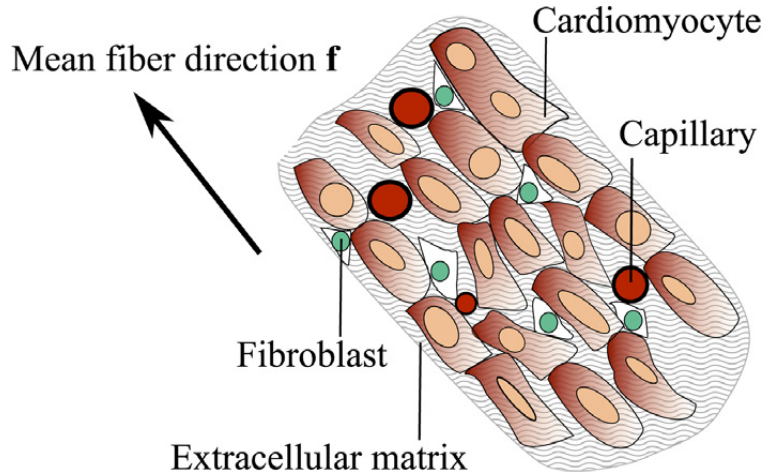
Figure 2.2: Schematic representation of the arrangement of cardiomyocytes in the extracellular matrix synthesized by the fibroblasts. The cardiomyocytes are locally arranged in linear arrays with similar orientation. A network of capillaries perfuses the cardiomyocytes. Image taken from [82].

that is constantly synthesized by cardiac fibroblast cells. These are the most numerous cells in the heart tissue and their task is to remodel the extracellular matrix in response to mechanical strain and external damage. Together they give rise to a fibre-reinforced structure where the cardiomyocytes are arranged in layers of laminar sheetlets. In addition, cardiac tissue contains vascular smooth muscle cells in the intramyocardial coronary arterioles and venules, Purkinje fibres that deliver the electrical signal from the ventricles' natural pacemaker to the muscle, and endothelial cells on the inner surface of the heart called the endocardium. A thin layer of connective tissue and fat, called epicardium, covers the exterior surface of the heart. Moreover, there exists a network of cardiomyocytes joined by intercalated discs, called cardiac syncytium (and divided between an atrial and a ventricular syncytium) that allows the fast propagation of electrical impulses, together with a synchronous contraction of the tissue and cells [55]. A schematic arrangement of myocardial cells is shown in Figure 2.2.

We use the word fibres to indicate the organization of the myocardial cells, which can be idealized as cylindrical objects with radius about a tenth of their longitudinal extension. Their longitudinal shape and the fact that adjacent cells tend to be oriented in roughly the same direction allows us to define the local orientation of the cells, the fibre direction. In most computational models the fact of taking into account individual cells to describe macroscopic behaviour will be computationally too heavy, since the enormous number of degrees of freedom (remember that we have an average of 6 million cells in a cm^2). As a consequence, from now on, we have to think of the fibres direction as the average myocardial cells orientation in a sufficiently small control volume, this technique is called homogenization. As in any muscle, both the passive and active mechanical properties of the tissue are defined following the direction along which fibres are aligned. Although the complex muscular architecture of the ventricles has been studied for centuries, only in the last fifty years has a comprehensive description of the macroscopic morphological structure of the cardiac muscle emerged. From these studies, it emerges that both ventricles are formed by a single bundle of fibres, the Ventricular Myocardial Band (VMB), twisted into
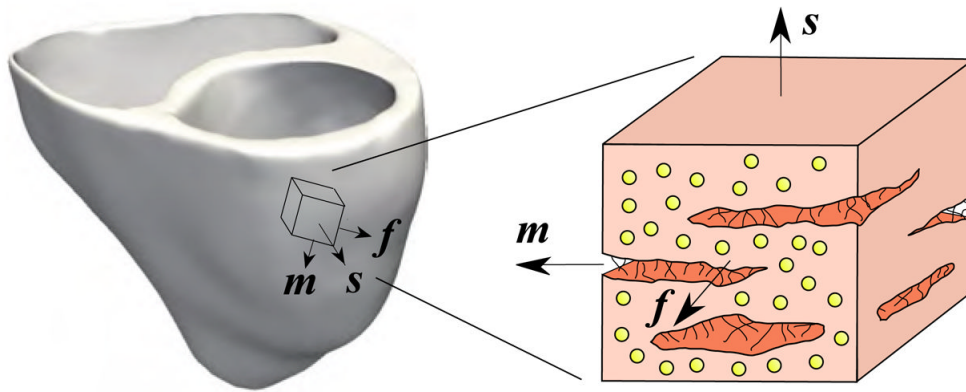
Figure 2.3: Characteristic microstructure of the human heart. Fibre directions f vary transmurally from approximately $-70°$ in the epicardium, the outer wall, to $+80°$ in the endocardium, the inner wall. fibre vectors f and sheet vectors m locally span the sheet plane, with the sheet plane normal s pointing outwards, approximately orthogonal to the epicardial wall. Image taken from [123].
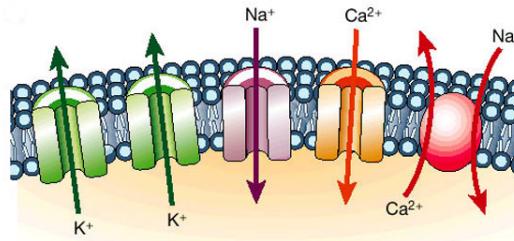
Figure 2.4: Ionic channel in which we have a continuous exchange of Na^+, K^+ and Ca^{2+}. Image taken from https://www.nature.com/.

a helicoidal configuration with two spiral turns [6, 37, 111]. Measurements of Streeter [105] showed a transmural variation of the fibre direction ranging from about $-70°$ in the short-axis plane at the outer ventricular surface, the epicardium, to approximately $+80°$ at the inner part of the wall, the endocardium as we can see in Figure 2.3.

2.2   Electrophysiology and cardiac action potential

Cardiac pacing is driven by the sinoatrial node (located at the right atrium of the heart), a natural pacemaker that discharges electrical signals into the heart's conduction system at varying periods of pacing depending on the level of blood flow required to supply oxygen to the organs. These signals travel through the atria into the atrioventricular node, where a brief delay permits the atria to contract first before the signal enters the ventricular fast conduction system through the left and right bundle branches, finally travelling through the specialized conduction network (highly conductive specialized muscle cells) and junctions into the ventricular muscles. In the cardiac muscle the electrical potential travels more slowly along the cell membranes, opening voltage-sensitive protein channels (see Figure 2.4) and allowing positively charged ions to enter the cells, causing
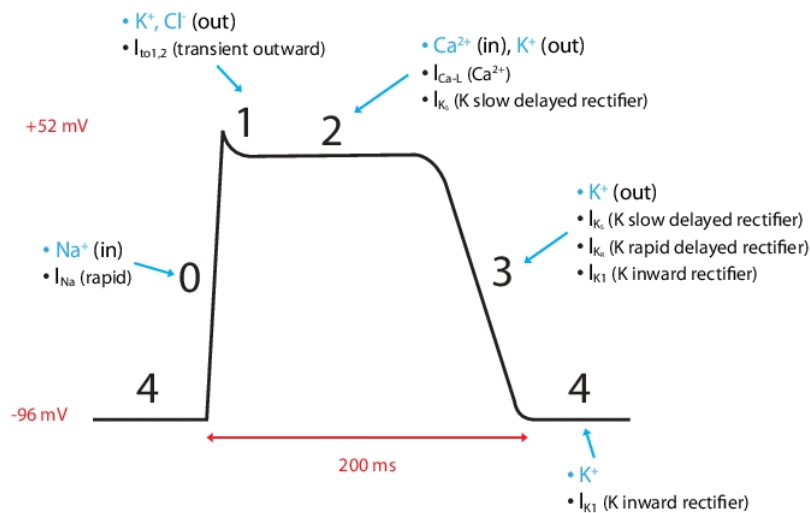
Figure 2.5: Relation between cardiac action potential and ion channel currents. Image taken from https://en.wikipedia.org/wiki/Ventricular_action_potential.

them to become depolarized. Once the entire muscle has been depolarized from its resting potential a slow process of repolarization begins, after which the muscle is ready to contract again. An action potential is formed.

In electrocardiography, the ventricular cardiomyocyte membrane potential is about -90 mV at rest, which is close to the potassium reversal potential. When an action potential is generated, the membrane potential rises above this level in four distinct phases (Figure 2.5). The beginning of the action potential, phase 0, specialized membrane proteins (voltage-gated sodium channels) in the cell membrane selectively allow sodium ions to enter the cell. This causes the membrane potential to rise at a rate of about 300 V/s. As the membrane voltage rises (to about 50 mV) sodium channels close due to a process called inactivation.

Na^+ inactivation comes with slowly activating Ca^{2+} channels at the same time as a few fast K^+ channels open. There is a balance between the outward flow of K^+ and the inward flow of Ca^{2+} causing a plateau. The delayed opening of more Ca^{2+}-activated K^+ channels, which are activated by build-up of Ca^{2+} in the sarcoplasm, while the Ca^{2+} channels close, ends the plateau. This leads to repolarisation.

The depolarization of the membrane allows calcium channels to open as well. As sodium channels close calcium provides current to maintain the potential around 20 mV. The plateau lasts on the order of 150 ms. At the time that calcium channels are getting activated, channels that mediate the transient outward potassium current open as well. This outward potassium current causes a small dip in membrane potential shortly after depolarization. This current is observed in human and dog action potentials, but not in guinea pig action potentials.

Repolarization is accomplished by channels that open slowly and are mostly activated at the end of the action potential (slow delayed-rectifier channels), and channels that open quickly but are inactivated until the end of the action potential (rapid delayed rectifier channels). Fast delayed rectifier channels open quickly but are shut by inactivation at high membrane potentials. As the membrane voltage begins to drop the channels recover

8
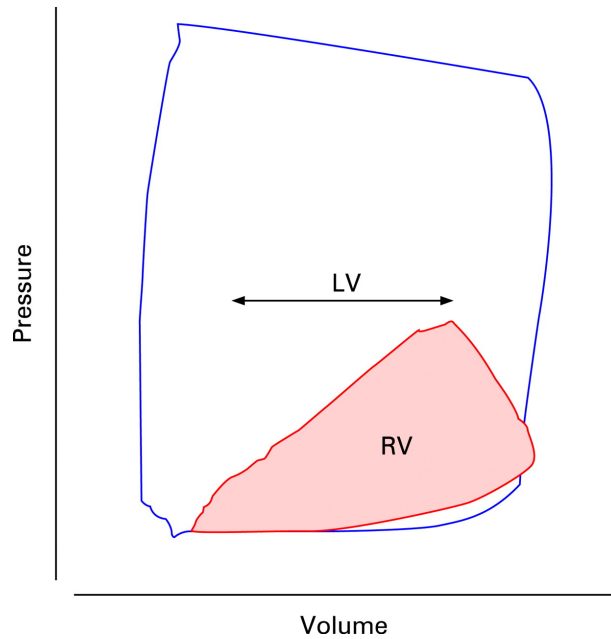
Figure 2.6: P-V loop of right and left ventricles. Image taken from [100].

from inactivation and carry current.

2.3 Electromechanics

Unlike the left ventricle (LV), the right ventricle (RV) has received little attention so far in terms of the detailed characterisation of its function. Accurate quantitative evaluation of the RV function has been limited by its complex structural geometry and contraction pattern. More recently, the development of tomographic imaging techniques such as computed tomography, magnetic resonance imaging and acoustic echocardiography, conductance ventriculography and sonomicrometry have allowed to estimate both the RV and LV volumes and pressure-volume (pV) loop (see Fig. 2.6), which represents the evolution of these two variables during a single heartbeat.

The period of time that begins with contraction of the atria and ends with ventricular relaxation is known as the cardiac cycle. The period of contraction that the heart undergoes while it pumps blood into circulation is called systole. The period of relaxation that occurs as the chambers fill with blood is called diastole. Both the atria and ventricles undergo systole and diastole, and it is essential that these components be carefully regulated and coordinated to ensure blood is pumped efficiently to the body. Briefly, during systole, the ventricles contract, pumping blood through the body. During diastole, the ventricles relax and fill with blood again.

- The left ventricle receives oxygenated blood from the left atrium via the mitral valve and pumps it through the aorta via the aortic valve, into the systemic circulation. The left ventricular muscle must relax and contract quickly and be able to increase or lower its pumping capacity under the control of the nervous system. In the diastolic phase, it has to relax very quickly after each contraction and it proceed to be filled with the oxygenated blood flowing from the pulmonary veins. Likewise in
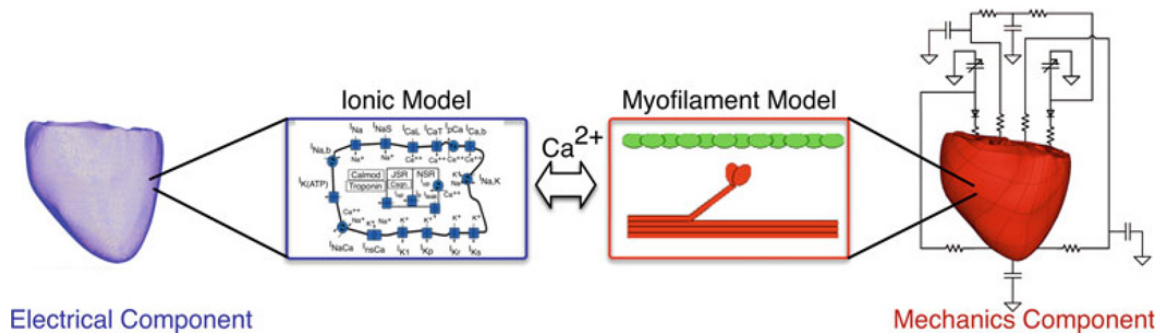
Figure 2.7: Relation between electrical and mechanics components. Image taken from [43].

the systolic phase, the left ventricle must contract rapidly and forcibly to pump this blood into the aorta, overcoming the much higher aortic pressure. The extra pressure exerted is also needed to stretch the aorta and other arteries to accommodate the increase in blood volume;

• The right ventricle receives deoxygenated blood from the right atrium via the tricuspid valve and pumps it into the pulmonary artery via the pulmonary valve, into the pulmonary circulation.

Multi-scale computational models of the ventricular electromechanics have to be capable to simulate both the electrical and the mechanical activity of the ventricles. Briefly, as a depolarization wave propagates through the heart, calcium is released from the myocyte intracellular stores. Calcium then is the responsible of active tension development and, as a consequence, deformation of the ventricles. A schematic diagram is present in Fig. 2.7. The simulation of cardiac contraction entails the simultaneous solution of the ionic model and myofilaments model equations with those representing passive cardiac mechanics over the volume of the heart. In the cardiac modelling community, models in which the electrical physiology is coupled with the mechanical behaviour are still an exception rather than the common rule [112]. The effect of the electrochemical system on the mechanics is the evident active contraction while the so-called mechanoelectrical feedback influences the speed of propagation of the traveling pulse. At the electrophysiology level, it consists in considering the bidomain equations in a deforming medium as well as considering that some ionic channels opening is regulated by stretching. At the sarcomere level, the generation of the power stroke is strongly dependent on the myofilaments overlap and, therefore, it depends on the mechanical strains. An example of electromechanical coupling that only considers geometrical effects is reported in [68]. Other studies have focused on the effects of stretch activated channels [113]. Still, the effects of strains on wave propagation and conduction velocities is poorly understood. Contrasting results have been reported where measured conduction velocities had greater, equal or even smaller magnitudes [106]. In [121], the monodomain model was also coupled with a four state myofilaments activation model to describe cellular contraction. Recently, further efforts have been made to couple the ionic models with myofilaments models [112]. Still, only a few groups are currently using such models mainly due to the difficult accessibility from other communities. From the numerical point of view, usually electromechanical coupling has been achieved by segregated algorithms, but recent studies have reported numerical instabilities [69, 75] and fully implicit solvers have been proposed [44]. While

efficient solvers have been developed for both electrophysiology and mechanics, efficient fully monolithic solvers for large scale problems are much more rare. In our model we are able to include the fluid interaction with the geometry, acting with a prestress in each chamber, as explained in Sec. 3.5. A detailed explanation of the phases performed by each ventricle during a complete heartbeat will be shown in Sec. 4.7.

3 Mathematical models

In this chapter we focus on the description of the mathematical models used to represent the complex and various behaviour of the ventricles. In Section 3.1 we explain the electrophysiology dealing with the electrochemical reactions taking place in the myocardium. The myocardium is a complex tissue composed of cardiomyocytes, organized in fibres and laminar collagen sheets [99], characterising the orthotropic internal structure of the ventricles. Therefore, their material properties are strongly dependent on the direction of fibres and sheets. First, the electrical conductivity of the cardiomyocytes is much larger in the longitudinal direction than transversally [57, 80]; hence, at the macroscopic level, the transmembrane electric potential travels faster along the fibres. Secondly, it has been experimentally observed in [48] that the response of internal stresses to an external load significantly varies when measured along different directions since the myocardium is stiffer along the fibres (see Section 3.2). Finally, the contraction of the two ventricles is made possible thanks to an active force stretching the cardiomyocytes lined up long the fibres direction [93], this is explained in Section 3.3. In order to mathematically define fibres and sheets, we identify a local frame of reference by defining the mutually orthonormal fibres, sheets and normal vector fields.

3.1 Electrophysiology

Electrophysiology models describe the electrochemical reactions occurring in the myocardium [27] triggered by an electric impulse originated at the sinoatrial node and then conveyed through the Purkinje fibres to the whole heart [26]. Such signal induces a quick depolarization of the LV and RV cardiomyocytes, meaning that the *transmembrane potential* (i.e. the difference in electric potential between the interior and the exterior of a cell) changes sign in few microseconds. The potential produces a change in the concentration of different ionic species (mostly Na^+, K^+, Cl^-) flowing through the so–called ionic gates located on the cellular membrane; the concentration of these ionic species, in turn, influences the potential thus slowly re-polarizing the cells. The continuous interaction between the ions concentration and the potential causes a cascade effect for which a fast travelling wave propagates in the whole myocardium [62].

In this work, assuming the same electrophysiological behaviour for both left and right ventricles, we consider the *monodomain equation* for the description of the evolution of the cellular transmembrane potential V, a non-linear diffusion-reaction equation obtained by homogenization of the *bidomain equations* [26, 52, 80, 97]. The latter is indeed a richer, but more complicated model than the monodomain equation which is required to model pathological conditions. In physiological conditions, the monodomain model is adequate

and reads:

$$\begin{cases} \chi \left(C_m \dfrac{\partial V}{\partial t} + I^{ion}(V, \mathbf{w}) \right) = \nabla \cdot (J\mathbf{F}^{-1}\mathbf{D}_m\mathbf{F}^{-T}\nabla V) + I^{app}(t) & \text{in } \Omega_0 \times (0, T), \\ (J\mathbf{F}^{-1}\mathbf{D}_m\mathbf{F}^{-T}\nabla V) \cdot \mathbf{N} = 0 & \text{on } \partial\Omega_0 \times (0, T), \\ V = V_0 & \text{in } \Omega_0 \times \{0\}. \end{cases}$$
$$(3.1)$$

Here, Ω_0 is the reference computational domain (represented e.g. by the configuration of the ventricles at the end of the diastolic phase) and $T > 0$ is the final time. The components w_j, with $j \in \{1, \dots, M\}$ are M so-called gating variables taking values in $[0, 1]$ that regulate the transmembrane currents and the intracellular concentrations of the different ionic species. The parameters χ and $C_m \in \mathbb{R}^+$ are the ratio of membrane surface with respect to the volume and the membrane capacitance, respectively. In order to take into account the anisotropic electrical conductance [96], we define the diffusion tensor as

$$\mathbf{D}_m = \sigma_t\,\mathbf{I} + (\sigma_l - \sigma_t)\,\mathbf{f}_0 \otimes \mathbf{f}_0,$$

where $\sigma_t, \sigma_l \in \mathbb{R}^+$ are the electric conductivities in the directions transversal and longitudinal with respect to the fibres, respectively. The function $I^{app}(t)$ represents an externally applied current, which stands for the electric stimulus injected at the endocardium by the terminal fibres of the Purkinje network; for our purposes, we consider it as a source term which triggers the electrophysiological activity. The non-linear term $I^{ion}(V, \mathbf{w})$ is peculiar of the *ionic model* which, in the Hodgkin-Huxley formalism [47], takes the form:

$$\begin{cases} \dfrac{\mathrm{d}w_i}{\mathrm{d}t} = \alpha_i(V)(w_i^\infty(V) - w_i) + \beta_i(V)w_i & \text{in } (0, T), \\ w_i(0) = w_{i,0}, & \text{at } t = 0, \end{cases} \qquad \text{for } i = 1, \dots, N_I, \qquad (3.2)$$

Having the possibility to choose between many models proposed in literature – see e.g. [2, 62, 63, 72, 110] – we decide to follow the approach of [38] using the Bueno–Orovio minimal model [19] (for which $N_I = 3$), in fact even if it is simple it has the characteristic of capturing the main features of the electrophysiology in healthy myocardial tissues. The system of differential equations modelling the electrophysiology hence reads:

$$\begin{cases} \dfrac{\partial V}{\partial t} + \displaystyle\sum_{q \in \{fi, so, si\}} I^q(V, \mathbf{w}) = \nabla \cdot (J\mathbf{F}^{-1}\mathbf{D}_m\mathbf{F}^{-T}\nabla V) + I^{app}(t) & \text{in } \Omega_0 \times (0, T), \\ (J\mathbf{F}^{-1}\mathbf{D}_m\mathbf{F}^{-T}\nabla V) \cdot \mathbf{N} = 0 & \text{on } \partial\Omega_0 \times (0, T), \\ \dfrac{\partial \mathbf{w}}{\partial t} = \alpha(V)(\mathbf{w}^\infty(V) - \mathbf{w}) + \beta(V)\mathbf{w} & \text{in } \Omega_0 \times (0, T), \\ V = V_0, \quad \mathbf{w} = (1, 1, 0)^T & \text{in } \Omega_0 \times \{0\}, \end{cases}$$
$$(3.3)$$

since $\chi = C_m = 1$ as prescribed in [19], where the monodomain equation is presented in dimensionless form; moreover, $I^{ion}(V, \mathbf{w}) = \displaystyle\sum_{q \in \{fi, so, si\}} I^q(V, \mathbf{w})$. Albeit a system of ODEs, the ionic model is defined in $\Omega_0 \times (0, T)$ since the dependence on V indirectly introduces a

13

dependence on the space independent variable. The terms of the chosen ionic model are defined as:

$$\alpha(V) = \text{diag}\left(\frac{1 - H_{V_1}(V)}{\tau_1^-(V)}, \frac{1 - H_{V_2}(V)}{\tau_2^-(V)}, \frac{1}{\tau_3(V)}\right), \quad \beta(V) = \text{diag}\left(-\frac{H_{V_1}(V)}{\tau_1^+}, -\frac{H_{V_2}(V)}{\tau_2^+}, 0\right),$$

$$\mathbf{w}^\infty(V) = \left(1 - H_{V_1^-}(V), H_{V_o}(V)\left(w_*^\infty - 1 + \frac{V}{\tau_2^\infty}\right) + 1 - \frac{V}{\tau_2^\infty}, H_{V_3}^{k_3}(V)\right)^T,$$

$$I^{fi}(V, w_1) = -\frac{H_{V_1}(V)(V - V_1)(\widehat{V} - V)}{\tau_{fi}}w_1, \quad I^{so}(V) = \frac{(1 - H_{V_2}(V))(V - V_o)}{\tau_o(V)} + \frac{H_{V_2}(V)}{\tau_{so}(V)},$$

$$I^{si}(V, w_2, w_3) = -\frac{H_{V_2}(V)}{\tau_{si}}w_2 w_3,$$

while the characteristic time functions read:

$$\tau_1^-(V) = H_{V_1^-}(V)(\tau_1'' - \tau_1') + \tau_1', \quad \tau_2^-(V) = H_{V_2^-}^{k_2}(V)(\tau_2'' - \tau_2') + \tau_2',$$

$$\tau_3(V) = H_{V_2}(V)(\tau_3'' - \tau_3') + \tau_3', \quad \tau_o(V) = H_{V_o}(V)(\tau_o'' - \tau_o') + \tau_o',$$

$$\tau_{so}(V) = H_{V_{so}}^{k_{so}}(V)(\tau_{so}'' - \tau_{so}') + \tau_{so}'.$$

Here $H_a(z)$ is the Heaviside function centered in $a \in \mathbb{R}$, while $H_a^\varepsilon(z) = \dfrac{(1 + \tanh(\varepsilon(z - a)))}{2}$ stands for its smooth approximation depending on a constant parameter $\varepsilon \in \mathbb{R}^+$.

3.2 Tissue mechanics

Due to the complexity of the myocardium's displacement, we need a suitable mechanical model for the description of the tissue's dynamics. Even if there are studies which prove differences between the left and right cardiac tissue structure (see [64]), we will assume, for simplicity and for the lack of data respect the right ventricle, similar mechanics for both ventricles, we will highlight the differences in the following explanation. First of all, the internal stresses induced by a prescribed deformation are highly anisotropic [42] and in our formulation depend on the directions $\mathbf{f}_0$, $\mathbf{s}_0$, and $\mathbf{n}_0$ (see Figure 3.1).

Since biological tissues are mostly made of water, which is an incompressible fluid, it is usual to include in the hyperelastic models the incompressibility constraint. Although, we have to recall that any living tissue is not just made of water, it is a complex bundle of vessels of different scales, collagen, other substances and perfused blood. Possibly, we have to take into account the contraction of the muscle due to the electrophysiological activity: with this aim, we introduce the auxiliary dimensionless variable γ_f, which represents the relative stretching (or elongation) of the fibres. The model that we use to describe the evolution of γ_f will be detailed in Sec. 3.3 as it constitutes the link between electrophysiology and mechanics. We recall the momentum conservation equation in the reference configuration Ω_0, endowed with boundary and initial conditions, in the unknown
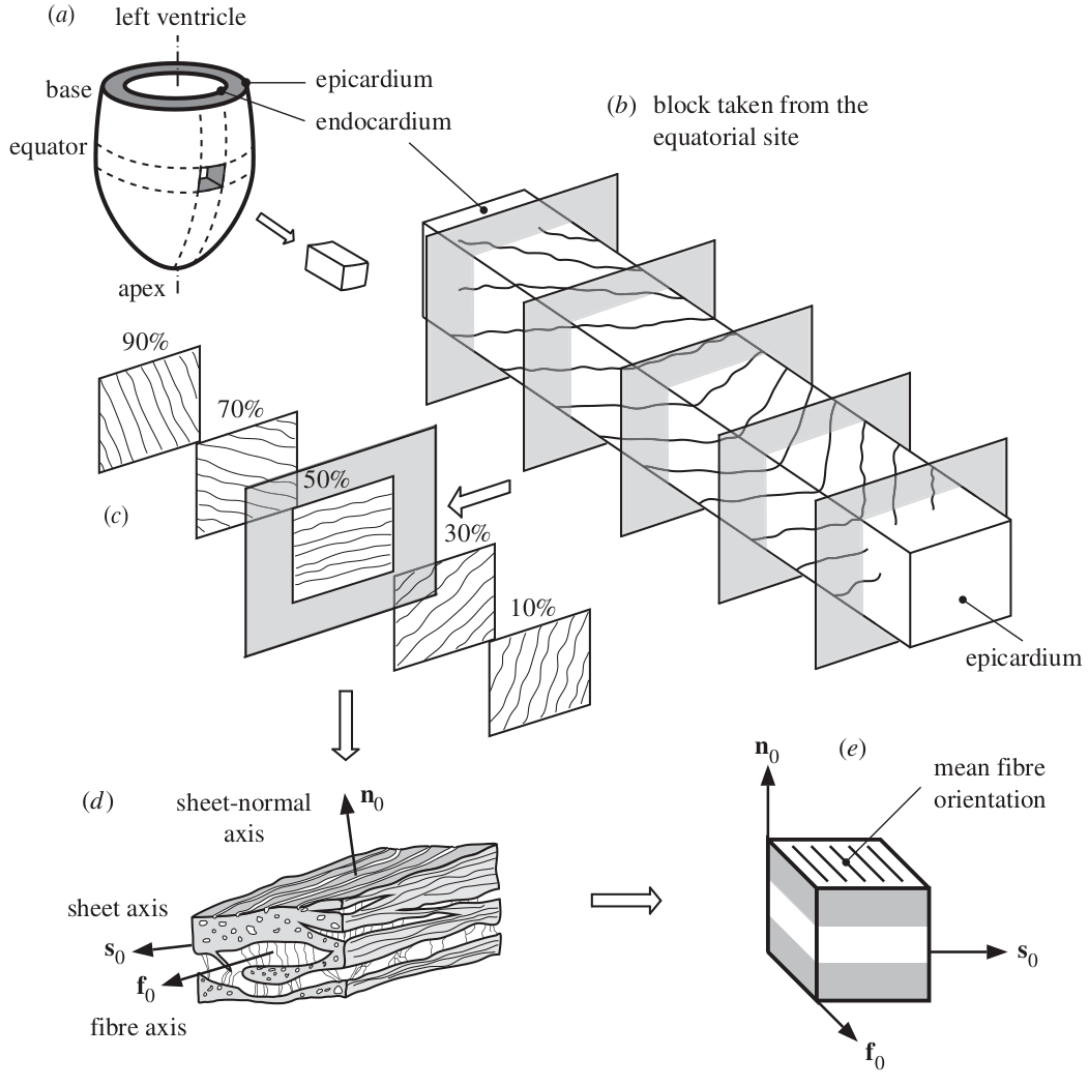
Figure 3.1: Schematic diagram of: (a) an idealized left ventricle and a cutout from the equator; (b) the structure through the thickness from the epicardium to the endocardium; (c) five longitudinal–circumferential sections at regular intervals from 10 to 90% of the wall thickness from the epicardium showing the transmural variation of layer orientation; (d) the layered organization of myocytes and the collagen fibres between the sheets referred to a right-handed orthonormal coordinate system with fibre axis $\mathbf{f}_0$, sheet axis $\mathbf{s}_0$ and sheet-normal axis $\mathbf{n}_0$; and (e) a cube of layered tissue with local material coordinates (X_1, X_2, X_3) serving as the basis for the geometrical and constitutive model. Image taken from [48].

displacement variable $\mathbf{d}$ [73]:

$$
\begin{cases}
\rho \dfrac{\partial^2 \mathbf{d}}{\partial t^2} - \nabla_0 \cdot \mathbf{P}(\mathbf{d}, \gamma_f) = \mathbf{0} & \text{in } \Omega_0 \times (0, T), \\[2ex]
(\mathbf{N} \otimes \mathbf{N})\left(K_\perp^\eta \mathbf{d} + C_\perp^\eta \dfrac{\partial \mathbf{d}}{\partial t}\right) + (\mathbf{I} - \mathbf{N} \otimes \mathbf{N})\left(K_\parallel^\eta \mathbf{d} + C_\parallel^\eta \dfrac{\partial \mathbf{d}}{\partial t}\right) & \\[2ex]
\quad + \mathbf{P}(\mathbf{d}, \gamma_f)\,\mathbf{N} = 0 & \text{on } \Gamma_0^\eta \times (0, T), \\[1ex]
\mathbf{P}(\mathbf{d}, \gamma_f)\,\mathbf{N} = p^{endo,LV}(t)\mathbf{N} & \text{on } \Gamma_0^{endo,LV} \times (0, T), \\[1ex]
\mathbf{P}(\mathbf{d}, \gamma_f)\,\mathbf{N} = p^{endo,RV}(t)\mathbf{N} & \text{on } \Gamma_0^{endo,RV} \times (0, T), \\[1ex]
\mathbf{d} = \mathbf{d}_0, \quad \dfrac{\partial \mathbf{d}}{\partial t} = \dot{\mathbf{d}}_0 & \text{in } \Omega_0 \times \{0\}.
\end{cases}
$$

$$(3.4)$$

15

Here, Γ_0^η with $\eta = \{epi, base\}$, represent the subsets of the boundary corresponding to the epicardium (we will distinguish between epi, LV and epi, RV only when needed) and the base of the myocardium, meanwhile $\Gamma_0^{endo,LV}$ and $\Gamma_0^{endo,RV}$ are, respectively, the left and right endocardium, as depicted in Fig. 3.2. We denote by $K_\perp^\eta, K_\parallel^\eta, C_\perp^\eta, C_\parallel^\eta \in \mathbb{R}^+$ the parameters of generalized Robin conditions on each of these boundary subsets: the symbols $\perp$ and $\parallel$ identify either a parameter relative to the normal or the tangential direction, respectively. We recall that having subdivided the epicardium in left and right subsets we have the possibility to apply different boundary condition to $\Gamma_0^{epi,LV}$ and $\Gamma_0^{epi,RV}$. This is to take into account a different interaction with the pericardium of the left and right ventricle. $p^{endo,LV}(t)$ and $p^{endo,RV}(t)$ are the external load applied by the fluid at each ventricle's endocardium wall which, at this stage of the model description only, we assume to be prescribed. It is important to stress the fact that $p^{endo}(t)$ assumes different values depending on the ventricle at which is applied. $\mathbf{N}$ is the outward directed unit vector normal to the boundary; $\mathbf{d}_0$ and $\dot{\mathbf{d}}_0$ are the initial data.

We model the mechanical behaviour taking advantage of the non-linear Piola–Kirchhoff strain tensor $\mathbf{P} = \mathbf{P}(\mathbf{d}, \gamma_f)$, which also must incorporate the active properties of the muscle. In order to derive $\mathbf{P}$, we have to define the right Cauchy–Green tensor as $\mathbf{C} = \mathbf{F}^T\mathbf{F}$, where $\mathbf{F} = \mathbf{I} + \nabla_0\mathbf{d}$ is the strain tensor, and, after that, we can introduce the strain energy function $\mathcal{W}(\mathbf{C}) : \mathbb{R}^{3\times3} \longrightarrow \mathbb{R}$. The latter takes into account the tissue mechanical properties: under the hyperelasticity assumption, the strain energy function is differentiated with respect to the deformation tensor in order to obtain the Piola-Kirchhoff strain tensor, i.e.:

$$\mathbf{P}(\mathbf{d}) = \frac{\partial\mathcal{W}(\mathbf{C})}{\partial\mathbf{F}}.$$

We will address the description of the myocardial tissue using the Holzapfel–Ogden [48] model. This is obtained by considering different contributions and by taking into account the anisotropic nature of the muscle:

$$
\begin{aligned}
\widetilde{\mathcal{W}}(\mathbf{C}) &= \mathcal{W}_1(\mathcal{I}_1) + \mathcal{W}_{4f}(\mathcal{I}_{4f}) + \mathcal{W}_{4s}(\mathcal{I}_{4s}) + \mathcal{W}_{8fs}(\mathcal{I}_{8fs}) \\
&= \frac{a}{2b}e^{b(\mathcal{I}_1-3)} + \sum_{i\in\{f,s\}}\frac{a_i}{2b_i}\left[e^{b\langle\mathcal{I}_{4i}-1\rangle^2} - 1\right] + \frac{a_{fs}}{2b_{fs}}\left[e^{b\mathcal{I}_{8fs}^2} - 1\right],
\end{aligned}
$$

where

$$
\begin{aligned}
\mathcal{I}_1 &= \operatorname{tr}\mathbf{C}, \qquad \mathcal{I}_{4f} = \mathbf{C} : \mathbf{f}_0\otimes\mathbf{f}_0 = \mathbf{f}\cdot\mathbf{f}, \\
\mathcal{I}_{4s} &= \mathbf{C} : \mathbf{s}_0\otimes\mathbf{s}_0 = \mathbf{s}\cdot\mathbf{s}, \qquad \mathcal{I}_{8fs} = \mathbf{C} : \mathbf{f}_0\otimes\mathbf{s}_0 = \mathbf{f}\cdot\mathbf{s}
\end{aligned}
$$

are the invariants of the tensor $\mathbf{C}$ and the parameters a_k, b_k are fitted from experimental data [48]. The function $\langle y \rangle = y\,H_0(y)$ indicates the positive part of y and its role consists in switching off the contributions to the stresses of the fibres and sheets when the material is under compression along their directions.

The mechanical model should also account for the volumetric change to which the myocardium undergoes during the cardiac cycle. It has been observed in [24, 124] that albeit this change is moderate, still it ranges from 2% to 15%. Consequently, we model the tissue's compressibility through a nearly–incompressible formulation by weakly penalizing large volumetric variations [101] since with this approach small volumetric changes are
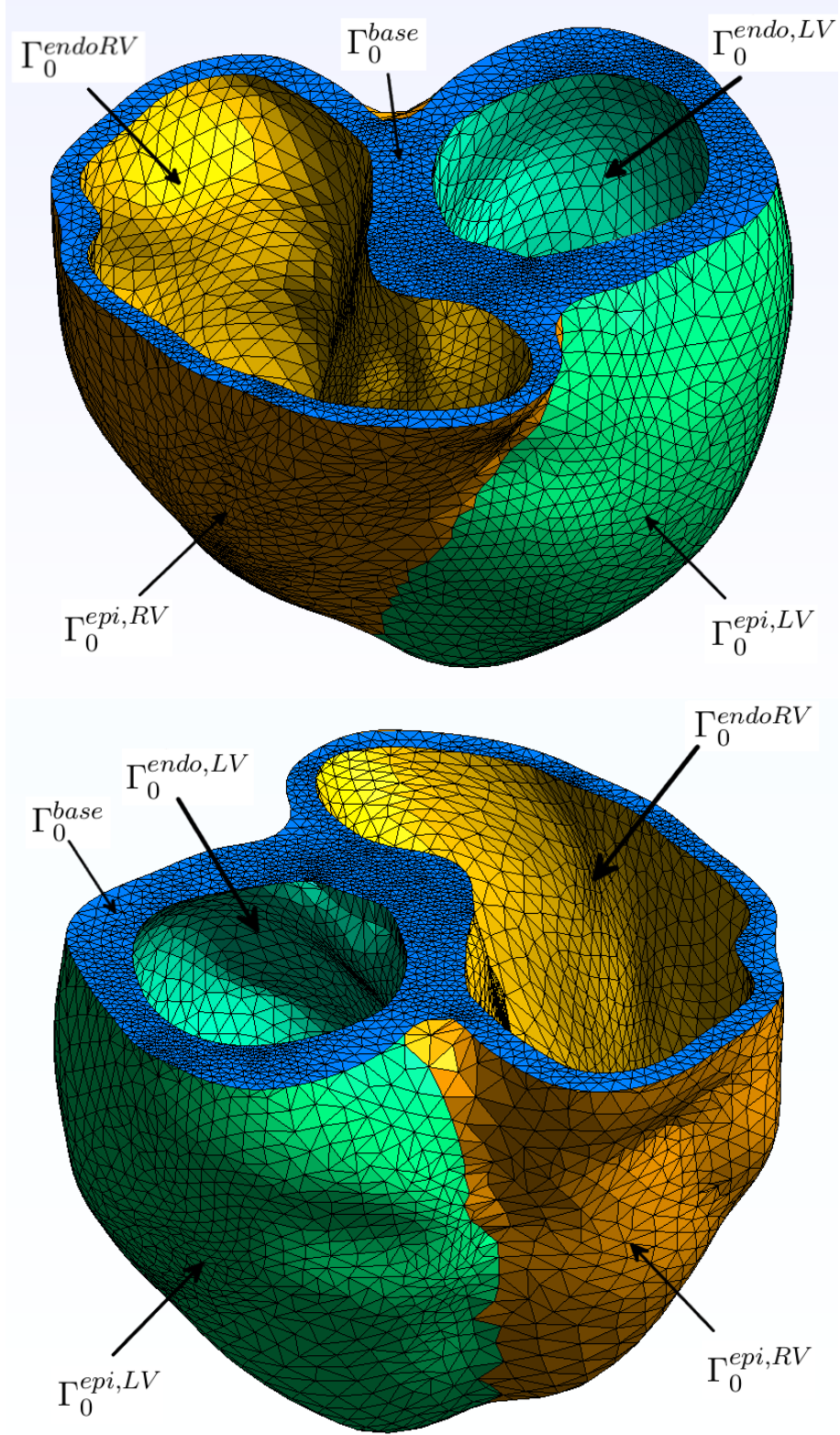
Figure 3.2: The patient–specific biventricle geometry used in this work with the $\Gamma_0^{epi,LV}$, $\Gamma_0^{epi,RV}$, $\Gamma_0^{endo,RV}$, $\Gamma_0^{endo,LV}$ and Γ_0^{base} boundary subsets highlighted. See Sec. 5.1 for details on this geometry.
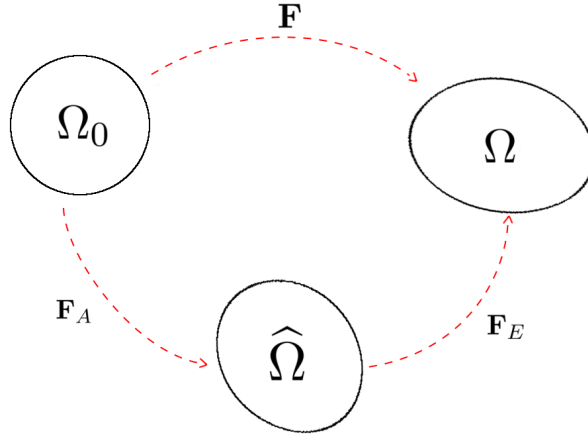
Figure 3.3: The active strain decomposition of the strain tensor $\mathbf{F}$. Taken from [38].

allowed [29]. We multiplicatively decompose the deformation gradient $\mathbf{F}$ into the isochoric and the volumetric parts as:

$$\mathbf{F} = \mathbf{F}_v \overline{\mathbf{F}}, \quad \mathbf{F}_v = J^{\frac{1}{3}}\,\mathbf{I}, \tag{3.5}$$

where $J = \det(\mathbf{F}_v) = \det(\mathbf{F})$, being $\det(\overline{\mathbf{F}}) = 1$, and we weakly enforce the incompressibility constraint by adding to the strain energy function $\widetilde{\mathcal{W}}$ a convex term $\mathcal{W}_{vol}(J)$ such that $J = 1$ is its global minimum; in this manner, large variations in volume are penalized. We choose:

$$\mathcal{W}_{vol}(J) = \frac{B}{2}(J + J\log J - 1), \tag{3.6}$$

such that the larger is the bulk modulus $B \in \mathbb{R}^+$, the "stronger" is the enforcement of the incompressibility constraint. Following [98], we evaluate the isotropic term $\mathcal{W}_1$ in $\overline{\mathcal{I}}_1 = \mathrm{tr}(\overline{\mathbf{F}}^T \overline{\mathbf{F}}) = J^{-\frac{2}{3}}\mathcal{I}_1$ (instead of $\mathcal{I}_1$). The energy function hence reads:

$$\mathcal{W} = \widetilde{\mathcal{W}} + \mathcal{W}_{vol} = \mathcal{W}_1(J^{-\frac{2}{3}}\mathcal{I}_1) + \mathcal{W}_{4f}(\mathcal{I}_{4f}) + \mathcal{W}_{4s}(\mathcal{I}_{4s}) + \mathcal{W}_{8fs}(\mathcal{I}_{8fs}) + \mathcal{W}_{vol}(J).$$

We now proceed by modelling the active behavior of the myocardium driven by the stretching of the fibres. By means of the *active strain* approach [3, 4, 71, 93]. A virtual intermediate state $\widehat{\Omega}$, representing the active part of the deformation, between the reference domain Ω_0 and the deformed one Ω (see Fig. 3.3) is introduced.

The domain $\widehat{\Omega}$ is reached from Ω_0 by applying a prescribed active transformation (which we will specify later) represented by the tensor $\mathbf{F}_A$. On the other hand, the material's elastic response to the prescribed active transformation is embedded in the tensor $\mathbf{F}_E$ and finally transforms $\widehat{\Omega}$ into Ω. At a macroscopic level, the latter represents the contraction of the sarcomeres depending on the calcium release, electrical excitation, and related phenomena taking place at cellular and subcellular scales. Mathematically, this approach requires a Lee's multiplicative decomposition [59] in the form

$$\mathbf{F} = \mathbf{F}_E \mathbf{F}_A = \mathbf{F}_v \overline{\mathbf{F}}_E \mathbf{F}_A = J^{\frac{1}{3}}\overline{\mathbf{F}}_E \mathbf{F}_A, \tag{3.7}$$

where we also take into account the factorization (3.5) for the term $\mathbf{F}_E$. Finally, we define $\mathbf{P}$ in Ω_0 with respect to the total displacement $\mathbf{d}$ of the tissue by applying a pull-back to

the stress computed in the intermediate state $\widehat{\Omega}$, i.e.:

$$\mathbf{P} = \det(\mathbf{F}_A)\mathbf{P}_E\mathbf{F}_A^{-T}, \quad \mathbf{P}_E = \frac{\partial \mathcal{W}(\mathbf{C}_E, J)}{\partial \mathbf{F}_E}.$$

In Section 3.3, we will provide the explicit form of the tensor $\mathbf{F}_A$ under the requirement of symmetry and identity of its determinant. Under these assumptions, the final form of the tensor $\mathbf{P}$ reads:

$$\begin{aligned}
\mathbf{P}(\mathbf{d}, \mathbf{F}_A) = {}& a e^{b\left(J^{-\frac{2}{3}}I_1^E - 3\right)} J^{-\frac{2}{3}} \left(\mathbf{F}_E\mathbf{F}_A^{-1} - \frac{I_1^E}{3}\left(\mathbf{F}_E\mathbf{F}_A\right)^{-T} \right) \\
& + 2a_f e^{b_f \langle I_{4f}^E - 1 \rangle^2} \langle I_{4f}^E - 1 \rangle \left(\mathbf{f}_E \otimes \mathbf{f}_A \right) \\
& + 2a_s e^{b_s \langle I_{4s}^E - 1 \rangle^2} \langle I_{4s}^E - 1 \rangle \left(\mathbf{s}_E \otimes \mathbf{s}_A \right) \\
& + a_{fs} e^{b_{fs}\left(I_{8fs}^E\right)^2} I_{8fs}^E \left(\mathbf{f}_E \otimes \mathbf{s}_A + \mathbf{s}_E \otimes \mathbf{f}_A \right) \\
& + \frac{B}{2} J \left(1 + \log(J) - \frac{1}{J} \right) \left(\mathbf{F}_E\mathbf{F}_A \right)^{-T},
\end{aligned} \tag{3.8}$$

where $\mathbf{f}_E = \mathbf{F}_E\mathbf{f}_0$, $\mathbf{f}_A = \mathbf{F}_A^{-1}\mathbf{f}_0$ and analogously $\mathbf{s}_E = \mathbf{F}_E\mathbf{s}_0$, $\mathbf{s}_A = \mathbf{F}_A^{-1}\mathbf{s}_0$.

3.3 Mechanical activation

The cardiac muscle is one of the most important example of active biological tissue. This means that it has the ability to actively change its own configuration as well as its mechanical properties without any external load. Moreover, the activation model of the myocardium represents the link between the electrophysiology and the tissue (passive) mechanics. Instead of cellular models describing the complex dynamic taking place inside the sarcomeres [87], we exploit a phenomenological model for the local shortening of the fibres γ_f at the macroscopic level. We follow the model presented in [38], which was proposed in [94] and further developed in [91], and assumes that the evolution of γ_f is due to the concentration of calcium ions $[Ca^{2+}]$ and by a feedback from the mechanics (through the variable $\mathbf{d}$):

$$\begin{cases}
g(c)\dfrac{\partial \gamma_f}{\partial t} - \varepsilon\Delta\gamma_f = \Phi(c, \gamma_f, \mathbf{d}) & \text{in } \Omega_0 \times (0, T), \\
\nabla\gamma_f \cdot \mathbf{N} = 0 & \text{on } \partial\Omega_0 \times (0, T), \\
\gamma_f = 0 & \text{in } \Omega_0 \times \{0\}.
\end{cases} \tag{3.9}$$

Here, $g(c) = \widehat{\mu}_A c^2$, while the active force $\Phi(c, \gamma_f, \mathbf{d})$ is defined as follows:

$$\Phi(c, \gamma_f, \mathbf{d}) = H_{c_0}(c)\alpha(c - c_0)^2 R_{FL}(I_{4f}) + \sum_{j=1}^{5}(-1)^j(j+1)(j+2)I_{4f}\gamma_f^j.$$

We have to highlight that the diffusive term $\varepsilon\Delta\gamma_f$ in (3.9) was added to yield a model in the form of a PDE. Moreover, even if this is not strictly motivated by physical considerations, it can be interpreted as an homogenization at the macroscopic continuum level of the

tissue of the microscopic activation. Furthermore, this choice provides benefits from the numerical approximation point of view, since we will obtain a more regular solution γ_f in terms of the space variable $\mathbf{X}$.

The contraction of the tissue is triggered by the calcium concentration exceeding a threshold value c_0. The parameters α and $\widehat{\mu}_A$ represent quantities to be properly tuned for the case under consideration, while R_{FL} is the sarcomere force-length relationship [41] of cardiac cells which we represent as truncated Fourier series:

$$R_{FL}(z) = \left(\frac{d_0}{2} + \sum_{n=1}^{3} \left[d_n \sin(n l_0 z^{1/2}) + e_n \cos(n l_0 z^{1/2}) \right] \right) \chi_{[SL_{min}, SL_{max}]}(z^{1/2}).$$

The calcium concentration is not explicitly represented in the set of variables $\mathbf{w}$ in the Bueno-Orovio model; however, the variable w_3 acts as a generic ion concentration, for which it can be interpreted as $c = [Ca^{2+}]$; this choice has been already made in literature e.g. in [91, 92].

Solving (3.9) we obtain γ_f. We have now to define a model for the activation tensor. We assume, for simplicity, that both the right and the left ventricles have the same mechanical behaviour. We will use, as described in [38], the orthotropic form for the tensor $\mathbf{F}_A$ [4, 9, 78, 91, 92]:

$$\mathbf{F}_A = \mathbf{I} + \gamma_f \mathbf{f}_0 \otimes \mathbf{f}_0 + \gamma_s \mathbf{s}_0 \otimes \mathbf{s}_0 + \gamma_n \mathbf{n}_0 \otimes \mathbf{n}_0,$$

which is symmetric. We are in fact assuming that the myocardium is composed with an orthotropic material, that is to say given an orthonormal ternary $\{\mathbf{f}_0, \mathbf{s}_0, \mathbf{n}_0\}$, the strain–energy is invariant with respect to rotations around any versor of the triplet. Moreover, we set $\gamma_n = \gamma_n(\gamma_f)$, $\gamma_s = \gamma_s(\gamma_f, \gamma_n)$. In analogy with γ_f, these functions represent the local shortening (or elongation) of the tissue in the directions $\mathbf{s}_0$ and $\mathbf{n}_0$, respectively. Following [10], we define γ_n such that, according to experimental observations [74], the thickening of the ventricles' walls is transversely non-homogeneous:

$$\gamma_n = k'(\lambda) \left(\frac{1}{\sqrt{1 + \gamma_f}} - 1 \right).$$

As we can see, the latter depends on an independent variable λ which represents the transmural coordinate, taking the value λ_{endo} at the endocardium and the value λ_{epi} at the epicardium. As detailed in [10] this model is able to capture the transmural heterogeneity of the thickening of the LV. In this work we will apply this model to the whole bi-ventricle's tissue, assuming the same behaviour in both the LV and RV, since there is no evidence of difference in the thickening of the ventricles. The function $k'(\lambda)$ is defined as:

$$k'(\lambda) = \overline{k}' \left(\overline{k}_{endo} \frac{\lambda - \lambda_{epi}}{\lambda_{endo} - \lambda_{epi}} + \overline{k}_{epi} \frac{\lambda - \lambda_{endo}}{\lambda_{epi} - \lambda_{endo}} \right). \tag{3.10}$$

Finally, as anticipated, we set:

$$\gamma_s = \frac{1}{(1 + \gamma_f)(1 + \gamma_n)} - 1.$$

In this way the condition $\det(\mathbf{F}_A) = 1$ is fulfilled.

3.4 The coupled model: electromechanics

Writing together Eqs.(3.3), (3.4), and (3.9), the coupled electromechanics problem finally reads:

$$
\begin{cases}
\dfrac{\partial V}{\partial t} + \displaystyle\sum_{q \in \{fi,so,si\}} I^q(V, \mathbf{w}) = \nabla \cdot (J\mathbf{F}^{-1}\mathbf{D}_m\mathbf{F}^{-T}\nabla V) - I^{app}(t) & \text{in } \Omega_0 \times (0,T), \\[2ex]
\dfrac{\partial \mathbf{w}}{\partial t} = \alpha(V)(\mathbf{w}^\infty(V) - \mathbf{w}) + \beta(V)\mathbf{w} & \text{in } \Omega_0 \times (0,T), \\[2ex]
\rho\dfrac{\partial^2 \mathbf{d}}{\partial t^2} - \nabla_0 \cdot \mathbf{P}(\mathbf{d}, \gamma_f) = \mathbf{0} & \text{in } \Omega_0 \times (0,T), \\[2ex]
g(w_3)\dfrac{\partial \gamma_f}{\partial t} - \varepsilon\Delta\gamma_f = \Phi(w_3, \gamma_f, \mathbf{d}) & \text{in } \Omega_0 \times (0,T), \\[3ex]
(J\mathbf{F}^{-1}\mathbf{D}_m\mathbf{F}^{-T}\nabla V) \cdot \mathbf{N} = 0 & \text{on } \partial\Omega_0 \times (0,T), \\[1ex]
(\mathbf{N} \otimes \mathbf{N})\left(K_\perp^\eta \mathbf{d} + C_\perp^\eta \dfrac{\partial \mathbf{d}}{\partial t}\right) + (\mathbf{I} - \mathbf{N} \otimes \mathbf{N})\left(K_\parallel^\eta \mathbf{d} + C_\parallel^\eta \dfrac{\partial \mathbf{d}}{\partial t}\right) \\
\qquad + \mathbf{P}(\mathbf{d})\mathbf{N} = \mathbf{0} & \text{on } \Gamma_0^\eta \times (0,T), \\[1ex]
\mathbf{P}(\mathbf{d})\mathbf{N} = p^{endo,LV}(t)\mathbf{N} & \text{on } \Gamma_0^{endo,LV} \times (0,T), \\[1ex]
\mathbf{P}(\mathbf{d})\mathbf{N} = p^{endo,RV}(t)\mathbf{N} & \text{on } \Gamma_0^{endo,RV} \times (0,T), \\[1ex]
\nabla\gamma_f \cdot \mathbf{N} = 0 & \text{on } \partial\Omega_0 \times (0,T), \\[3ex]
V = V_0, \quad \mathbf{w} = (1,1,0)^T, \quad \gamma_f = 0 & \text{in } \Omega_0 \times \{0\}, \\[2ex]
\mathbf{d} = \mathbf{d}_0, \quad \dfrac{\partial \mathbf{d}}{\partial t} = \dot{\mathbf{d}}_0 & \text{in } \Omega_0 \times \{0\}.
\end{cases}
$$
$$\tag{3.11}$$

We remark that at this stage the pressures $p^{endo,LV}(t)$ and $p^{endo,RV}(t)$ are still prescribed: however, later in Section 4.7, we will consider $p^{endo,LV}(t)$ and $p^{endo,RV}(t)$ as additional unknowns of the coupled problem, being the solution of 0D problems (that is, ordinary differential equations) at each of the phases of the cardiac cycle.

3.5 Prestress

As we will see in the Sec. 5.1, we will take advantage of a reference geometry Ω_0 acquired through Magnetic Resonance Imaging and we will assume that our Ω_0 is at tele-diastole (the phase immediately before the systole), which gives us a configuration which is not stress–free. This is a known problem dealing with biomedical modelling involving fluid–structure interface. We have to model the pressures $p^{endo,LV}(t)$ and $p^{endo,RV}(t)$ on each endocardium wall exerted by the blood. We have to recall that these quantities are always larger than zero during the cardiac cycle. In fact, from medical measurements (e.g. [17, 86]), we have the approximate values in Table 3.1. This implies that solving prob-

Site		Normal pressure range (in mmHg)
Right ventricular pressure	systolic	15–30
	diastolic	3–8
Left ventricular pressure	systolic	100–120
	diastolic	3–12

Table 3.1: Ventricular pressures

lem (3.4) with physiological endocardial pressures $p^{endo,LV} > 0$ and $p^{endo,RV} > 0$ would give rise to non-physiological displacements as the internal stresses are not in equilibrium with the intraventricular blood's pressure of the ventricles. We indicate with $\overline{p}^{endo,LV}$ and $\overline{p}^{endo,RV}$ the pressure at telediastole and the stressed ventricles' configuration is determined in these conditions. To address this issue we will adapt to our problem the one proposed in [38], an extension of the method presented in [51], called *pressure prestress* [109]. We compute an internal stresses distribution such that the reference geometry is in equilibrium with the blood pressures $\overline{p}^{endo,LV}$ and $\overline{p}^{endo,RV}$ both in the left and in the right ventricles. With this aim we proceed with an additive decomposition of the strain tensor $\widetilde{\mathbf{P}} = \mathbf{P}(\mathbf{d}) + \mathbf{P}_0$, where the prestress tensor $\mathbf{P}_0$ is determined to ensure a null displacement $\mathbf{d}_0$ in correspondence of the assigned pressures $\overline{p}^{endo,LV}$ and $\overline{p}^{endo,RV}$.

In order to compute $\mathbf{P}_0$ according to this approach, we proceed by adapting the method proposed in [51] to our model by first defining the following mechanical problem:

$$\begin{cases} \nabla_0 \cdot \mathbf{P}(\mathbf{d}) = -\nabla_0 \cdot \mathbf{P}_0 & \text{in } \Omega_0, \\ (\mathbf{N} \otimes \mathbf{N})K_\perp^\eta \mathbf{d} + (\mathbf{I} - \mathbf{N} \otimes \mathbf{N})K_\parallel^\eta \mathbf{d} + \mathbf{P}(\mathbf{d})\,\mathbf{N} = 0 & \text{on } \Gamma_0^\eta, \\ \mathbf{P}(\mathbf{d})\,\mathbf{N} = p^{endo,LV}(t)\mathbf{N} & \text{on } \Gamma_0^{endo,LV} \\ \mathbf{P}(\mathbf{d})\,\mathbf{N} = p^{endo,RV}(t)\mathbf{N} & \text{on } \Gamma_0^{endo,RV}. \end{cases} \tag{3.12}$$

We recall that in our case the endocardium is subdivided in the two ventricles so we need to assign different constant values to the right and left chamber at telediastole. We can do that since we have a particular label for each ventricle. We set $\overline{p}^{endo,LV} = 10$ mmHg and $\overline{p}^{endo,RV} = 5$ mmHg. Eq. (3.12) is the steady, passive version of problem (3.4) with the additive decomposition of the strain tensor. Moreover, we set

$$p_k^{LV} = \frac{k}{S}\overline{p}^{endo,LV} \quad \text{and} \quad p_k^{RV} = \frac{k}{S}\overline{p}^{endo,RV}, \quad k = 1, \dots, S,$$

where $S \in \mathbb{N}$ is the number of steps of the continuation method that we exploit to gradually increase the pressure value inside each chamber. Then, the fixed point described in Algorithm 1 is applied to compute $\mathbf{P}_0$. First, we compute the approximation $\widetilde{\mathbf{P}}_0 = \text{PRESTRESS}(100, 10^{-2}, \overline{p}^{endo,LV}, \overline{p}^{endo,RV}, \mathbf{0})$ and finally we set $\mathbf{P}_0 = \text{PRESTRESS}(1, 10^{-5}, \overline{p}^{endo,LV}, \overline{p}^{endo,RV}, \widetilde{\mathbf{P}}_0)$. The additional step is performed to require a smaller tolerance when the pressures have already reached a closer value of the tensor $\widetilde{\mathbf{P}}_0$ to the target. We observe that, while $\frac{\|\mathbf{P}(\mathbf{d}_k^m, \mathbf{I})\|_\infty}{\|\mathbf{P}_{0,k}^m\|_\infty} \longrightarrow 0$ for $m \longrightarrow +\infty$ in Algorithm 1, the displacement $\mathbf{d}_k^{m+1}$ does not converge to $\mathbf{0}$ but to a vector which we denote by $\widehat{\mathbf{d}}$. However, we observe

that the quantity $\|\widehat{\mathbf{d}}\|_\infty$ is negligible with respect to the endocardial walls thickness, and that this initial displacement ensures that the prestress is in equilibrium with the pressure at the epicardium. Therefore, we set $\mathbf{d}_0 = \widehat{\mathbf{d}}$ in (3.11).

Algorithm 1 Prestress computation

---

function PRESTRESS(S, tol, $\overline{p}^{endo,LV}$, $\overline{p}^{endo,RV}$, $\mathbf{P}_{0,0}$)

    for $k = 1, \ldots, S$ **do**

        set $m = 1$, $\mathbf{P}_{0,k}^m = \mathbf{P}_{0,k-1}$;

        repeat

            obtain $\mathbf{d}_k^{m+1}$ by solving problem (3.12) with

            $p^{LV} = p_k^{LV} = \frac{k}{S}\overline{p}^{endo,LV}$, $p^{RV} = p_k^{RV} = \frac{k}{S}\overline{p}^{endo,RV}$ and $\mathbf{P}_0 = \mathbf{P}_{0,k}^m$;

            update $\mathbf{P}_{0,k}^{m+1} = \mathbf{P}_{0,k}^m + \mathbf{P}\left(\mathbf{d}_k^{m+1}, \mathbf{I}\right)$ by means of Eq. (3.8);

            set $m = m + 1$;

        until $\frac{\|\mathbf{P}\left(\mathbf{d}_k^m, \mathbf{I}\right)\|_\infty}{\|\mathbf{P}_{0,k}^m\|_\infty} < tol$

        set $\mathbf{P}_{0,k} = \mathbf{P}_{0,k}^m$;

    end for

    return $\mathbf{P}_{0,S}$

end function

---

4 Numerical discretization

In this chapter we describe the numerical approximation of the electromechanics problem (3.11). The Finite Element Method (FEM) [84] is used for the space discretization of the PDEs, while Backward Differentiation Formula (BDF) [84] are used for the time discretization.

4.1 Space discretization

We consider a mesh composed of tetrahedrons $\mathcal{T}_h$, with h representing the maximum size of the elements $K \in \mathcal{T}_h$, such that $\cup_{K \in \mathcal{T}_h} K = \Omega_0$; the mesh elements are pairwise disjoint and their union $\Omega_0 \subset \mathbb{R}^3$ is the region of the space identified by the myocardium assuming to be at the telediastolic phase of the heartbeat. We consider a bi-ventricle geometry taken from a cardiac atlas ([49]). We will describe how we managed to extrapolate our mesh from the whole heart in Section 5.1. We will approximate each of the single core models in the computational domain with a space discretization based on the FEM. We denote by $N_V^{\mathrm{dof}}, N_{\mathbf{w}}^{\mathrm{dof}}, N_{\mathbf{d}}^{\mathrm{dof}}$, and $N_{\gamma_f}^{\mathrm{dof}}$ the number of Degrees of Freedom (DoF) (i.e. the size of the discretized single core model) for the potential, ionic variables, displacement, and fibre shortening, respectively. The underlying number of nodes determined by the mesh $\mathcal{T}_h$ is indicated as N_h.

4.2 Monodomain equation

We proceed to the spatial approximation of the monodomain equation (3.1) with the FEM. Firstly we introduce the finite dimensional space $\mathcal{X}_h^1 = \left\{ v \in C^0(\overline{\Omega}_0) \; : \; v|_K \in \mathbb{P}^1(K) \; \forall K \in \mathcal{T}_h \right\}$, where $\mathbb{P}^1(K)$ is the set of polynomials of degree equal to 1 in the element K. Moreover, we denote by $\{\psi_i\}_{i=1}^{N_V^{\mathrm{dof}}}$ a basis of $\mathcal{X}_h^1$ with $N_V^{\mathrm{dof}} = \dim(\mathcal{X}_h^1)$. The projection of the solution $V(t)$ on the finite space $\mathcal{X}_h^1$ can hence be written as $V_h(t) = \sum_{j=1}^{N_V^{\mathrm{dof}}} V_j(t) \psi_j$ and the weak semidiscrete formulation of the problem reads: given $\mathbf{w}_h(t)$ and $\mathbf{d}_h(t)$, find, for all $t \in (0, T)$, $V_h(t) \in \mathcal{X}_h^1$ such that

$$\int_{\Omega_0} \dot{V}_h \psi_i \, d\Omega_0 + \int_{\Omega_0} (J\mathbf{F}_h^{-1}\mathbf{D}_m \mathbf{F}_h^{-T} \nabla V_h) \cdot \nabla \psi_i \, d\Omega_0$$

$$+ \sum_{q \in \{fi,so,si\}} \int_{\Omega_0} I^q(V_h, \mathbf{w}_h) \psi_i \, d\Omega_0 = \int_{\Omega_0} I^{app}(t) \psi_i \, d\Omega_0, \quad \forall i = 1, \ldots, N_V^{\mathrm{dof}}, \tag{4.1}$$

with $V_h(0) = \sum_{j=1}^{N_V^{\mathrm{dof}}} (V_0, \psi_j)_{L^2(\Omega_0)} \psi_j$.

By setting $\mathbf{V}_h(t) = \{V_j(t)\}_{j=1}^{N_V^{\mathrm{dof}}}$ and $\mathbf{V}_{0,h} = \left\{ (V_0, \psi_j)_{\mathcal{H}} \right\}_{j=1}^{N_V^{\mathrm{dof}}}$, we rewrite Eq. (4.1) as a

system of non-linear ODEs:

$$
\begin{cases}
\mathbb{M}\dot{\mathbf{V}}_h(t) + \mathbb{K}(\mathbf{d}_h(t))\mathbf{V}_h(t) + \mathbf{I}_{ion}(\mathbf{V}_h(t), \mathbf{w}_h(t)) = \mathbf{I}_{app}(t) & t \in (0,T), \\
\mathbf{V}_h(0) = \mathbf{V}_{0,h},
\end{cases}
\tag{4.2}
$$

where:

$$
\mathbb{M}_{ij} = \int_{\Omega_0} \psi_j \psi_i \, d\Omega_0, \quad \mathbb{K}_{ij}(\mathbf{d}_h) = \int_{\Omega_0} (J\mathbf{F}_h^{-1}\mathbf{D}_m\mathbf{F}_h^{-T}\nabla\psi_j) \cdot \nabla\psi_i \, d\Omega_0
$$

$$
(\mathbf{I}_{ion}(\mathbf{V}_h, \mathbf{w}_h))_i = \sum_{q \in \{fi,so,si\}} \int_{\Omega_0} I^q(V_h, \mathbf{w}_h)\,\psi_i\, d\Omega_0, \quad (\mathbf{I}_{app}(t))_i = \int_{\Omega_0} I^{app}(t)\psi_i \, d\Omega_0.
\tag{4.3}
$$

Different strategies can be made for the approximation of the non-linear term $\mathbf{I}_{ion}(\mathbf{V}_h, \mathbf{w}_h)$. We follow the choice of using the *State Variable Interpolation* (SVI) [38] which we will find out to be exactly the standard FEM approximation. Indeed, by denoting with $\left\{\mathbf{x}_s^K\right\}_{s=1}^{N_q}$ and $\left\{\omega_s^K\right\}_{s=1}^{N_q}$ the quadrature nodes and the corresponding weights in a generic mesh element $K \in \mathcal{T}_h$, the variables V_h and $\mathbf{w}_h$ in Eq. (4.3) can be evaluated at the quadrature nodes

$$
\int_{\Omega_0} I^q(V_h, \mathbf{w}_h)\psi_i\, d\Omega_0 = \sum_{K \in \mathcal{T}_h}\left(\sum_{s=1}^{N_q} I^q \left(\sum_{j=1}^{N_V^{dof}} V_j(t)\psi_j(\mathbf{x}_s^K), \sum_{j=1}^{N_V^{dof}} \mathbf{w}_j(t)\psi_j(\mathbf{x}_s^K) \right) \psi_i(\mathbf{x}_s^K)\,\omega_s^K \right).
$$

We will prove in our simulations that following this approach we will have the tendency to overestimate the conduction velocities if the computational mesh is not "sufficiently" fine [70], but yield convergent results under h–refinement. This is a behaviour described in [38] for the LV, we confirm it also for the bi-ventricle context. Furthermore, since we know that a numerical issue may occur in the case of problems with "travelling waves" due to the dominance of zero order terms over the second order ones [20], we will use in Eq. (4.2) a lumped mass matrix $\mathbb{M}^L$ in place of $\mathbb{M}$ in order to avoid numerical oscillations.

4.3 Ionic model

The ionic model (3.2) is a system of ODEs that indirectly depends on the space variable through the transmembrane potential V. By denoting with $\{\mathbf{x}_j\}_{j=1}^{N_{\mathbf{w}}^{\text{dof}}}$ the set of the degrees of freedom, we write the equations of the model evaluated at each of these points and we denote the value of the l-th ionic variable in $\mathbf{x}_j$ by $w_j^l(t)$. Similarly, we write $V_j(t) = V_h(\mathbf{x}_j, t)$, and finally rearrange the unknowns in the vector $\mathbf{w}_h(t)$ in the following fashion:

$$
\mathbf{w}_h(t) = \left\{\mathbf{w}_h^l(t)\right\}_{l=1}^{N_I} \quad \text{and} \quad \mathbf{w}_h^l(t) = \left\{w_j^l(t)\right\}_{j=1}^{N_{\mathbf{w}}^{\text{dof}}}.
\tag{4.4}
$$

The problem thus obtained reads: given $V_h(t)$, find, for all $t \in (0,T)$, $\mathbf{w}_h(t)$ such that

$$
\dot{w}_j^l + (\alpha_l(V_j) - \beta_l(V_j))w_j^l = \alpha_l(V_j)w_l^\infty(V_j),
\tag{4.5}
$$

with $w_j^l(0) = w_0^l$, for $l = 1, \ldots, N_I$, $j = 1, \ldots, N_{\mathbf{w}}^{\text{dof}}$.

Following the conventions of Eq. (4.4), system (4.5) can be conveniently rewritten in algebraic form as

$$
\begin{cases}
\dot{\mathbf{w}}_h(t) + \mathbb{U}(V_h(t))\mathbf{w}_h(t) = \mathbf{Q}(V_h(t)), & t \in (0,T], \\
\mathbf{w}_h(0) = \mathbf{w}_{0,h},
\end{cases}
$$

where the block matrix $\mathbb{U}$ and the block vector $\mathbf{Q}$ are defined as

$$
(\mathbf{Q}(V_h))_m = \alpha_l(V_j)w_l^\infty(V_j),
$$
$$
(\mathbb{U}(V_h))_{mm} = \alpha_l(V_j) - \beta_l(V_j),
$$

where $m = l\,N_{\mathbf{w}}^{\mathrm{dof}} + j$, for $l = 1, \ldots, N_I,\ j = 1, \ldots, N_{\mathbf{w}}^{\mathrm{dof}}$.

4.4 Active and passive mechanics

Following the same procedure as the one applied to the monodomain equation, we use the FEM to approximate the momentum equation (3.4). We denote by $[\mathcal{X}_h^1]^3$ the finite dimensional subspace of vector valued functions and by $\{\boldsymbol{\psi}_i\}_{i=1}^{N_{\mathbf{d}}^{dof}}$ its basis. The Galerkin formulation of Eq. (3.4) reads: given $\gamma_{f,h}(t)$, find, for all $t \in (0,T)$, $\mathbf{d}_h(t) \in [\mathcal{X}_h^1]^3$ such that

$$
\int_{\Omega_0} \rho_s \frac{\partial^2 \mathbf{d}_h}{\partial t^2} \cdot \boldsymbol{\psi}_i \, d\Omega_0 + \int_{\Omega_0} \mathbf{P}(\mathbf{d}_h, \gamma_{f,h}) : \nabla_0 \boldsymbol{\psi}_i \, d\Omega_0
$$

$$
+ \sum_{\eta \in \{epi,base\}} \int_{\Gamma_0^\eta} \left((\mathbf{N} \otimes \mathbf{N}) \left(K_\perp^\eta \mathbf{d}_h + C_\perp^\eta \frac{\partial \mathbf{d}_h}{\partial t} \right) + (\mathbf{I} - \mathbf{N} \otimes \mathbf{N}) \left(K_\parallel^\eta \mathbf{d}_h + C_\parallel^\eta \frac{\partial \mathbf{d}_h}{\partial t} \right) \right) \cdot \boldsymbol{\psi}_i \, d\Gamma_0
$$

$$
= \int_{\Gamma_0^{endo,LV}} p^{endo,LV}(t)\mathbf{N} \cdot \boldsymbol{\psi}_i \, d\Gamma_0 + \int_{\Gamma_0^{endo,RV}} p^{endo,RV}(t)\mathbf{N} \cdot \boldsymbol{\psi}_i \, d\Gamma_0, \qquad \forall i = 1, \ldots, N_{\mathbf{d}}^{dof},
$$

with $\mathbf{d}_h(0) = \sum_{\eta=1}^{N_{\mathbf{d}}^{\mathrm{dof}}} (\mathbf{d}_0, \boldsymbol{\psi}_j)_{[L^2(\Omega_0)]^3} \boldsymbol{\psi}_j$ and $\dot{\mathbf{d}}_h(0) = \sum_{\eta=1}^{N_{\mathbf{d}}^{\mathrm{dof}}} \left(\dot{\mathbf{d}}_0, \boldsymbol{\psi}_j \right)_{[L^2(\Omega_0)]^3} \boldsymbol{\psi}_j$.

Recall that in our case the endocardium is divided between right and left ventricle, as defined in Fig. 3.2, so we have to take into account two different pressure values. We rewrite it in algebraic form as:

$$
\begin{cases}
\rho_s \mathbb{M}\ddot{\mathbf{d}}_h(t) + \mathbb{F}\dot{\mathbf{d}}_h(t) + \mathbb{G}\mathbf{d}_h(t) + \mathbf{S}(\mathbf{d}_h(t), \gamma_{f,h}(t)) = \mathbf{p}^{endo,LV}(t) + \mathbf{p}^{endo,RV}(t) & t \in (0,T], \\
\mathbf{d}_h(0) = \mathbf{d}_{0,h}, \quad \dot{\mathbf{d}}_h(0) = \dot{\mathbf{d}}_{0,h},
\end{cases}
$$

where, in particular,

$$
\mathbb{F}_{ij} = \sum_{\eta \in \{epi,base\}} \int_{\Gamma_0^\eta} \left(C_\perp^\eta(\mathbf{N} \otimes \mathbf{N}) + C_\parallel^\eta(\mathbf{I} - \mathbf{N} \otimes \mathbf{N}) \right) \boldsymbol{\psi}_j \cdot \boldsymbol{\psi}_i \, d\Gamma_0,
$$

$$
\mathbb{G}_{ij} = \sum_{\eta \in \{epi,base\}} \int_{\Gamma_0^\eta} \left(K_\perp^\eta(\mathbf{N} \otimes \mathbf{N}) + K_\parallel^\eta(\mathbf{I} - \mathbf{N} \otimes \mathbf{N}) \right) \boldsymbol{\psi}_j \cdot \boldsymbol{\psi}_i \, d\Gamma_0,
$$

and

$$\mathbf{S}_i(\mathbf{d}_h(t), \gamma_{f,h}(t)) = \int_{\Omega_0} \mathbf{P}(\mathbf{d}_h, \gamma_{f,h}) : \nabla_0 \boldsymbol{\psi}_i \, d\Omega_0.$$

Finally, we once again use the FEM to discretize in space the equation for the unknown γ_f: given $c_h(t)$ and $\mathbf{d}_h(t)$, find, for all $t \in (0, T)$, $\gamma_{f,h}(t) \in \mathcal{X}_h$ such that

$$\int_{\Omega_0} \frac{\partial \gamma_{f,h}}{\partial t} \, \psi_i \, d\Omega_0 + \varepsilon \int_{\Omega_0} \frac{1}{g(c_h)} \nabla \gamma_{f,h} \cdot \nabla \psi_i \, d\Omega_0$$

$$- \int_{\Omega_0} \frac{1}{g(c_h)} \Phi(c_h, \gamma_{f,h}, \mathbf{d}_h) \, \psi_i \, d\Omega_0 = 0, \qquad \forall i = 1, \dots, N_{\gamma_f}^{dof},$$

with $\gamma_{f,h}(0) = 0$. Note that, with respect to Eq. (3.9), we divided all the terms by $g(c_h)$ to avoid the non-linearity in the time derivative term.

Finally, we obtain the following system of ODEs:

$$\begin{cases} \mathbb{M}\dot{\boldsymbol{\gamma}}_{f,h}(t) + \varepsilon\mathbb{K}(c(t))\boldsymbol{\gamma}_{f,h}(t) + \boldsymbol{\Phi}(c(t), \boldsymbol{\gamma}_{f,h}(t), \mathbf{d}(t)) = \mathbf{0} & t \in (0, T], \\ \boldsymbol{\gamma}_{f,h}(0) = \mathbf{0}. \end{cases}$$

4.5   Time discretization

The natural step after having spatially discretized each core model is to proceed with the time discretization of the semi–discretized formulation of problem (3.11), in the form of a non-linear system of ODEs. Following the notation defined in [38] we denote by $\mathbf{z} = (\mathbf{z_w}, \mathbf{z}_V, \mathbf{z}_{\gamma_f}, \mathbf{z_d})^T$ the block vector containing the unknowns of each semi–discrete single core problem and we write:

$$\begin{cases} \mathcal{M}\mathbf{z}(t) + \mathbf{T}(\mathbf{z}(t)) = \mathbf{h}(t) & t \in (0, T], \\ \mathbf{z}(0) = \mathbf{z}_0, \\ \dot{\mathbf{z}}_{\mathbf{d}}(0) = \dot{\mathbf{d}}_{0,h}, \end{cases} \tag{4.6}$$

where we define the differential operator

$$\mathcal{M} = \mathrm{diag}\left(\frac{\mathrm{d}}{\mathrm{dt}}, \frac{\mathrm{d}}{\mathrm{dt}}, \frac{\mathrm{d}}{\mathrm{dt}}, \frac{\mathrm{d}^2}{\mathrm{dt}^2} \right),$$

This operator permits us to apply a first order time derivative to the ionic variables, the transmembrane potential and the fibres shortening (motivating the division by $g(c_h)$ of the corresponding equation), while a second order time derivative to the displacement. We use the BDF for the time approximation of Eq. (4.6), in order to obtain a fully discretized formulation. Hence, we write:

$$\dot{z}_i(t^{n+1}) \approx \frac{1}{\Delta t}\left(\vartheta_0^{(I)} z_i^{n+1} - z_i^{RHS} \right), \qquad z_i^{RHS} = \sum_{k=1}^{\sigma} \vartheta_k^{(I)} z_i^{n-k+1},$$

$$\ddot{z}_i(t^{n+1}) \approx \frac{1}{(\Delta t)^2}\left(\vartheta_0^{(II)} z_i^{n+1} - z_i^{RHS} \right), \qquad z_i^{RHS} = \sum_{k=1}^{\sigma+1} \vartheta_k^{(II)} z_i^{n-k+1},$$

where $\Delta t = \frac{T}{N_T}$ is the timestep, N_T being the number of timesteps, while the parameters $\vartheta_k^{(\mathrm{I})}, \vartheta_k^{(\mathrm{II})}, k = 0, \ldots, \sigma$ depend on the order σ of the BDF scheme. We will in particular use BDF of order $\sigma = 2$, and will consider fully implicit scheme for the time discretization of the monolithic problem.

Eventually, in the implicit case, we obtain the following non-linear system:

$$\mathbf{A}(\mathbf{z}^{n+1}) = \mathbf{b}^{n+1} \qquad n = \sigma, \ldots, N_T - 1, \tag{4.7}$$

with $\mathbf{z}^k$ assigned for $k = 0, \ldots, \sigma$ and we set for simplicity $\dot{\mathbf{d}}_{0,h} = \mathbf{0}$. Problem (4.7) is solved by exploiting the Newton method [84] at each timestep.

4.5.1 The implicit scheme

By applying the Newton method [84] to (4.7), we iteratively solve for $n = \sigma, \ldots, N_T - 1$ the linear problem

$$\begin{cases} \mathbb{J}_k^{n+1} \delta \mathbf{z}_{k+1}^{n+1} = -\mathbf{r}_k^{n+1}, \\ \mathbf{z}_{k+1}^{n+1} = \mathbf{z}_k^{n+1} + \delta \mathbf{z}_{k+1}^{n+1}, \end{cases} \tag{4.8}$$

for $k = 0, \ldots$, until some convergence criterion is met. $\mathbb{J}_k^{n+1}$ is the Jacobian matrix of $\mathbf{A}$ evaluated in the $\mathbf{z}_k^{n+1}$ and is endowed with the following block structure:

$$\mathbb{J}_k^{n+1} = \begin{bmatrix} \mathbb{J}_{\mathbf{w}}(\mathbf{V}_k^{n+1}) & \mathbb{J}_{\mathbf{w}\mathbf{V}}(\mathbf{w}_k^{n+1}, \mathbf{V}_k^{n+1}) & 0 & 0 \\ \mathbb{J}_{\mathbf{V}\mathbf{w}}(\mathbf{w}_k^{n+1}, \mathbf{V}_k^{n+1}) & \mathbb{J}_{\mathbf{V}}(\mathbf{d}_k^{n+1}) & 0 & \mathbb{J}_{\mathbf{V}\mathbf{d}}(\mathbf{V}_k^{n+1}, \mathbf{d}_k^{n+1}) \\ \mathbb{J}_{\boldsymbol{\gamma}_f \mathbf{w}}(\mathbf{w}_k^{n+1}, \boldsymbol{\gamma}_{f_k}^{n+1}, \mathbf{d}_k^{n+1}) & 0 & \mathbb{J}_{\boldsymbol{\gamma}_f}(\mathbf{w}_k^{n+1}, \boldsymbol{\gamma}_{f_k}^{n+1}, \mathbf{d}_k^{n+1}) & \mathbb{J}_{\boldsymbol{\gamma}_f \mathbf{d}}(\mathbf{w}_k^{n+1}, \boldsymbol{\gamma}_{f_k}^{n+1}, \mathbf{d}_k^{n+1}) \\ 0 & 0 & \mathbb{J}_{\mathbf{d}\boldsymbol{\gamma}_f}(\boldsymbol{\gamma}_{f_k}^{n+1}, \mathbf{d}_k^{n+1}) & \mathbb{J}_{\mathbf{d}}(\boldsymbol{\gamma}_{f_k}^{n+1}, \mathbf{d}_k^{n+1}) \end{bmatrix},$$

while the residual is defined as $\mathbf{r}_k^{n+1} = \mathbf{b}^{n+1} - \mathbf{A}(\mathbf{z}_k^{n+1})$.

4.6 Linear solver: the preconditioning strategy

For the sake of simplicity, we rewrite the linear system associated to a single Newton iteration for the implicit scheme (4.8) in the following form:

$$\mathbb{J} \delta \mathbf{z} = -\mathbf{r}, \tag{4.9}$$

where

$$\mathbb{J} = \begin{bmatrix} J_{11} & J_{12} & 0 & 0 \\ J_{21} & J_{22} & 0 & J_{24} \\ J_{31} & 0 & J_{33} & J_{34} \\ 0 & 0 & J_{43} & J_{44} \end{bmatrix}.$$

We take advantage of the GMRES method [95] for the solution of the linear problem (4.9) as $\mathbb{J}$ is non-symmetric and the distribution of the eigenvalues of its spectrum is not known a priori.

We proceed now with the choice of the preconditioner. This is critical in order to ensure the convergence of the linear solver; while this is true in general, it is even more

relevant in the case of monolithic multiphysics problems [56]. Following the choice made in [38], we take a block Gauss-Seidel preconditioner $\mathcal{P}$ obtained by dropping the upper triangular blocks of matrix $\mathbb{J}$, i.e. the off–diagonal blocks, thus obtaining:

$$
\mathcal{P} = \left[\begin{array}{c|c|c|c}
J_{11} & 0 & 0 & 0 \\
\hline
J_{21} & J_{22} & 0 & 0 \\
\hline
J_{31} & 0 & J_{33} & 0 \\
\hline
J & 0 & J_{43} & J_{44}
\end{array} \right] .
$$

The interesting thing is that $\mathcal{P}$ can then be factorized into four model–specific nonsingular matrices, namely $\mathcal{P}_{ion}$, $\mathcal{P}_{pot}$, $\mathcal{P}_{act}$, and $\mathcal{P}_{mec}$ corresponding to the ionic, the potential, the activation, and the mechanics single core models, respectively:

$$
\mathcal{P} = \underbrace{\left[\begin{array}{c|c|c|c}
J_{11} & 0 & 0 & 0 \\
\hline
0 & I & 0 & 0 \\
\hline
0 & 0 & I & 0 \\
\hline
0 & 0 & 0 & I
\end{array} \right]}_{\mathcal{P}_1 = \mathcal{P}_{ion}}
\underbrace{\left[\begin{array}{c|c|c|c}
I & 0 & 0 & 0 \\
\hline
J_{21} & J_{22} & 0 & 0 \\
\hline
0 & 0 & I & 0 \\
\hline
0 & 0 & 0 & I
\end{array} \right]}_{\mathcal{P}_2 = \mathcal{P}_{pot}}
\underbrace{\left[\begin{array}{c|c|c|c}
I & 0 & 0 & 0 \\
\hline
0 & I & 0 & 0 \\
\hline
J_{31} & 0 & J_{33} & 0 \\
\hline
0 & 0 & 0 & I
\end{array} \right]}_{\mathcal{P}_3 = \mathcal{P}_{act}}
\underbrace{\left[\begin{array}{c|c|c|c}
I & 0 & 0 & 0 \\
\hline
0 & I & 0 & 0 \\
\hline
0 & 0 & I & 0 \\
\hline
0 & 0 & J_{43} & J_{44}
\end{array} \right]}_{\mathcal{P}_4 = \mathcal{P}_{mec}} .
$$

The preconditioned version of problem (4.9) then reads:

$$
\begin{cases}
\mathbb{J}\mathcal{P}^{-1}\mathbf{y} = -\mathbf{r} \\
\mathcal{P}\delta\mathbf{z} = \mathbf{y}.
\end{cases}
\tag{4.10}
$$

Since each diagonal block J_{ii} appears in a distinct factor $\mathcal{P}_i$, for $i = 1, \dots, 4$, then physics–specific ad–hoc preconditioners can be efficiently used to approximate its inverse. Indeed, we define the symbolic operation $\delta\mathbf{z} = \mathcal{P}^{-1}\mathbf{y}$ in (4.10) as the application of the following sequential steps

$$
\begin{cases}
\delta\mathbf{z_w} &= J_{11}^{-1}\mathbf{y_w}, \\
\delta\mathbf{z}_V &= J_{22}^{-1}(\mathbf{y}_V - J_{21}\delta\mathbf{z_w}), \\
\delta\mathbf{z_d} &= J_{33}^{-1}(\mathbf{y_d} - J_{31}\delta\mathbf{z_w}), \\
\delta\mathbf{z}_{\gamma_f} &= J_{44}^{-1}(\mathbf{y}_{\gamma_f} - J_{43}\delta\mathbf{z_d});
\end{cases}
\tag{4.11}
$$

the solution of each linear system in (4.11) is carried out by using again the GMRES method and by exploiting Algebraic Multigrid (AMG) preconditioners [18].

4.7   Cardiac cycle

For our simulations we will consider a full heartbeat, by taking the conventional duration of $T = 0.8$ s. With this aim, we take into account for the interaction of the endocardium with the blood by modeling the pressures $p^{endo,LV}$ and $p^{endo,RV}$ as in Eq. (3.11). Before introducing the models used to describe such pressures, we first recall that the heartbeat of each ventricle is conventionally split into four phases (see Fig. 4.1):

1. an isovolumic contraction phase (the red one in Fig. 4.1) in which the endocardial pressures $p^{endo,RV}(t)$ and $p^{endo,LV}(t)$ increase from the End Diastolic Pressure (EDP) to the value measured at the pulmonary artery (RV) or at the aorta (LV). This increment is driven by the early stages of the ventricles contraction;
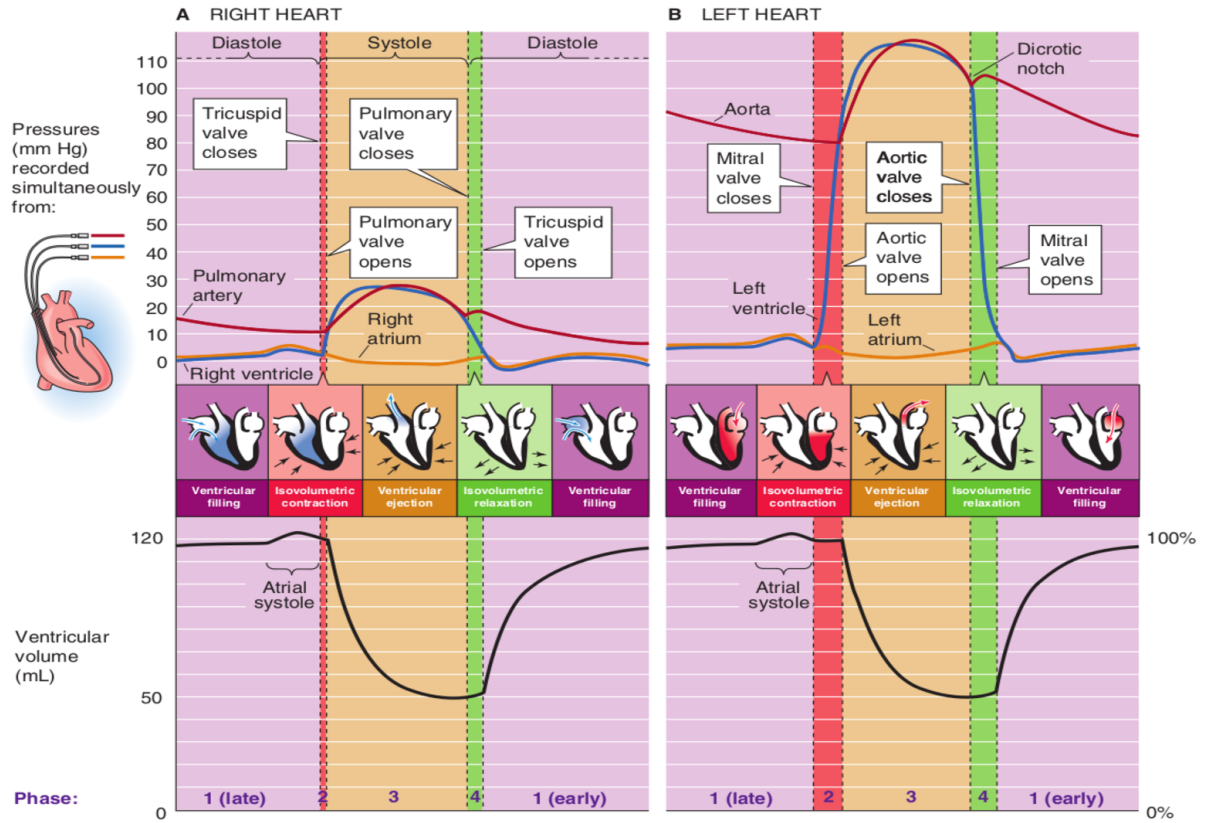
Figure 4.1: The Wiggers diagram of both the left and the right heart depicting the aortic, pulmonary artery, ventricular, and atrial pressures and the ventricular volume, as well as the four phases of the cardiac cycle. Taken from [15].

2. an ejection phase (the one in yellow) characterized by a decrement in the ventricular volumes $V^{endo,LV}(t)$ and $V^{endo,RV}(t)$ due to the contraction of the ventricles. It is called ejection phase since the contraction force the blood to flow out from the ventricular chambers;

3. an isovolumic relaxation (green one) phase during which $p^{endo,LV}(t)$ and $p^{endo,RV}(t)$ decrease as a consequence of the ventricles early relaxation;

4. a filling phase (purple one) starting with the opening of the tricuspid valve (RV) or of the mitral valve (LV) causing an increment of the endocardial volume until $p^{endo,LV}(t)$ and $p^{endo,RV}(t)$ reach the EDP value.

Before proceeding with the definition of a model for an heartbeat it is essential to exploit the joint behaviour of the ventricles. Having a look on Fig. 4.2 we can understand the asynchrony between the right and left ventricle, moreover we can see that the timing of each phase is strictly dependent on the ventricle. Finally, we can rewrite the four phases depicted before to describe the coupled dynamics of the ventricles:

1. we assume to begin in the phase in which both ventricles are in the first isovolumic contraction phase, since we will start our numerical simulations at this time, the right ventricular free wall shortens and moves toward the septum (steps 2, 3 from
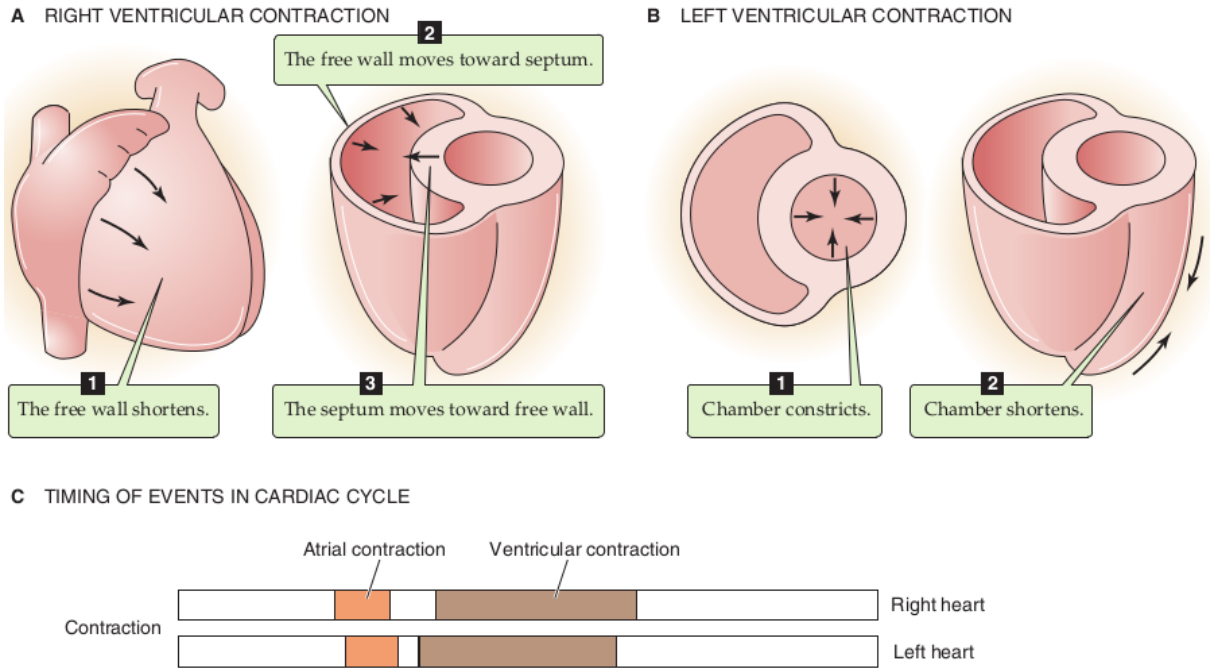
30

Figure 4.2: Comparison between the dynamics of the right and left ventricles. Taken from [15].

Fig. 4.2A), the left ventricular chamber compresses and shortens (steps 1, 2 from Fig. 4.2B);

2. since the pulmonary valve opens before the aortic one (see Fig. 4.3), the RV enters the ejection phase meanwhile the LV is still in the isovolumic phase;

3. the opening of the aortic valve determines the beginning of the ejection phase also for the LV. At this moment both the chambers are ejecting blood. The ventricles keep contracting until there is fluid in them;

4. the first valve to close is the aortic one (see Fig. 4.3) and thus the LV enters in the second isovolumic phase, meanwhile the RV continues the ejection;

5. when the pulmonary valve closes too both ventricles are in the isovolumic relaxation;

6. since the tricuspid opening happens before than the mitral one (see Fig. 4.3), the RV is the first to enter the filling phase;

7. during the filling phase both pressures $p^{endo,LV}(t)$ and $p^{endo,RV}(t)$ are increasing until reaching the EDP value.

Fig. 4.3 helps us understand the valves' dynamics in both right and left part of the human heart. We can now proceed with the description of the models used to reproduce the pressure and volume behaviour inside the ventricles. We will adapt the procedure presented only for the left ventricle in [38] to the case of both the ventricles. As we have seen rewriting the four phases for the bi-ventricle, we have to define a model which have to be able to take into account the fact that the ventricles are not aligned during the cardiac cycle, thus they can be in different phases modelled in a completely distinct way. We
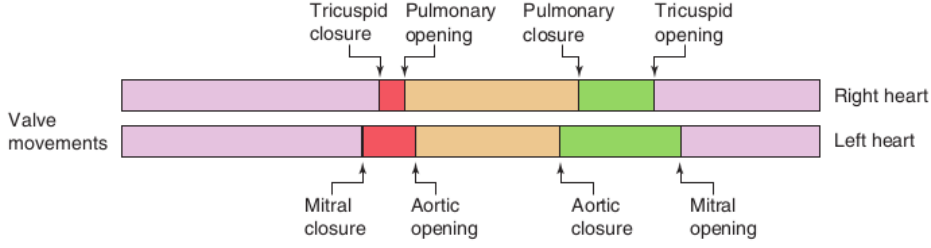
31

Figure 4.3: Valve movements of the right and left ventricles. Taken from [15].

compute the volumes $V^{endo,LV}(t)$ and $V^{endo,RV}(t)$ of each chamber at time n by exploiting the formula

$$V^{endo,LV;\,n} = \int_{\Gamma_0^{endo,LV}} J(\mathbf{d}_h^n)\boldsymbol{\xi}^{LV} \cdot \mathbf{F}^{-T}(\mathbf{d}_h^n)\mathbf{N}\,d\Gamma_0, \qquad (4.12)$$

$$V^{endo,RV;\,n} = \int_{\Gamma_0^{endo,RV}} J(\mathbf{d}_h^n)\boldsymbol{\xi}^{RV} \cdot \mathbf{F}^{-T}(\mathbf{d}_h^n)\mathbf{N}\,d\Gamma_0, \qquad (4.13)$$

which is rigorously derived in [91] and where $\boldsymbol{\xi}^{LV}$ and $\boldsymbol{\xi}^{RV}$ are vectors directed as the centerline of, respectively, the LV and RV. We then model the endocardial pressures $p^{endo,LV}(t)$ and $p^{endo,RV}(t)$ with different 0D models, proposed in [31, 38, 91, 115], for each one of the phases presented above (in the following, we drop the "*endo*" superscript for simplicity and we leave "*LV*" or "*RV*" depending on the ventricle):

1. *Both ventricles in isovolumic phase I*: We assume that both ventricles begin this phase at $t = 0$. At the beginning the endocardial pressures are $p^{LV} = 10$ mmHg and $p^{RV} = 5$ mmHg. At each timestep, we iteratively solve problem (3.11) by updating at each subiteration the pressure in the following manner:

$$p_{k+1}^{i,n+1} = p_k^{i,n+1} + \frac{V_k^{i,n+1} - V^{i,n}}{C_p^i} \qquad k = 0,\dots \qquad (4.14)$$

with $p_0^{i,n+1} = p^{i,n}$, $V_0^{i,n+1} = V^{i,n}$, $i \in \{LV, RV\}$, until the condition $\frac{|V_k^{i,n+1} - V^{i,n}|}{V^{i,n}} < \varepsilon$ is satisfied. The parameter $C_p^i < 0$ has to be tuned, it has to be "sufficiently" large in order for the fixed point algorithm to converge but small "enough" to allow a quick convergence. We know that the first ventricle to start the second phase is the right one, this happens when the pressure $p_{k+1}^{RV,n+1}$ reaches the value $\overline{p^{RV}} = 15$ mmHg.

2. *RV in ejection phase and LV in isovolumic phase I*: For the RV ejection phase we will use a two-element Windkessel model [122] of the form:

$$\begin{cases} C^{RV}\dfrac{dp^{RV}}{dt} = -\dfrac{p^{RV}}{R^{RV}} - \dfrac{dV^{RV}}{dt} & t \in (T^{RV,1}, T^{RV,2}] \\[2mm] p^{RV}(T^{RV,1}) = \overline{p^{RV}} \end{cases} \qquad (4.15)$$

which is solved in the pressure variable with a BDF scheme of order $\sigma = 1$ while the term $\frac{dV^{RV}}{dt}$ is approximated at time $n+1$ as $\frac{V^{RV,n} - V^{RV,n-1}}{\Delta t}$, for simplicity. $T^{RV,1}$ and $T^{RV,2}$ are the initial and final time of this phase, for the right ventricle in this case, while the parameters $C^{RV}, R^{RV} > 0$ represent the capacitance and resistance

of the equivalent electric circuit. At the same time the left ventricular pressure keeps increasing till it reaches the value $\overline{p^{LV}} = 85$ mmHg.

3. *Both ventricles in ejection phase*: Here both the pressures are updated through the Windkessel model:

$$\begin{cases} C^i \dfrac{dp^i}{dt} = -\dfrac{p^i}{R^i} - \dfrac{dV^i}{dt} & t \in (T^{i,1}, T^{i,2}] \\ p^i(T^{i,1}) = \overline{p^i} \end{cases} \tag{4.16}$$

where $i \in \{LV, RV\}$. This phase ends when the (initially negative) term $\frac{dV^{LV}}{dt}$ changes sign.

4. *LV in isovolumic phase II and RV in ejection phase*: The second isovolumic phase for the left ventricle is modelled as the first isovolumic phase. Meanwhile, the RV ejection continues until the (initially negative) term $\frac{dV^{RV}}{dt}$ changes sign.

5. *Both ventricles in isovolumic phase II*: This phase is modelled as the first isovolumic phase and ends when the left ventricular pressure reaches the minimal value of $\overline{\overline{p^{LV}}} = 5$ mmHg.

6. *LV in filling phase and RV isovolumic phase II*: At each time step the left ventricular pressure is linearly increased so that is reaches the EDP value at the final time T. We are aware that this is not fully coherent with the real behaviour of the diastolic phase, but to be able to model it we will have to take into account the contribution of the muscle and the function of the atria. Future work should better address this stages to represent the full heartbeat in a detailed fashion. The RV isovolumic phase finishes when $\overline{\overline{p^{RV}}} = 3$ mmHg.

7. *Both ventricles in filling phase*: At each time step the pressures are linearly increased so that they reach the EDP value at the final time T.

We have here presented an adaptation of a model proposed for the left ventricle only, to the bi-ventricle case, in which the behaviour and the implementation of the various phases of the heartbeat are asynchronous. Therefore, the complexity consists precisely in making accurate choices for mathematical and numerical models of the different stages.

5 Geometry and fibres generation

We now describe the geometry used for the numerical simulation of the integrated electromechanics problem. As anticipated in Chapter 4, we use patient–specific geometry segmented from MRI images as detailed in Section 5.1. Moreover, in Section 5.2, we outline the procedure that is exploited to define the fibres and the sheets fields on previous mesh.

5.1 Patient–specific mesh generation

Our geometry has been generated through a technique called image segmentation, which is the process of locating regions of interest (ROI) in the form of a subset of pixels [45]. Dealing with biomedical applications, this accounts to assign different flags to regions/subsets of the fluid or domain. This result, depending on the properties of the biological material which is to be segmented, can often be achieved through semi–automatic or automatic procedures (see e.g. [32, 54, 114] for arteries and blood vessels and [14, 119] for the Purkinje network), exploiting a large set of different techniques. However, since the development of algorithms for the segmentation of the chambers of the heart [77, 125, 126] is beyond the scope of this work, we refer ourselves to the cardiac atlas taken from [49]. Atlases and statistical models play important roles in the personalization and simulation of cardiac physiology. For the study of the heart, however, the construction of comprehensive atlases and spatio-temporal models is faced with a number of challenges, in particular the need to handle large and highly variable image datasets, the multi-region nature of the heart, and the presence of complex as well as small cardiovascular structures. In [49] it is presented a detailed atlas and spatio-temporal statistical model of the human heart based on a large population of 3D multi-slice computed tomography time sequences, and the framework for its construction. It uses spatial normalization based on non-rigid image registration to synthesize a population mean image and establish the spatial relationships between the mean and the subjects in the population. Temporal image registration is then applied to resolve each subject-specific cardiac motion and the resulting transformations are used to warp a surface mesh representation of the atlas to fit the images of the remaining cardiac phases in each subject. Subsequently, they demonstrate the construction of a spatio-temporal statistical model of shape such that the inter-subject and dynamic sources of variation are suitably separated. The framework is applied to a data set of 138 subjects. The data include a variety of pathologies, this permits their generalization to new subjects and physiological studies. The obtained level of detail and the extendability of the atlas present an advantage over most cardiac models published previously. The resulting geometry is the one in Figure 5.1.
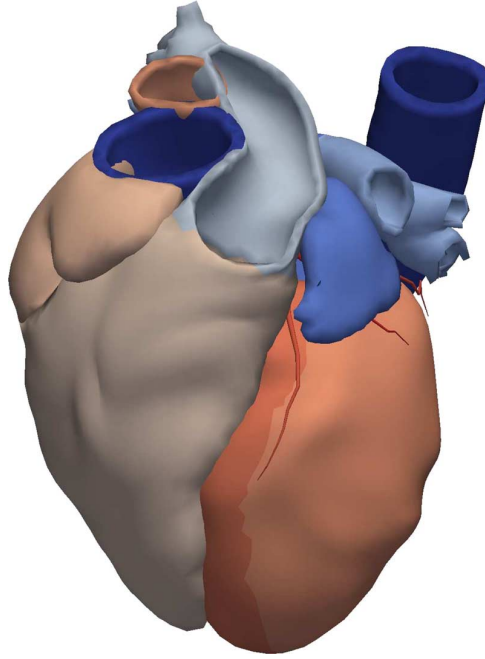
Figure 5.1: The full atlas mesh, corresponding to the synthesized mean image. Different colors indicate different structures. Image taken from [49].

At this point we have an ensemble of surfaces representing a complete human heart. Since we are interested in modelling only the ventricles, we have to extract them from the whole heart. We list below a set of useful softwares to achieve our goal.

1. PARAVIEW [1]: by uploading the heart geometry in this software we are able to apply clips and to obtain from them the surfaces of interest;

2. MESHLAB [25]: here we can proceed cleaning, smoothing and remeshing each part;

3. GID [67]: this software is useful for reconstructing NURBS surfaces from surface meshes letting us to apply some typical geometrical features such as translations, rotations, etc.;

4. GMSH [39]: suitable to merge the various surface meshes, assign them labels, create a volume, obtain a 3D mesh.

We could obtain two different geometries. The two meshes are presented in Figure 5.2 and in Figure 5.3.

5.2 Fibres and sheets distribution

The muscle contractions necessary to pump blood through the body are triggered by electrical signals in the myocardium. The direction of these electric waves depend on the spatial arrangement of myocytes within the myocardium [89], which is termed fibre orientation since it macroscopically resembles a network of fibres within a laminar sheet architecture [104, 61]. Furthermore, ventricular mechanics also depends on fibre
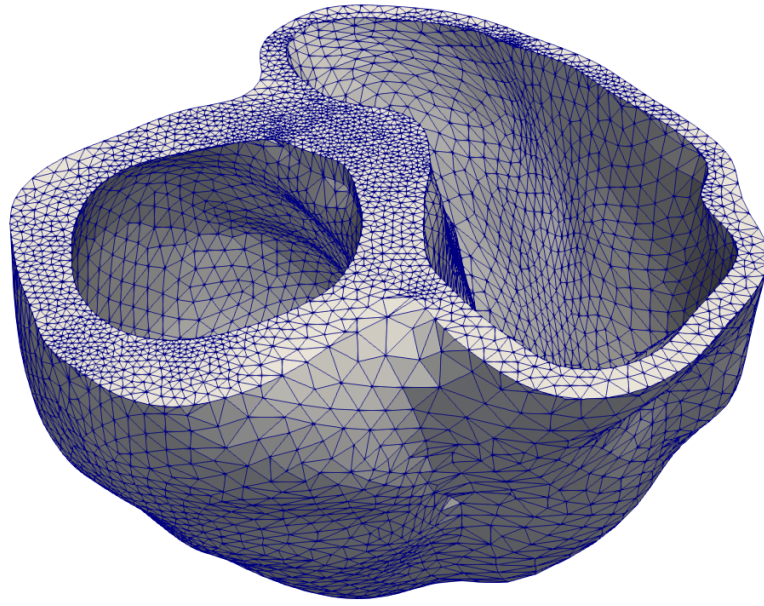
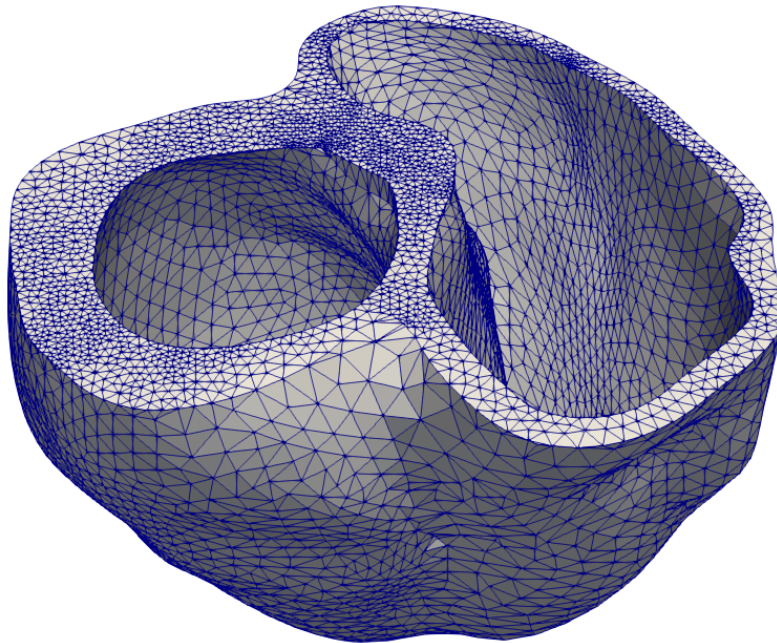Figure 5.2: The resulting biventricle 3D mesh (a).

Figure 5.3: The resulting biventricle 3D mesh (b).

orientation [16]. Thus, in computational studies that simulate electrical wave propagation or mechanical contraction in the myocardium, [112] fibres orientation should be represented accurately so that the chosen model will corroborate with experimental data [50, 88, 117, 120]. One possibility to assign fibre orientation to heart models is based on Diffusion Tensor Imaging (DTI) data, yet few alternative methodologies exist if DTI data
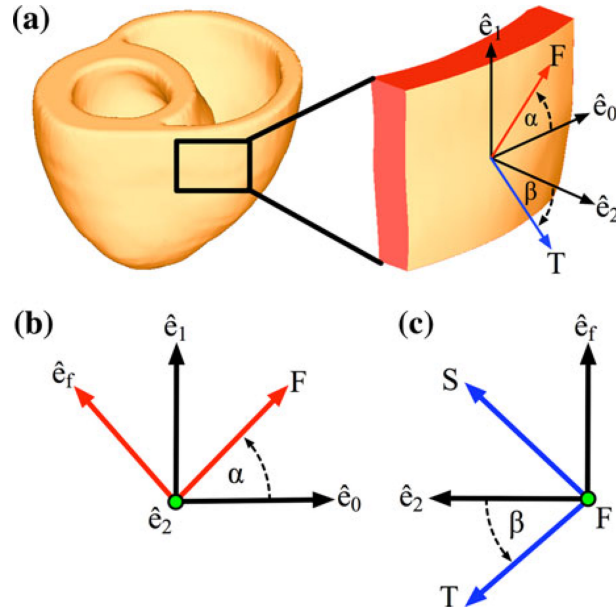
Figure 5.4: The coordinate system used for assigning fibre orientation to computational models of the ventricles. (a) The longitudinal fibre (F) and transverse (T) directions with respect to the circumferential ($\hat{e}_0$), apicobasal ($\hat{e}_1$) and transmural ($\hat{e}_2$) axes derived from the Laplace solutions. (b) The rotation of F, and the rotation of T, in the axis system with respect to the input angles α and β, respectively. The green dots represent axes pointing out of the page. Image taken from: [11].

is noisy or absent.

Traditionally, rule-based algorithms parameterize the transmural direction based on the minimal distance between the endocardial and epicardial surfaces, and define the apicobasal direction parallel to the long axis of the heart. This approach has shown some success in ventricular models with basic geometries [13, 80]. However, minimal distance parameterizations do not guarantee the absence of singularities in the minimal distance function throughout the entire myocardium.

Here we follow the *Laplace–Dirichlet Rule-Based* (LDRB) algorithm of [11] to perform this task. This class of algorithms is addressed as "rule-based" since it produces mathematical descriptions for fibre configuration with rules formulated on the basis of observations from histology and DTI. A common characteristic of all rule-based algorithms is that the transmural and apicobasal directions throughout the entire myocardium of a model need to be parametrized in order to systematically assign orthotropic fibre orientation.

We decide to take advantage of this algorithm since the use of a Laplace–Dirichlet method lets us to simultaneously define the transmural and apicobasal directions for the entire myocardium (Figure 5.4). The main difference between this method and minimal distance parametrizations, is that this algorithm exploits the continuity properties of the harmonic solutions to Laplace's equation with Dirichlet boundary conditions to ensure that the transmural and apicobasal directions change smoothly and continuously throughout the entire myocardium, even in models with complex geometries, this is why this procedure is preferable in our case, since we consider a patient-specific geometry. It is worthy to highlight that since we need a fluid and continuous changing in the fibres orientation, particularly in the septum and its junctions with the LV and the RV, in [11]

they propose to use bidirectional spherical linear interpolation to interpolate fibre orientations within the myocardium, this choice guarantees that fibre orientation will change smoothly throughout the entire myocardium.

The LDRB algorithm is based on the following properties of myocardial fibre orientation derived from histological and DTI data:

- The longitudinal fibre direction in the ventricular walls is parallel to the endocardial and epicardial surfaces.

- The longitudinal fibre direction rotates clockwise throughout the ventricular walls from the endocardium ($+\alpha$) to the epicardium ($-\alpha$), where α is the helical angle with respect to the counterclockwise circumferential direction in the heart when looking from the base towards the apex.

- The longitudinal fibre direction in papillary muscles and trabeculae is parallel to the long axis of these structures.

- The transverse fibre direction is perpendicular to the longitudinal fibre direction and is defined by the angle β, where β is the angle with respect to the outward transmural axis of the heart. For simplicity, β is assumed to vary transmurally from $-\beta$ on the endocardium to $+\beta$ on the epicardium.

- The sheet normal is orthonormal to the longitudinal and transverse fibre directions.

The LDRB algorithm also requires the definition of the following surfaces in order to assign Dirichlet boundary conditions:

- Γ_0^{apex}, the apex of the ventricles

- Γ_0^{base}, the base of the ventricles

- Γ_0^{epi}, the epicardial surface of the ventricles

- $\Gamma_0^{endo,LV}$, the endocardial surface of the LV

- $\Gamma_0^{endo,RV}$, the endocardial surface of the RV

In this case we can assume $\Gamma_0^{epi} = \Gamma_0^{epi,LV} \cup \Gamma_0^{epi,RV}$, since in this method it is not necessary to subdivide the epicardium to define the fibres configuration. It is important to note that Γ_0^{apex} corresponds to a point taken at the apex of the bi-ventricle. Now we need to solve four Laplace equations applying prescribed boundary conditions:

$$
\begin{cases}
-\Delta \psi_{ab} = 0 & \text{in } \Omega_0 \\
\psi_{ab} = 1 & \text{on } \Gamma_0^{base} \\
\psi_{ab} = 0 & \text{on } \Gamma_0^{apex}
\end{cases}
$$

$$
\begin{cases}
-\Delta \phi_{lv} = 0 & \text{in } \Omega_0 \\
\phi_{lv} = 1 & \text{on } \Gamma_0^{endo,LV} \\
\phi_{lv} = 0 & \text{on } \Gamma_0^{epi} \cup \Gamma_0^{endo,RV}
\end{cases}
$$

$$\begin{cases} -\Delta\phi_{rv} = 0 & \text{in } \Omega_0 \\ \phi_{rv} = 1 & \text{on } \Gamma_0^{endo,V} \\ \phi_{rv} = 0 & \text{on } \Gamma_0^{epi} \cup \Gamma_0^{endo,LV} \end{cases}$$

$$\begin{cases} -\Delta\phi_{epi} = 0 & \text{in } \Omega_0 \\ \phi_{epi} = 1 & \text{on } \Gamma_0^{epi} \\ \phi_{epi} = 0 & \text{on } \Gamma_0^{endo,LV} \cup \Gamma_0^{endo,RV} \end{cases}$$

We recall that since $\psi_{ab}, \phi_{epi}, \phi_{lv}$ and ϕ_{rv} are harmonic solutions taking values between 0 and 1, they are continuous and thus we can proceed taking their gradient to define the normal direction to each surface of interest. By taking the gradient of the Laplace solutions, $\nabla\psi_{ab}$ is used to define the apicobasal direction, and $\nabla\phi_{lv}$, $\nabla\phi_{rv}$, and $\nabla\phi_{epi}$ are used to find the transmural direction, since the gradient is directed as the normal to the surface. Now we need a function which takes as inputs, for a given point in Ω_0, a vector $\nabla\psi_{ab}$ along with either $\nabla\phi_{lv}$, $\nabla\phi_{rv}$ or $\nabla\phi_{epi}$, then yields a right-handed axis system ($\mathbf{Q} = \begin{bmatrix} \hat{\mathbf{e}}_0 & \hat{\mathbf{e}}_1 & \hat{\mathbf{e}}_2 \end{bmatrix}$) where $\hat{\mathbf{e}}_0$ is oriented in the circumferential direction, $\hat{\mathbf{e}}_1$ in the apicobasal direction, and $\hat{\mathbf{e}}_2$ in the transmural direction. To understand better the procedure we can compute, for example, $\hat{\mathbf{e}}_0$, $\hat{\mathbf{e}}_1$, $\hat{\mathbf{e}}_2$ given $\nabla\psi_{ab}$ and $\nabla\phi_{epi}$.

$$\hat{\mathbf{e}}_1 = \frac{\nabla\psi_{ab}}{\|\nabla\psi_{ab}\|}$$
$$\hat{\mathbf{e}}_2 = \frac{\nabla\phi_{epi} - (\hat{\mathbf{e}}_1 \cdot \nabla\psi_{ab})\,\hat{\mathbf{e}}_1}{\|\nabla\phi_{epi} - (\hat{\mathbf{e}}_1 \cdot \nabla\psi_{ab})\,\hat{\mathbf{e}}_1\|}$$
$$\hat{\mathbf{e}}_0 = \hat{\mathbf{e}}_1 \times \hat{\mathbf{e}}_2$$

All the other directions can be calculated in the same way given $\nabla\psi_{ab}, \nabla\phi_{lv}, \nabla\phi_{rv}$ and $\nabla\phi_{epi}$. Due to the manner in which we set up the Laplace equations, the various gradients are perpendicular and aligned in the apicobasal and transmural directions.

At this point we have to find an orthonormal coordinate system $\begin{bmatrix} \mathbf{f} & \mathbf{s} & \mathbf{t} \end{bmatrix}$, where $\mathbf{f}$ is the longitudinal direction, $\mathbf{s}$ is the sheet normal and $\mathbf{t}$ is the transverse direction. For a given point in Ω, the direction $\mathbf{f}$ is obtained by rotating $\mathbf{Q}$ around $\hat{\mathbf{e}}_2$ by the angle α at that point (Figure 5.4b):

$$\mathbf{R}_{\hat{\mathbf{e}}_2}^{\alpha} = \mathbf{Q} \begin{bmatrix} \cos(\alpha) & -\sin(\alpha) & 0 \\ \sin(\alpha) & \cos(\alpha) & 0 \\ 0 & 0 & 1 \end{bmatrix} \mathbf{Q}^{\mathbf{T}}$$

$$\begin{bmatrix} \mathbf{f} & \hat{\mathbf{e}}_{\mathbf{f}} & \hat{\mathbf{e}}_2 \end{bmatrix} = \mathbf{R}_{\hat{\mathbf{e}}_2}^{\alpha} \mathbf{Q}$$

We follow the same procedure to generate the $\mathbf{s}$ and $\mathbf{t}$ directions. Given a point of Ω, $\mathbf{s}$ and $\mathbf{t}$ are produced by rotating the axis system $\begin{bmatrix} \mathbf{f} & \hat{\mathbf{e}}_{\mathbf{f}} & \hat{\mathbf{e}}_2 \end{bmatrix}$ around F by the angle β at that point (Figure 5.4c):

$$\mathbf{R}_{\mathbf{F}}^{\beta} = \begin{bmatrix} \mathbf{f} & \hat{\mathbf{e}}_{\mathbf{f}} & \hat{\mathbf{e}}_2 \end{bmatrix} \begin{bmatrix} 1 & 0 & 0 \\ 0 & \cos(\beta) & \sin(\beta) \\ 0 & -\sin(\beta) & \cos(\beta) \end{bmatrix} \begin{bmatrix} \mathbf{f} \\ \hat{\mathbf{e}}_{\mathbf{f}} \\ \hat{\mathbf{e}}_2 \end{bmatrix}$$

$$\begin{bmatrix} \mathbf{f} & \mathbf{s} & \mathbf{t} \end{bmatrix} = \mathbf{R}_{\mathbf{F}}^{\beta} \begin{bmatrix} \mathbf{f} & \hat{\mathbf{e}}_{\mathbf{f}} & \hat{\mathbf{e}}_2 \end{bmatrix}$$

The angles α and β are expressed in degrees and they are functions of d the transmural depth normalized from 0 to 1.

$$\begin{aligned} \alpha_s(d) &= \alpha_{endo}(1-d) - \alpha_{endo}\, d \\ \alpha_w(d) &= \alpha_{endo}(1-d) - \alpha_{epi}\, d \\ \beta_s(d) &= \beta_{endo}(1-d) - \beta_{endo}\, d \\ \beta_w(d) &= \beta_{endo}(1-d) - \beta_{epi}\, d \end{aligned}$$

To interpolate the fibre orientation axes continuously throughout the myocardium we pass through a straight-forward adaptation of quaternion spherical linear interpolation, also known as "slerp", to account for the bidirectional nature of fibres' distribution. Quaternions are a generalization of complex numbers, where every right-handed axys $\mathbf{Q_A}$ can be transformed into a unit quaternion $\mathbf{q_A}$ and vice versa.

Here we present the spatial discretization of a general Laplace problem with mixed boundary conditions using the finite dimensional space $\mathcal{X}_h^1$ introduced in Chapter 4. We first define the problem. Let $\Omega_0 \subset \mathbb{R}^3$ be a bounded domain in which we consider this boundary-value problem

$$\begin{cases} -\Delta u = 0 & \text{in } \Omega_0 \\ u = g & \text{on } \Gamma_D \\ \dfrac{\partial u}{\partial n} = 0 & \text{on } \Gamma_N \end{cases}$$

where $\Gamma_D \cup \Gamma_N = \partial \Omega_0$ is the boundary with $\Gamma_D \cap \Gamma_N = \emptyset$. We assume that $g \in \mathrm{H}^{1/2}(\Gamma_D)$, having denoted by $\mathrm{H}^{1/2}(\Gamma_D)$ the space of functions of $\mathrm{L}^2(\Gamma_D)$ that are traces of functions of $\mathrm{H}^1(\Omega_0)$. We suppose to know a function R_g, called *lifting of the boundary data*, such that

$$R_g \in \mathrm{H}^1(\Omega_0), \quad R_g|_{\Gamma_D} = g$$

We set $\mathring{u} = u - R_g$ and we begin by observing that $\mathring{u}|_{\Gamma_D} = u|_{\Gamma_D} - R_g|_{\Gamma_D} = 0$, that is $\mathring{u} \in V = \mathrm{H}^1_{\Gamma_D}(\Omega_0)$, having denoted by $\mathrm{H}^1_{\Gamma_D}(\Omega_0)$ the space of functions of $\mathrm{H}^1(\Omega_0)$ which are zero on Γ_D. Moreover, we denote by $\{\psi_i\}_{i=1}^{N^{\mathrm{dof}}}$ a basis of $\mathcal{X}_h^1$ with $N^{\mathrm{dof}} = \dim(\mathcal{X}_h^1)$. The projection of the solution $\mathring{u}$ on the finite space $\mathcal{X}_h^1$ can hence be written as $\mathring{u}_h = \sum_{j=1}^{N^{\mathrm{dof}}} \mathring{u}_j \psi_j$ and consequently we get the following space discretization

$$\text{find } \mathring{u}_h \in V : \int_{\Omega_0} \nabla \mathring{u}_h \cdot \nabla \psi_i \, d\Omega_0 = -\int_{\Omega_0} \nabla R_{g_h} \cdot \nabla \psi_i \, d\Omega_0 \quad \forall\, i = 1, \dots, N_V^{\mathrm{dof}},$$

By expressing $\mathring{u}_h$ in terms of the basis $\{\psi_j\}$, we have $\mathring{u}_h = \sum_{j=1}^{N^{\mathrm{dof}}} \mathring{u}_j \psi_j$, we end up with the following linear system (for details see [81])

$$\mathrm{A}\mathbf{u} = -\mathrm{B}\mathbf{g}$$

In Figures 5.5 and 5.6 we show the solutions to the Laplace–Dirichlet scalar fields obtained thanks to Finite Element Method.

Following the fibres orientation presented in [5], for a similar patient-specific bi-venticle geometry, we take two different settings for α_{endo}, α_{epi}, β_{endo} and β_{epi}, these will result extremely similar to the one found in human ventricles (see for examples the fibres obtained in [116]):
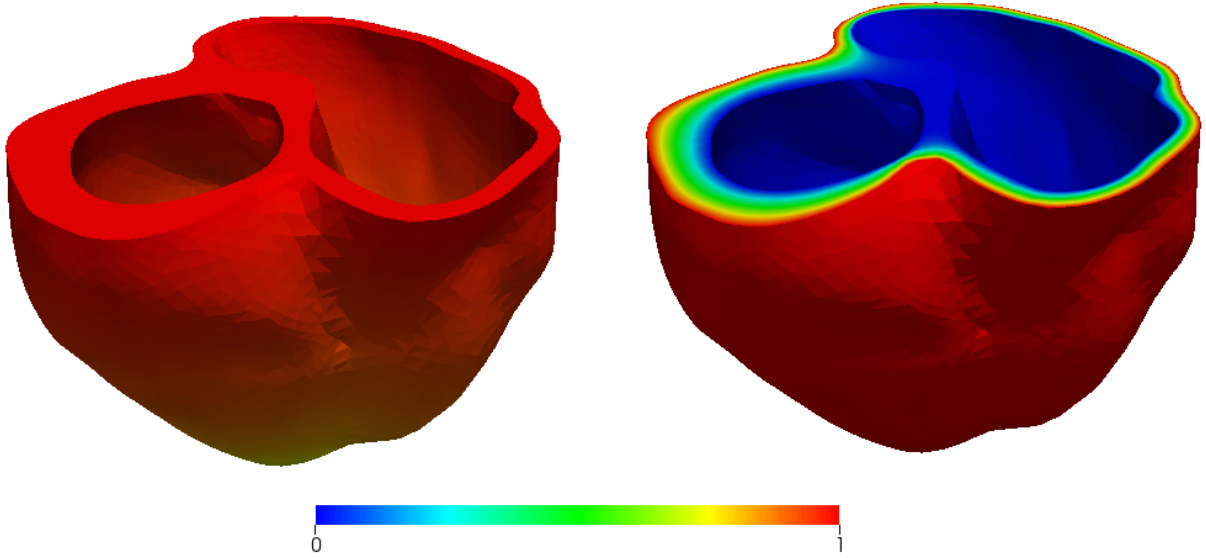
Figure 5.5: Solutions to Laplace's equation with the Dirichlet boundary conditions. From left to right we have ψ_{ab} and ϕ_{epi}.
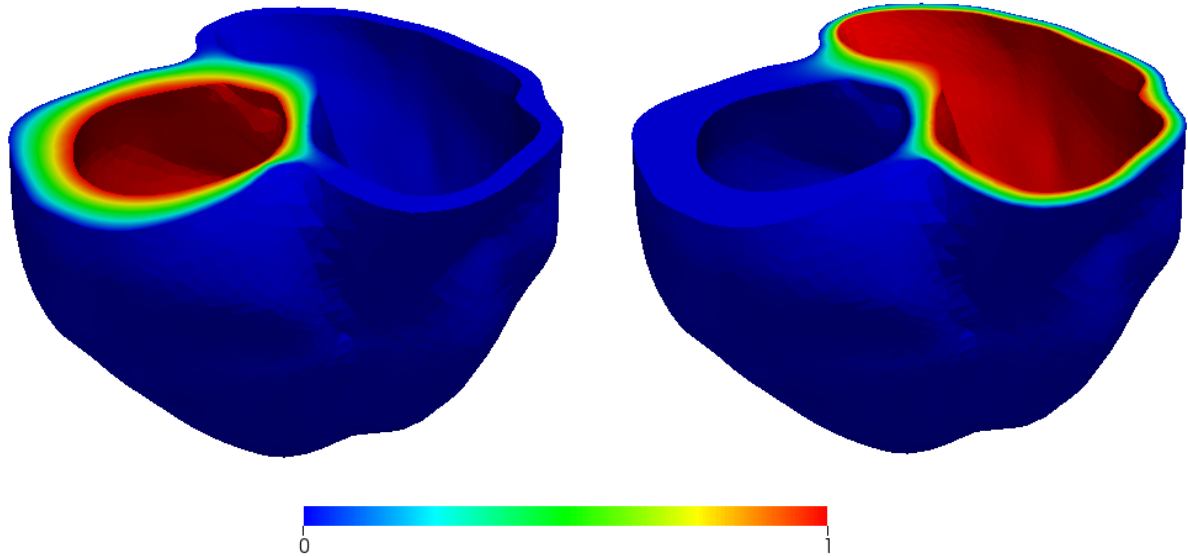

Figure 5.6: Solutions to Laplace's equation with the Dirichlet boundary conditions. From left to right we have ϕ_{lv} and ϕ_{rv}.

1. $\alpha_{endo} = 60°$, $\alpha_{epi} = -60°$, $\beta_{endo} = 80°$, $\beta_{epi} = -80°$;

2. $\alpha_{endo} = 50°$, $\alpha_{epi} = 130°$, $\beta_{endo} = 120°$, $\beta_{epi} = 80°$.

By applying this method to our two different geometries with both settings we obtain fibres and sheets in Figures 5.7, 5.8, 5.9 and 5.10.

Confronting the two chosen setting on each geometry, we can notice that even if, at first glance, they seem to reproduce a similar fibres orientation both at the endocardium

41
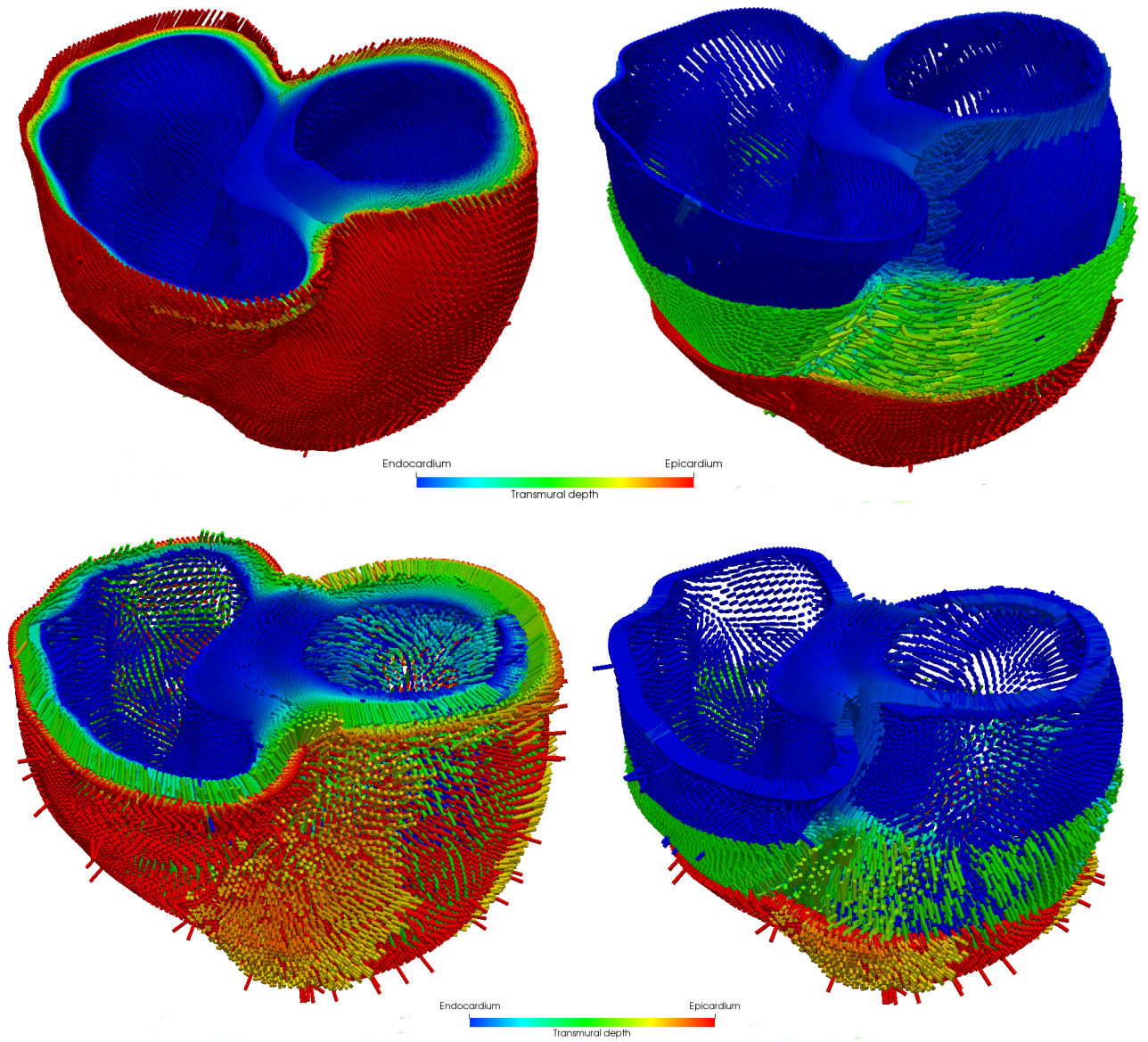
Figure 5.7: Fibres and sheets on mesh (a) with setting 1.

and at the epicardium, having a closer look at the layered figures we can observe a different direction transmurally. However, switching from setting 1 to setting 2 the sheets configuration changes completely. Albeit changing geometry does not affect the fibres and sheets orientation at the epicardium, it influences the transmural directions in the septum.
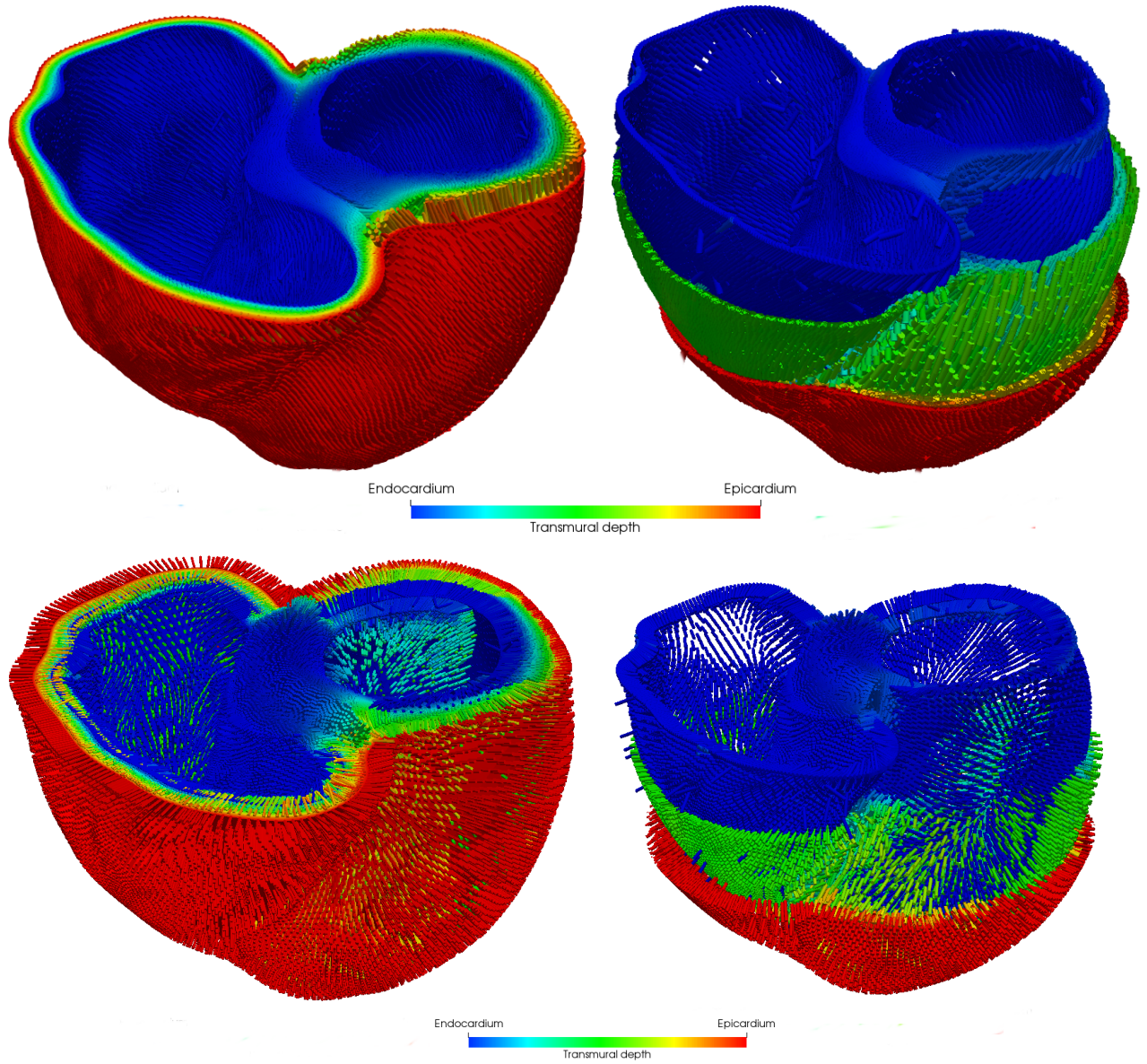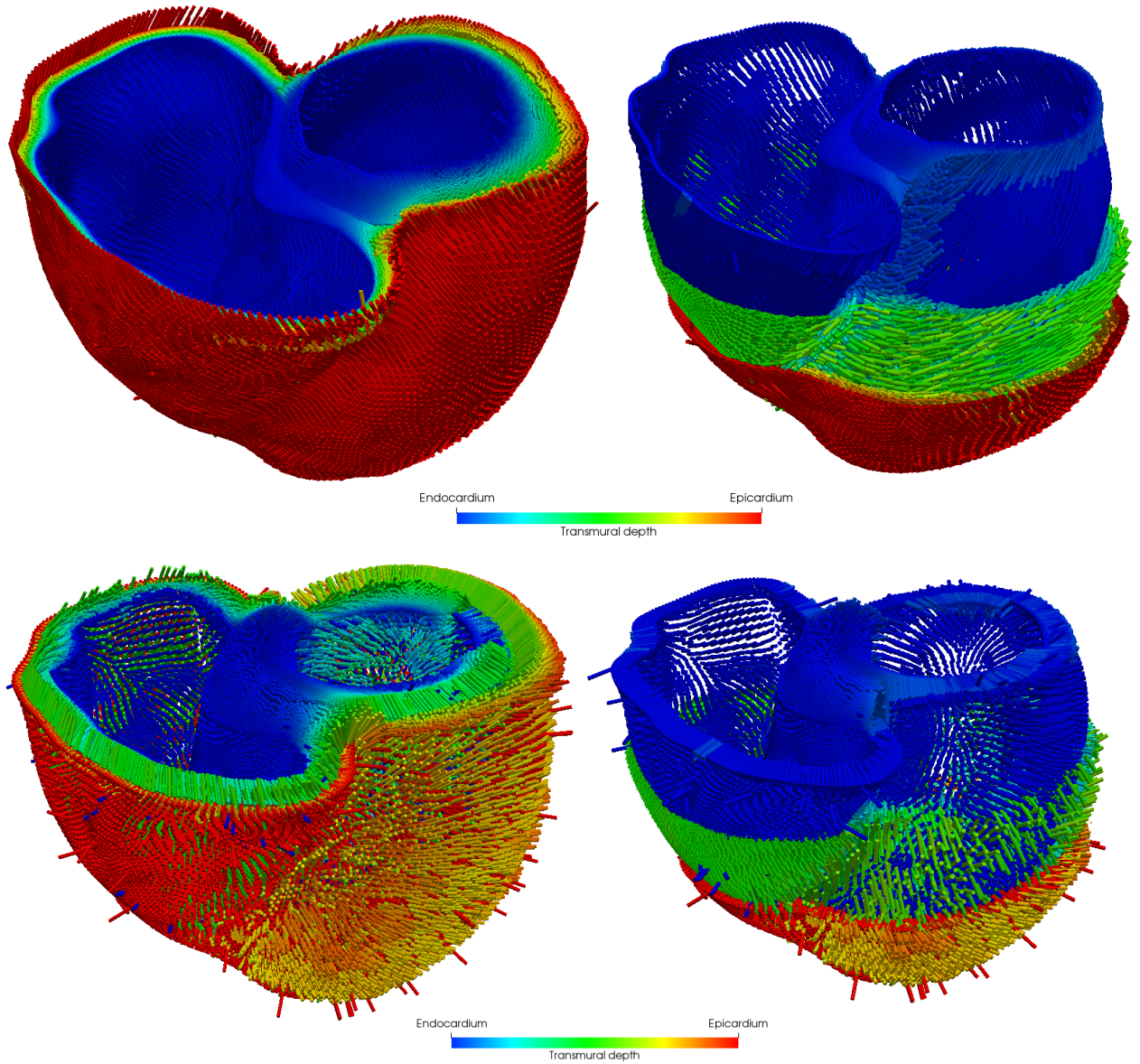
Figure 5.8: Fibres and sheets on mesh (a) with setting 2.

Figure 5.9: Fibres and sheets on mesh (b) with setting 1.
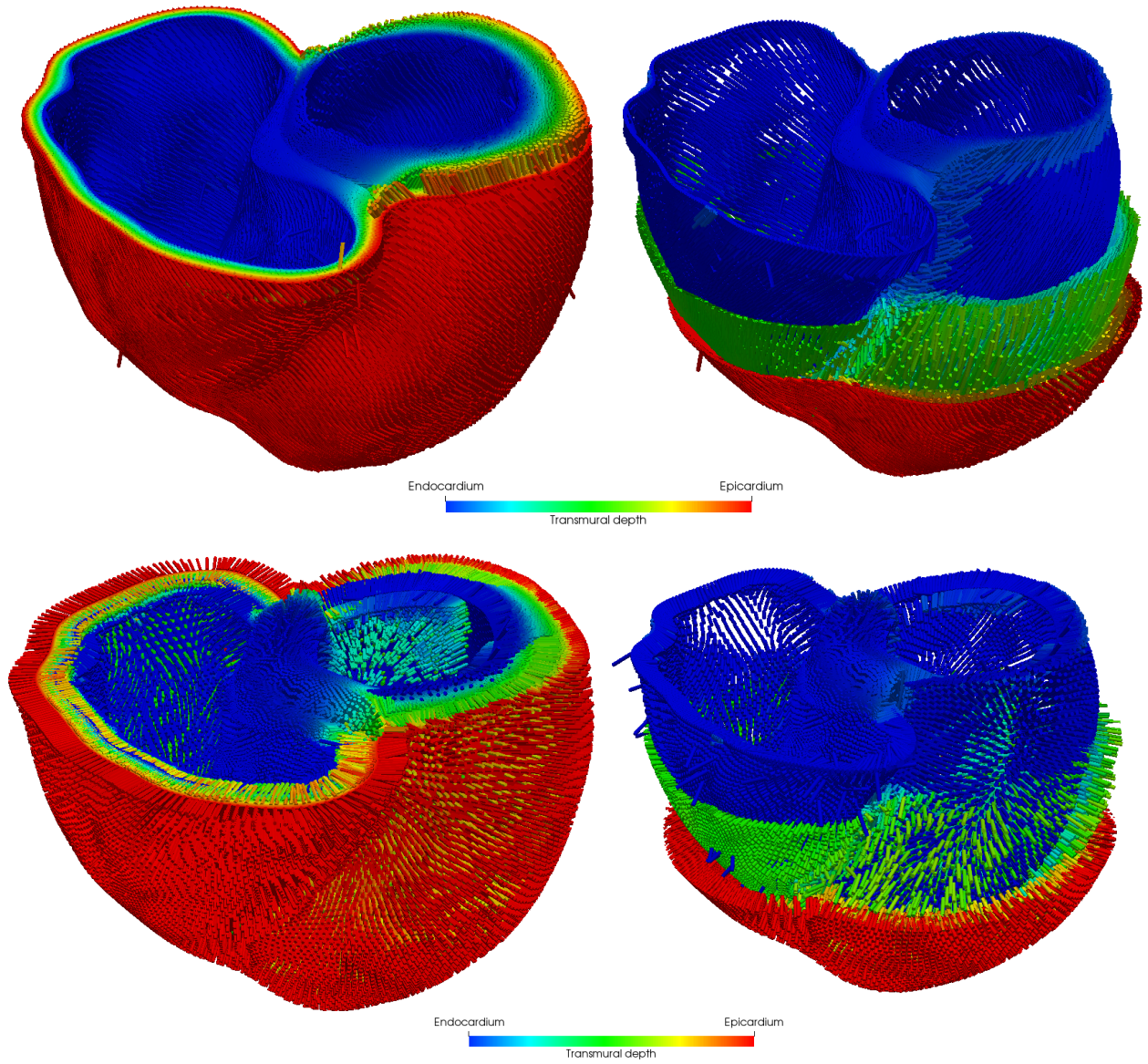
Figure 5.10: Fibres and sheets on mesh (b) with setting 2.

6 Numerical simulations

In this chapter, we provide a broad range of numerical simulations we have run in order to asses the validity of the main assumptions detailed in the previous chapter. We start with Sec. 6.1 by outlining the numerical setting used to carry out the simulations. We will proceed by explaining in Sec. 6.2 how the electrical signal is driven through the myocardium and we will exhibit our result regarding the cardiac action potential propagation and the calcium concentration. Finally, we will complete the results' presentation by discussing in Sec. 6.3 the simulations on the mechanical behaviour of our ventricles, highlighting the differences due to the fibres and sheets configurations. We recall that we are solving an electromechanical problem on bi-ventricle geometries, this means that electrophysiology and mechanics are strictly coupled one to the other. We will subdivide the electrophysiology and mechanics results just to have the possibility to underline different characteristics belonging to each core model.

6.1 Numerical setting

The following numerical simulations are carried out on the meshed geometries presented in Sec 5.1 as Figs. 5.2 and 5.3. The monodomain, the activation, and the mechanical equations are approximated with $\mathbb{P}^1$ elements; however, the ionic model is solved in the degrees of freedom determined by the discretization of the monodomain equations (in our case the vertices of the tetrahedrons). We obtain a linear system of size $M = 8 \times N_h$. Regarding time discretization, we proceed with a second order BDF scheme ($\sigma = 2$), this to maximize the convergence order while ensuring A-stability [85]. The time-step used in the simulations is 5.0×10^{-5}. We show in Tables 6.1 and 6.2 the informations regarding each mesh used in the simulations and the size of the monolithic linear systems.

Geometry	Mesh	h	# Vertices	# Elements
Patient-specific (Fig. 5.2)	(a)	4.04 mm	7718	27636
Patient-specific (Fig. 5.3)	(b)	4.11 mm	7688	27479

Table 6.1: Information about the meshes of the patient-specific geometries: average edge length h, number of vertices and number of elements.

Mesh	M	# CPUs
(a)	61744	18
(b)	61504	18

Table 6.2: Size M of the monolithic linear system and number of threads used.

To solve the monolithic problem we implement and use the models in LifeV[1], an open–source finite element library. We applied the numerical methods implemented in a
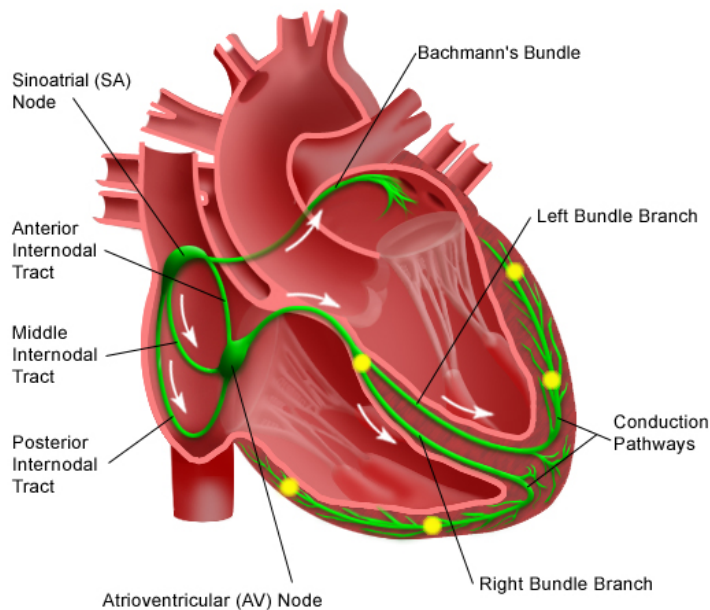
---

[1] https://www.lifev.org/

Figure 6.1: Purkinje network in the human heart. In yellow we have highlighted the five points in which we apply an impulse. Adapted from http://www.stanfordchildrens.org/.

High Performance Computing framework and the computation are performed using Piz Daint, a Cray XC50/XC40 supercomputer installed at the Swiss National Supercomputing Center (CSCS)[2]. For the solution of the non linear system (4.7) we exploit the Newton method, as detailed in Section 4.6, setting a maximum number of 5 iterations per time step. As stopping criterion we use the relative residual, with a tolerance equal to 10^{-7}. As preconditioning technique we follow what anticipated in Section 4.6. At each Newton iteration (4.8) we use the GMRES method to invert the blocks J_{ii}, $i = 1, \ldots, 4$ together with AMG preconditioners by taking into account the number of underlying PDEs of each block; we exploit the ML package [36] of the Trilinos library [46] by performing three sweeps of the Gauss–Seidel algorithm for pre– and post–smoothing, while the solution on the coarsest level is obtained through an LU factorization. We consider the relative residual as stopping criterion for the GMRES method, with a tolerance equal to 10^{-8}.

6.2 Numerical results: electrophysiology

The cardiac action potential is spread along the endocardium of each ventricle thanks to the Purkinje fibres (see Fig. 6.1). These are specialised conducting fibres composed of electrically excitable cells which have the ability of conducting the impulse more quickly and efficiently than any other cells in the heart. An essential property, to underline to model in a right way this behaviour, is that the Purkinje fibres allow the heart's conduction system to create synchronized contractions of its ventricles, and are therefore crucial for maintaining a consistent heart rhythm.

As a consequence, we simulate the cardiac action potential spreading following the
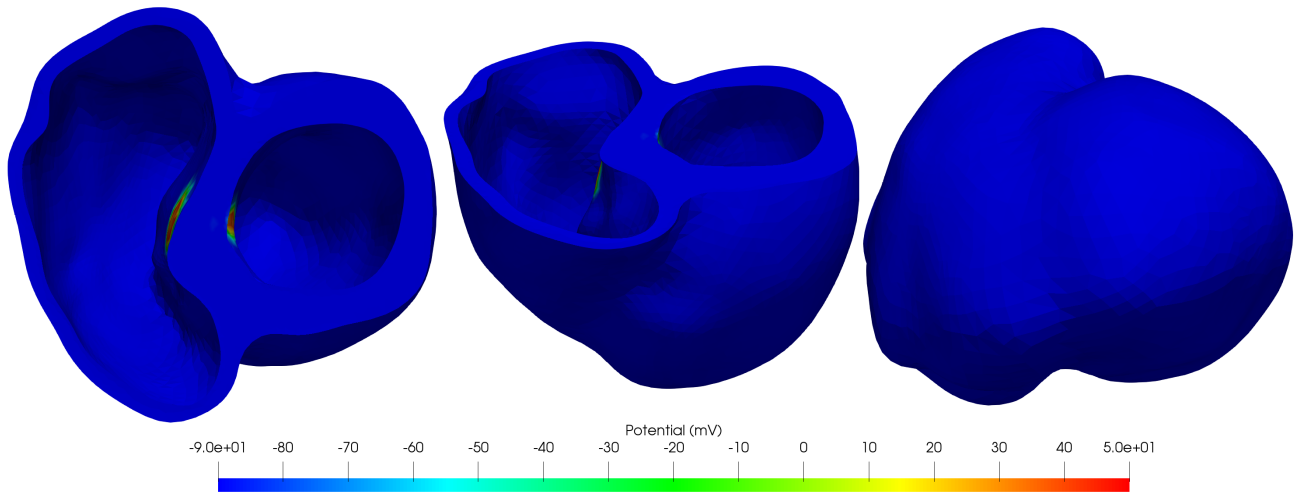
---

[2]https://www.cscs.ch/

47

Figure 6.2: Transmembrane potential at $t = 0.002$.
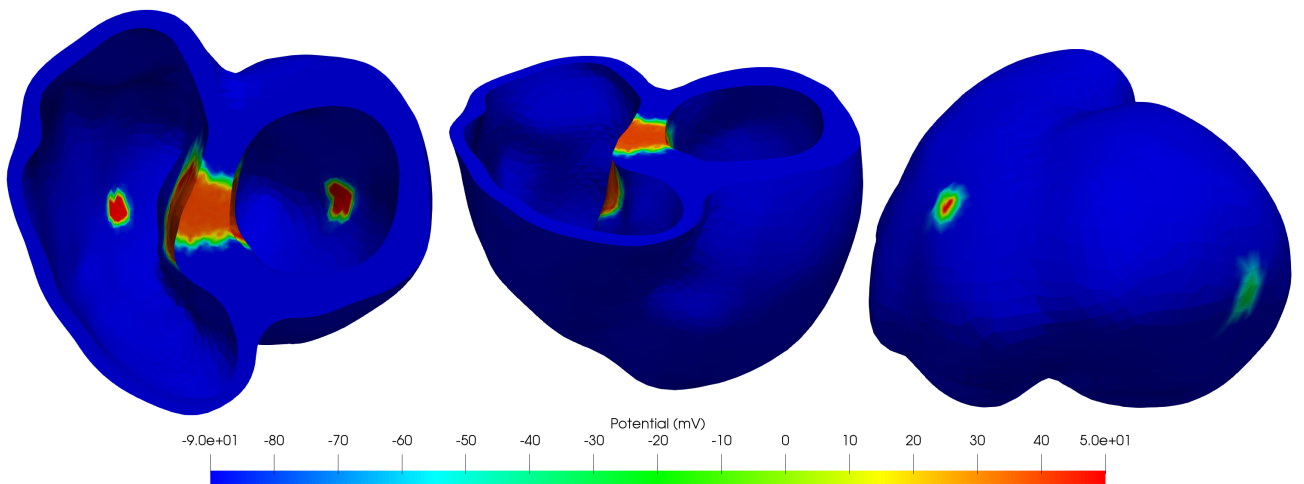

Figure 6.3: Transmembrane potential at $t = 0.0037$.

conduction pathways defined by the Purkinje fibres implementing a way to set delayed stimuli along the geometry. We apply a 2-milliseconds long stimulum at five points on the endocardium of the geometry (a) (see Figs. 6.2, 6.3 and 6.4) (we will show only the simulations carried out on the mesh (a) with setting 1 since the comparison with the others does not highlight remarkable differences) at different time steps ($t = 0$ s, $t = 2.5e^{-3}$ s, $t = 5.0e^{-3}$ s) which will approximate the delay due to the propagation velocity of the impulse along the Purkinje fibres [53]. Even if this strategy is not totally realistic, since the Purkinje network activates asynchronously hundreds of cells [90, 118], it provides a physically meaningful behaviour.

As we can see from our simulations the first point to be excited is situated in the middle of the septum (see Fig. 6.2), in fact, following the conduction pathways in Fig. 6.1, the signal coming from the sinoatrial node stimulates the ventricles wall through the septum. Following the Purkinje fibres, the next impulse is set near the apex of each ventricle. Observing the Fig. 6.3 we notice that meanwhile we apply the second impulse, most of the septum is activated. We decide to locate our last stimulus on the upper part of the
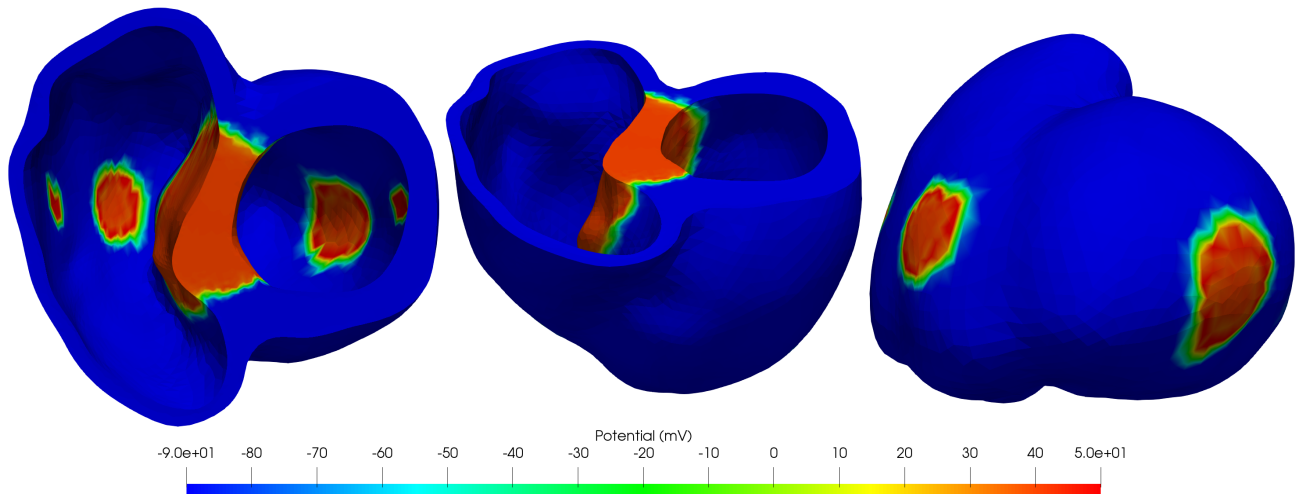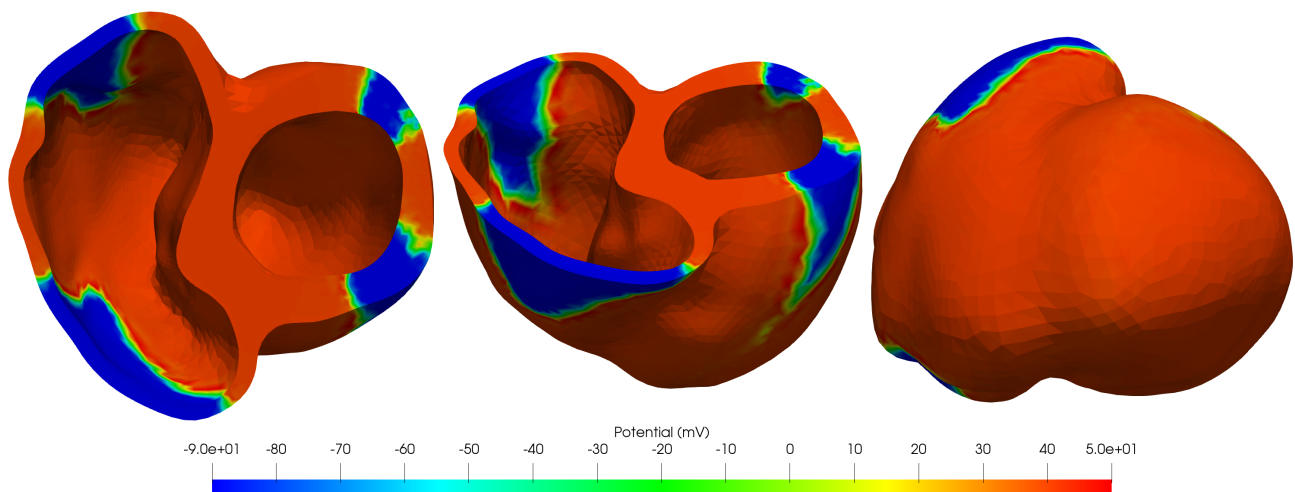
Figure 6.4: Transmembrane potential at $t = 0.0064$.

Figure 6.5: Transmembrane potential at $t = 0.012$.

free wall of the right and left ventricle (see Fig. 6.4). At this time all the septum is excited and the potential has passed through the endocardium and begins to spread in the epicardium. In the last Fig. 6.5, we can observe how both the ventricles are mostly activated by the transmembrane potential.

We recall that since we are using piecewise linear polynomials of degree 1 and a coarse mesh we tend to have a conduction velocity which is overestimated [12, 30]. To overcome this problem we can, for example, refine the mesh (a) keeping piecewise linear polynomials of degree 1. In Figs. 6.6, 6.7, 6.8 and 6.9 we have applied the same electrical impulses in a refined mesh (a) ($h = 0.97$, #Vertices = 49674 #Elements = 221088). We proved the fact that the conduction velocities are overestimated when the mesh size is not sufficiently small. However, even if this difference is significant in the electrophysiology characteristic time scale, it will not affect the mechanics, this thanks to the multiscale nature of the integrated problem.

Another important result to present is the Ca^{2+} concentration, solution of (3.2). As we have highlighted in Sec. 3.3, the mechanical activation is driven by the presence of
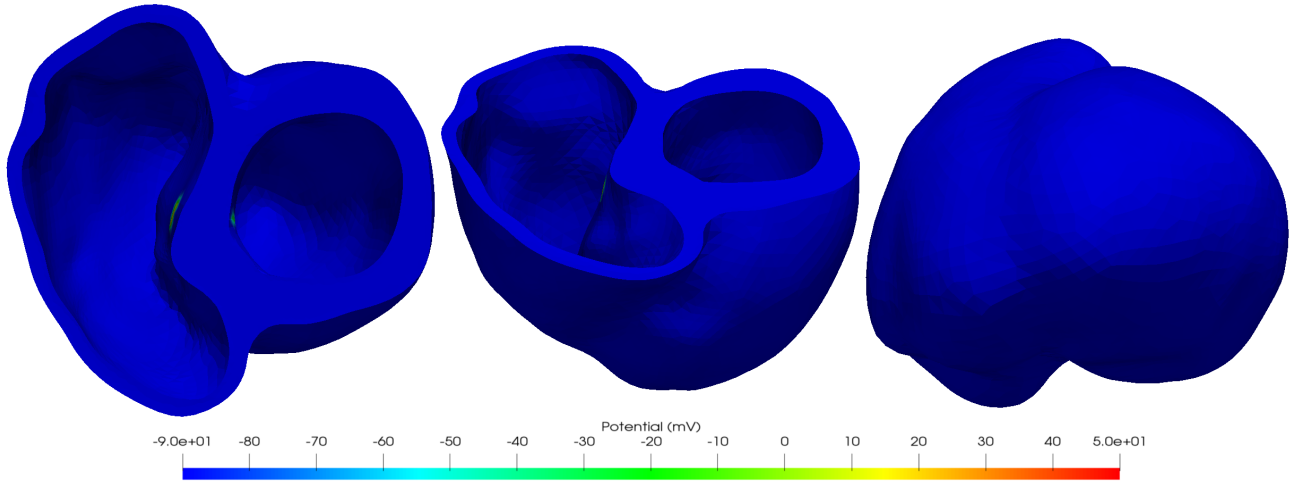
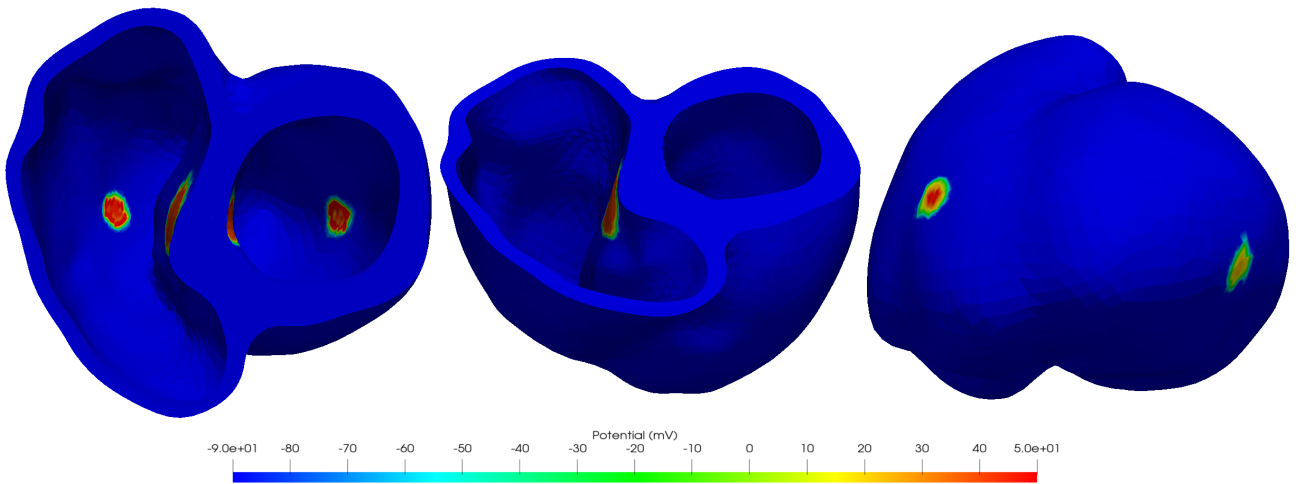Figure 6.6: Transmembrane potential in refined mesh at $t = 0.002$.

Figure 6.7: Transmembrane potential in refined mesh at $t = 0.0037$.

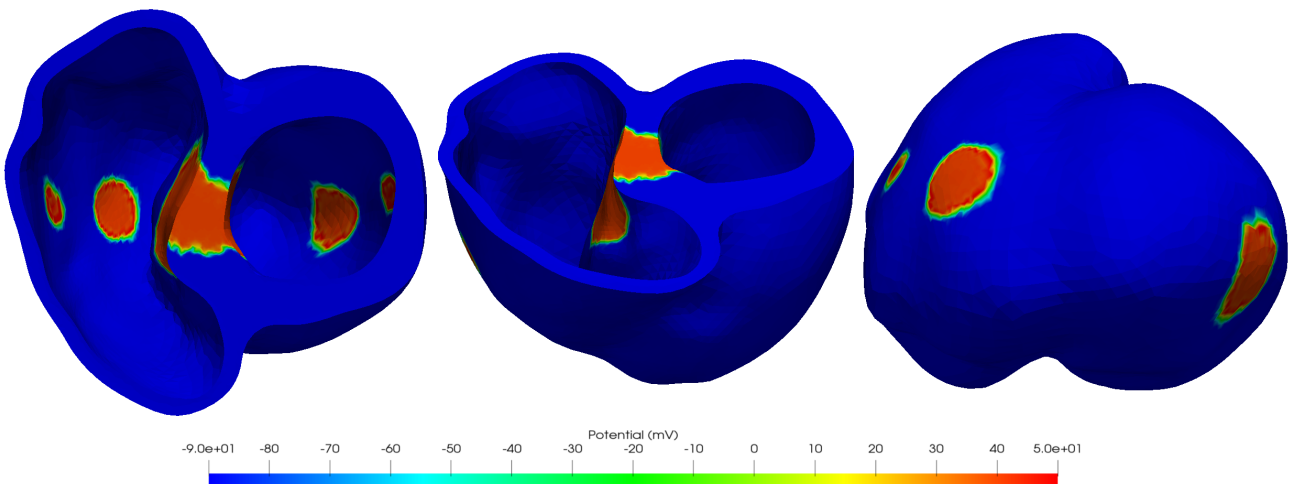Figure 6.8: Transmembrane potential in refined mesh at $t = 0.0064$.
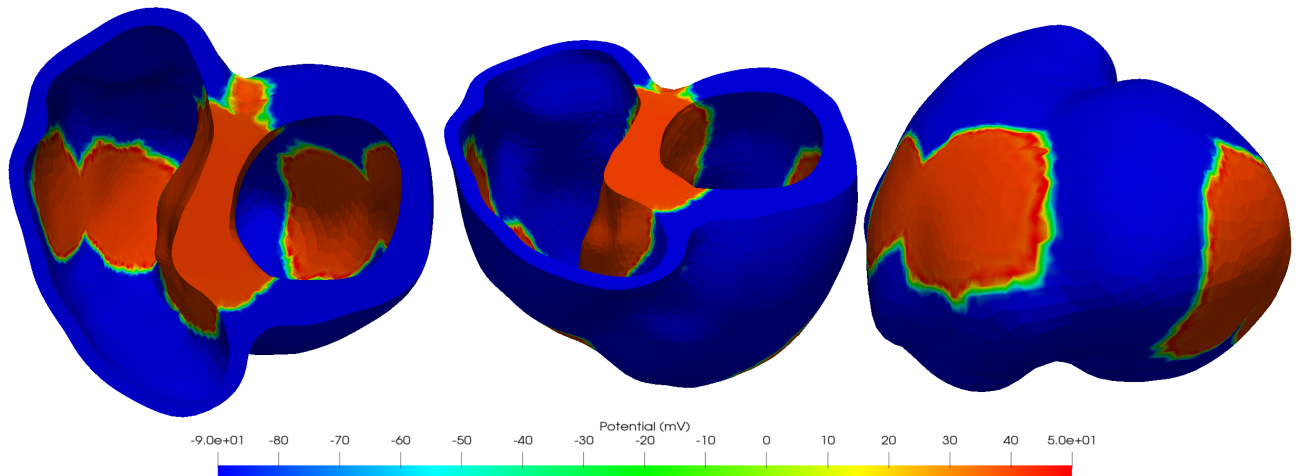
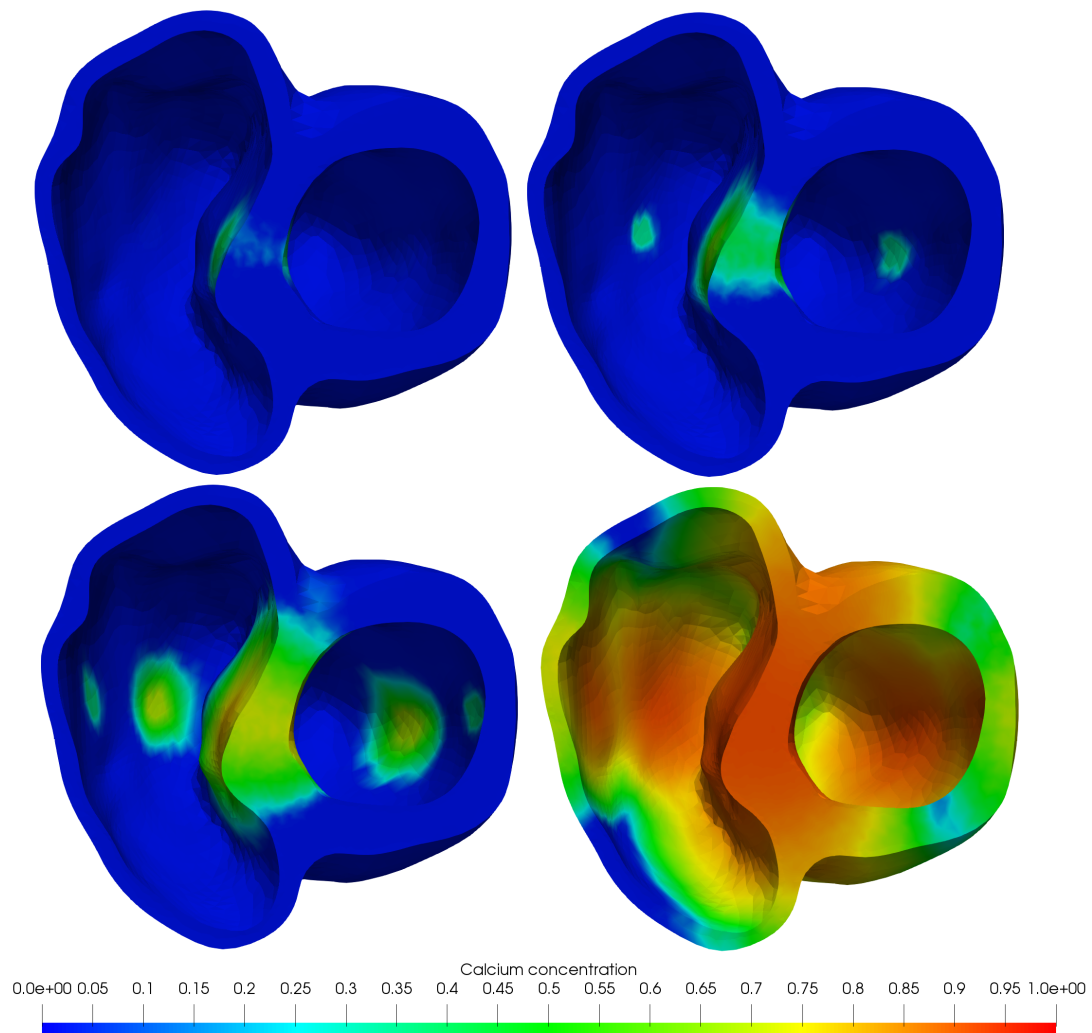Figure 6.9: Transmembrane potential in refined mesh at $t = 0.012$.

Figure 6.10: Ca^{2+} concentration in the cardiac tissue at different time steps. From left to right t=0.0029, t=0.00425, t=0.0069, t=0.015.

σ_t	σ_l	λ_{epi}	λ_{endo}	$\bar{k}_{epi}$	$\bar{k}_{endo}$	$\bar{k}'$	α	c_0	$\widehat{\mu}_A^1$	$\widehat{\mu}_A^2$	$\widehat{\mu}_A^3$	$\widehat{\mu}_A^4$	ρ
17.61	120.4	0.8	0.5	0.75	1.0	-7.0	-4.5	0.05	2.1	7.0	12	500	10^{-3}

$K_\perp^{epi,LV}$	$K_\perp^{epi,RV}$	$K_\perp^{base}$	$K_\parallel^{epi,LV}$	$K_\parallel^{epi,RV}$	$K_\parallel^{base}$	$C_\perp^{epi,LV}$	$C_\perp^{epi,RV}$	$C_\perp^{base}$	$C_\parallel^{epi,LV}$	$C_\parallel^{epi,RV}$	$C_\parallel^{base}$
12	15	1700	0	0	10^{-4}	5	5	1	0	0	0

B	$C_p^{LV,I}$	$C_p^{LV,II}$	$C_p^{RV,I}$	$C_p^{RV,II}$	C^{LV}	R^{LV}	C^{RV}	R^{RV}
100	-0.03	-0.08	-0.005	-0.015	3.0	0.035	5.0	0.015

Table 6.3: Parameters used in the electromechanical model: transversal and longitudinal conductivities ($\frac{mm^2}{s}$) in Eq. (3.1); transmurally heterogeneous wall thickening model parameters in Eq. (3.10); activation model coefficients α (μM^{-2}), c_0, and $\widehat{\mu}_A$ ($\mu M^2 \cdot s$) in the four cardiac phases in Eq. (3.9); density ρ ($\frac{g}{mm^3}$); Robin boundary condition coefficients ($\frac{kPa}{mm}$ and $\frac{kPa \cdot s}{mm}$) in Eqs. (3.4) - (3.6); bulk modulus B (kPa), relaxation parameter for the two isochoric phases C_p^I and C_p^{II} ($\frac{kPa}{mm^3}$) in Eq. (4.14); Windkessel model parameters C and R ($\frac{mm^3}{kPa}$ and $\frac{kPa \cdot s}{mm}$) in Eq. (4.16).

calcium in the cardiac tissue. We notice from Fig. 6.10 how the ion concentration and/or the fraction of open ionic channels on the cellular membrane changes accordingly to the transmembrane potential spreading along the myocardium.

6.3 Numerical results: mechanics

In this section we present the mechanical results coming from the problem (3.11) applied to our two geometries Figs. 5.2 and 5.3. We recall that we are solving the coupled electromechanical problem, here to better discuss and characterize the mechanics of the ventricles we show the mechanical results only. To obtain the following results we set the parameters in Table 6.3.

We will start exhibiting the displacement magnitude at different time-steps, making a comparison between the two settings. We will continue showing the fibres dynamics and how their orientation, together with the sheets, will strongly influence the mechanical behaviour of the complete geometry. Moreover, we will illustrate how the pressures and volumes change over time and we will display the pressure-volume (pV) loops for each case. Eventually, we will analyse how changing each parameter will affect the cardiac cycle.

From Figs. 6.11 to 6.22 we have the displacement magnitude of both mesh (a) and mesh (b) with the two fibres and sheets settings. We recall that these simulations are obtained keeping the same parameters of Table 6.3, the only differences are the geometry and the fibres and sheets orientation. In fact, we will discuss the results in the following:

- The displacement coming from the mesh (a) with setting 1 appears to be more physiological, the deformation is quite homogeneous along the geometry, the movement of the base is rigid and perpendicular to the centerline of each ventricle, both the sizes of the left and right ventricular base keep their initial shape, the thickening of the myocardium is rather uniform, the apexes move towards the base.
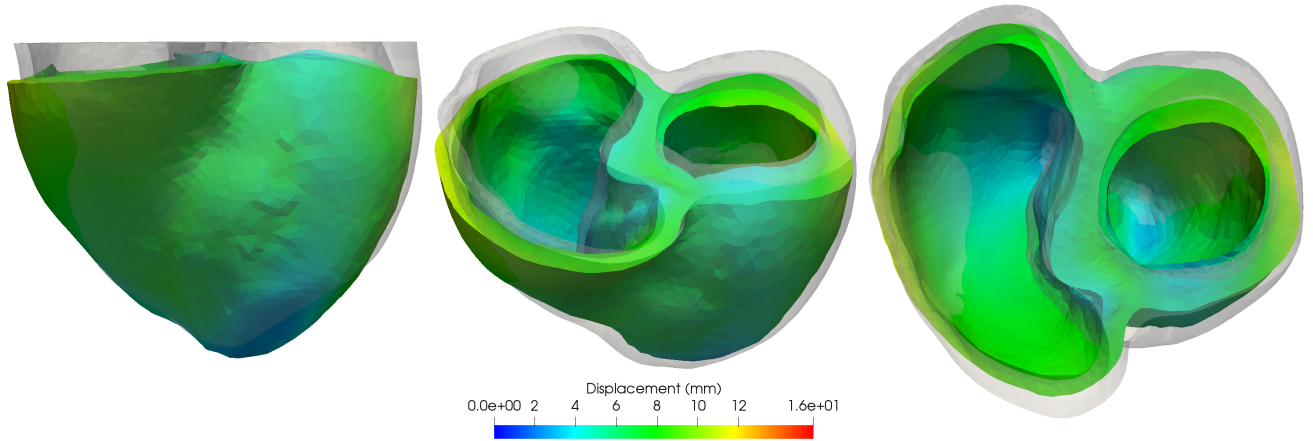
Figure 6.11: Myocardium displacement magnitude of mesh (a) with setting 1 at $t = 0.12$.

- The displacement coming from the mesh (a) with setting 2 appears to be heavily determined by the fibres' and sheets' directions. We have a considerable deformation of the base in a non-perpendicular direction, there are different regions distributed in the upper part of the geometry with a displacement longer than 16 mm, the size of the left ventricular base becomes more elliptical, loosing its original rounded shape, we have a non-homogeneous thickening of the myocardium, the apexes are barely moving.

- The displacement coming from the mesh (b) with setting 1 presents similar characteristics to the one obtained with the mesh (a) and the same setting. It is valuable to notice that the fact of having a thinner septum and a thicker left myocardial wall highlights the ability of the model [10] of reproducing the thickening of the myocardium.

- The displacement coming from the mesh (b) with setting 2 lets us better understand the influence of a thin septum in the mechanics. We can in fact observe that since in this case the septum is thinner than the one in the first geometry, it becomes less rigid and more prone to larger deformations.

In Figs. 6.23, 6.24, 6.25 and 6.26) we present the fibres dynamics of both mesh (a) and mesh (b) with different settings. Even though the fibres fields with setting 1 and 2 appear to be similar, at first glance, both at the endocardium and epicardium, we have to remember that looking at the transmural direction (see Figs. 5.7, 5.8, 5.9 and 5.10) we notice that with setting 1 the fibres are directed parallel to the base, with setting 2 perpendicular to it. This could explain the base deformation present in the simulations with the second setting.

Now we verify the ability to reproduce physiological pressure–volume (pV) loops for both the ventricles. We highlight the fact that our pV loops in Figs. 6.27 and 6.29 are in agreement with the medical measurements (see 2.6) both in the first isovolumic and in the ejection phase. Furthermore, the pressures and volumes evolution over time are in line with the ones presented in the Wiggers diagram 4.1. The maximum values of ventricular pressures are 120 mmHg for the left and around 30 mmHg for the right, as we depicted in 3.1. On the other hand, for the geometry (a) the endocardial volumes start
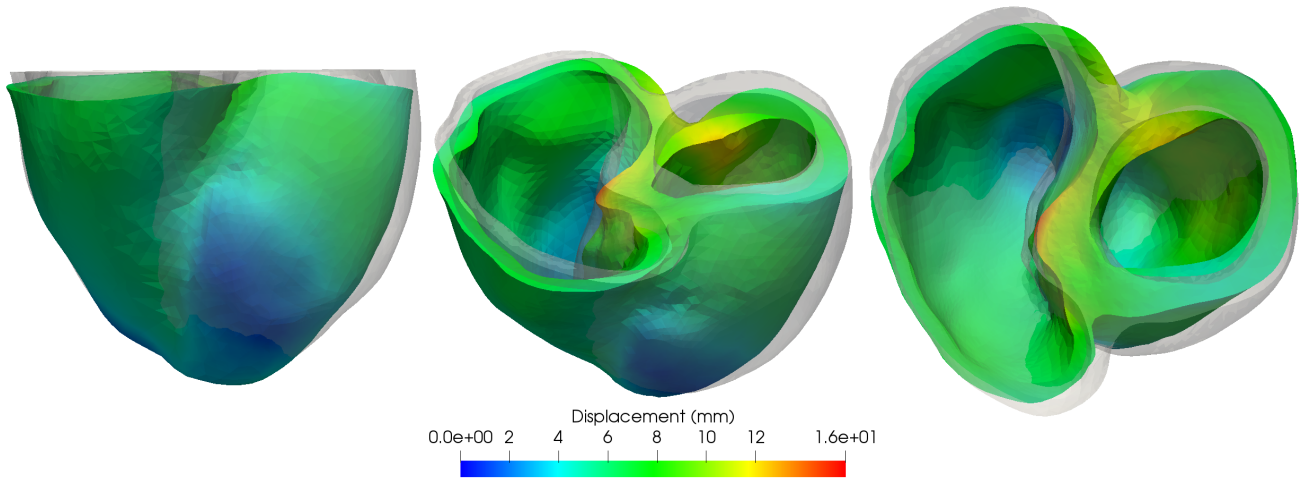
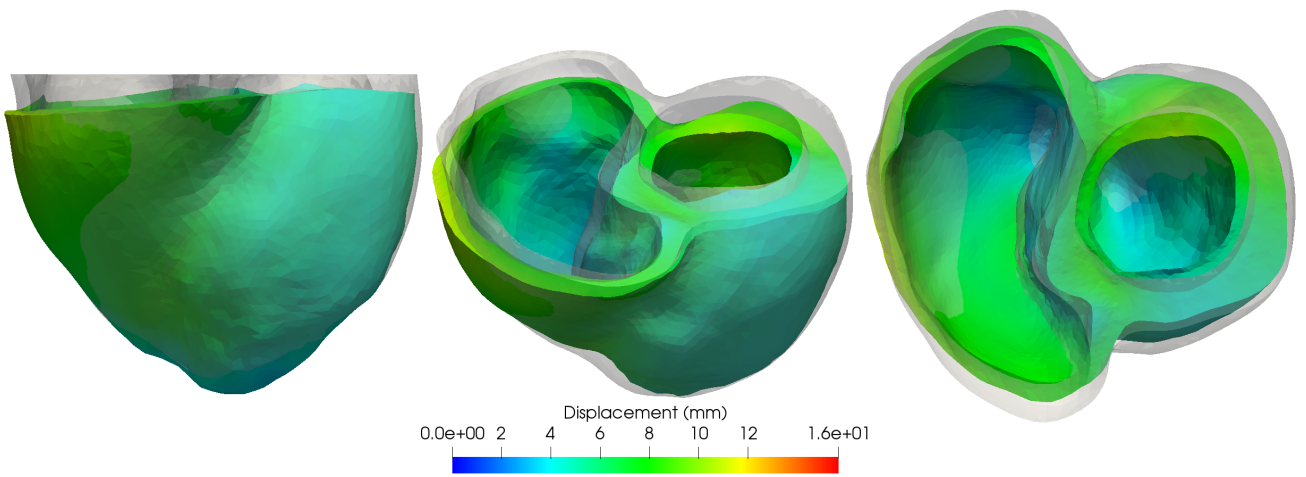Figure 6.12: Myocardium displacement magnitude of mesh (a) with setting 2 at $t = 0.12$.

Figure 6.13: Myocardium displacement magnitude of mesh (b) with setting 1 at $t = 0.12$.

Figure 6.14: Myocardium displacement magnitude of mesh (b) with setting 2 at $t = 0.12$.

Figure 6.15: Myocardium displacement magnitude of mesh (a) with setting 1 at $t = 0.17$.

Figure 6.16: Myocardium displacement magnitude of mesh (a) with setting 2 at $t = 0.17$.

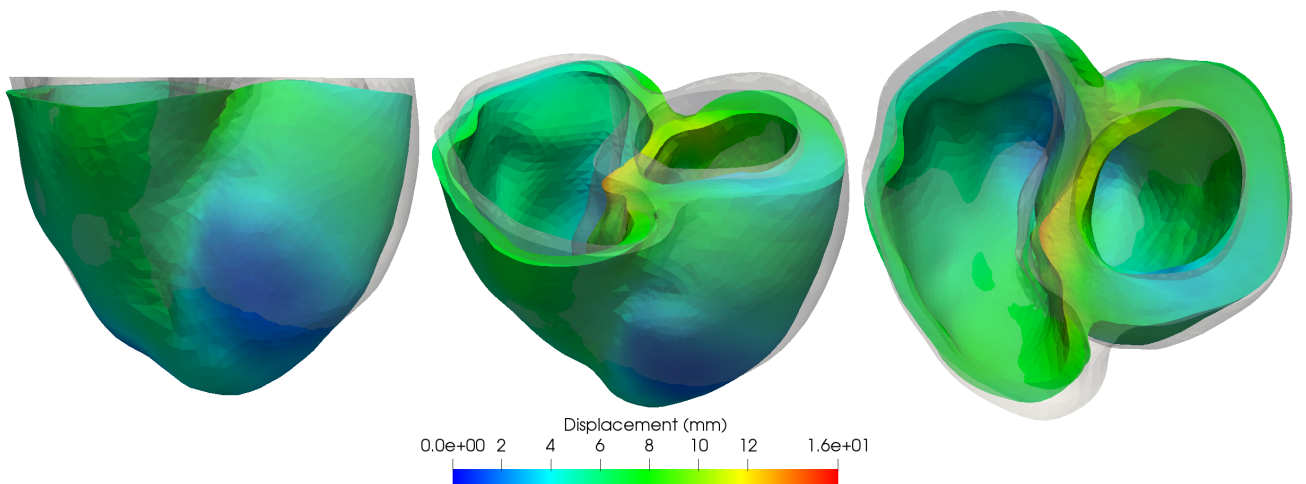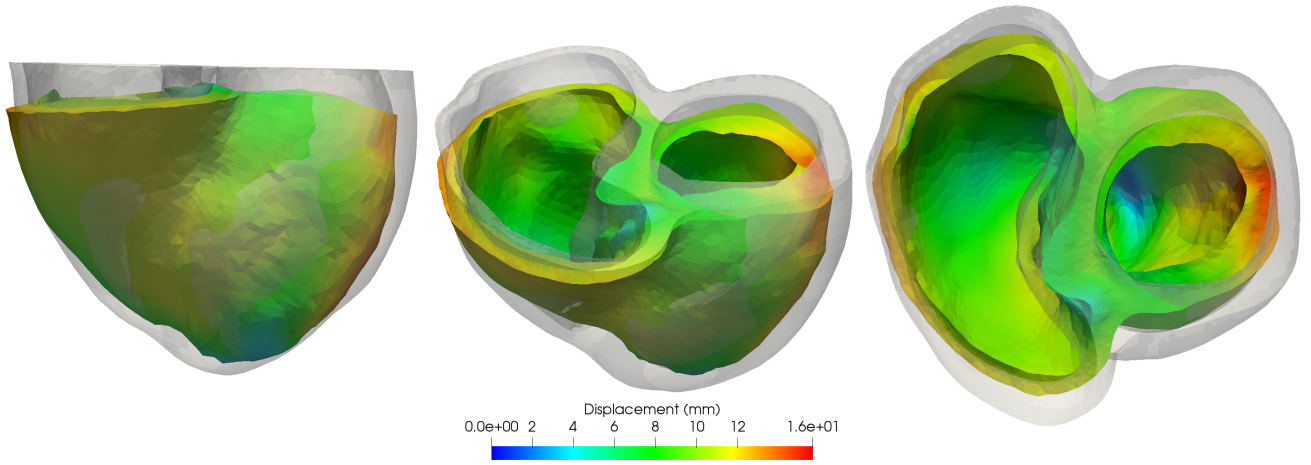Figure 6.17: Myocardium displacement magnitude of mesh (b) with setting 1 at $t = 0.17$.

Figure 6.18: Myocardium displacement magnitude of mesh (b) with setting 2 at $t = 0.17$.

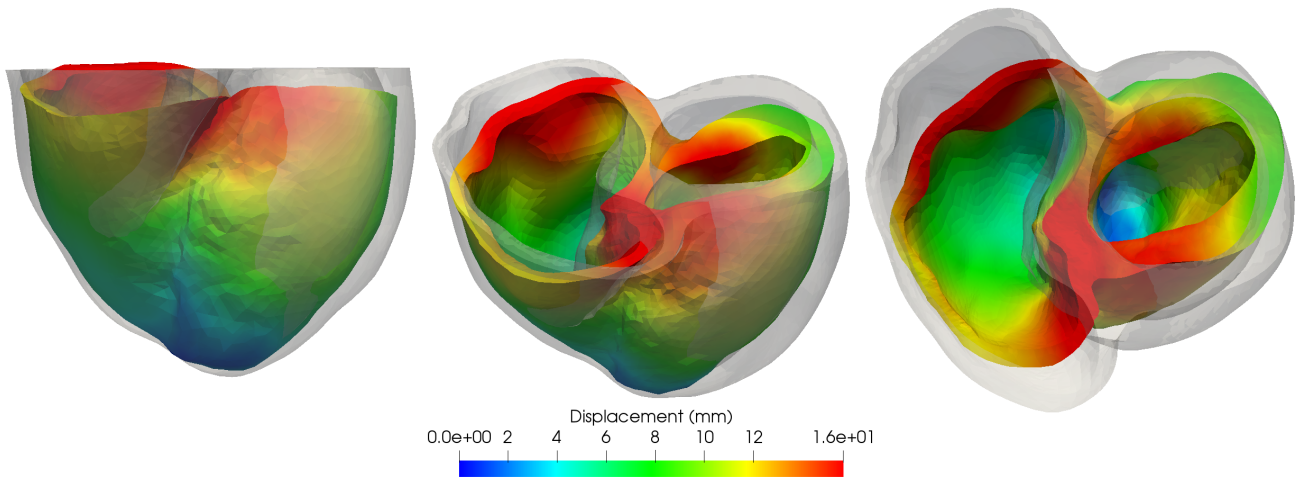Figure 6.19: Myocardium displacement magnitude of mesh (a) with setting 1 at $t = 0.20$.

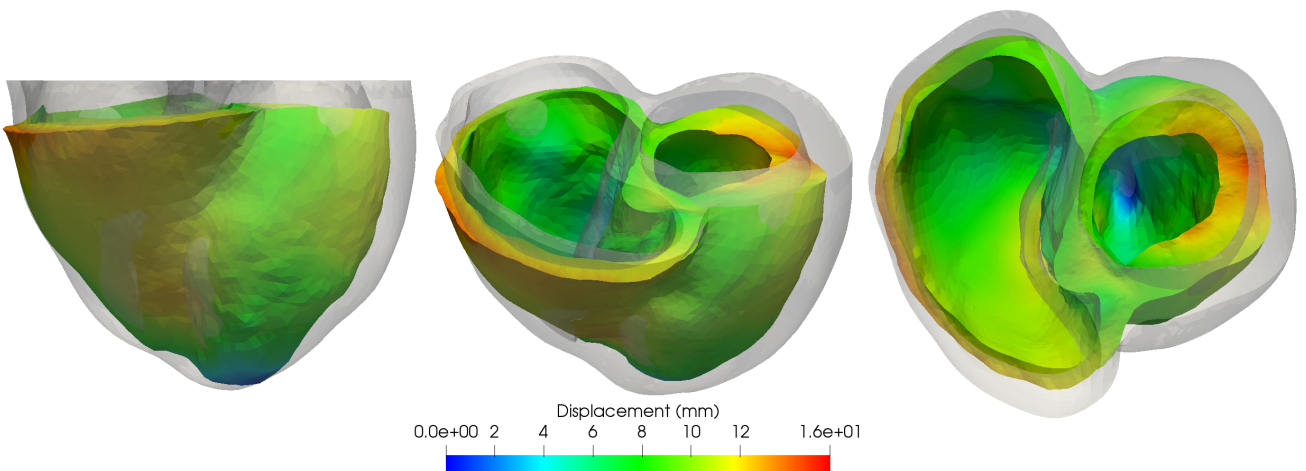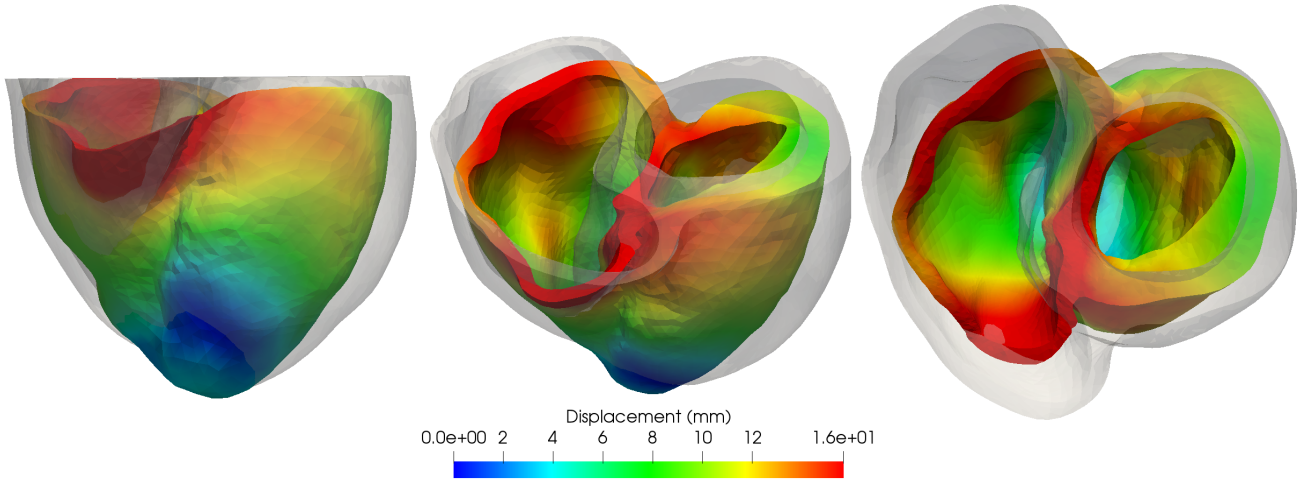Figure 6.20: Myocardium displacement magnitude of mesh (a) with setting 2 at $t = 0.20$.
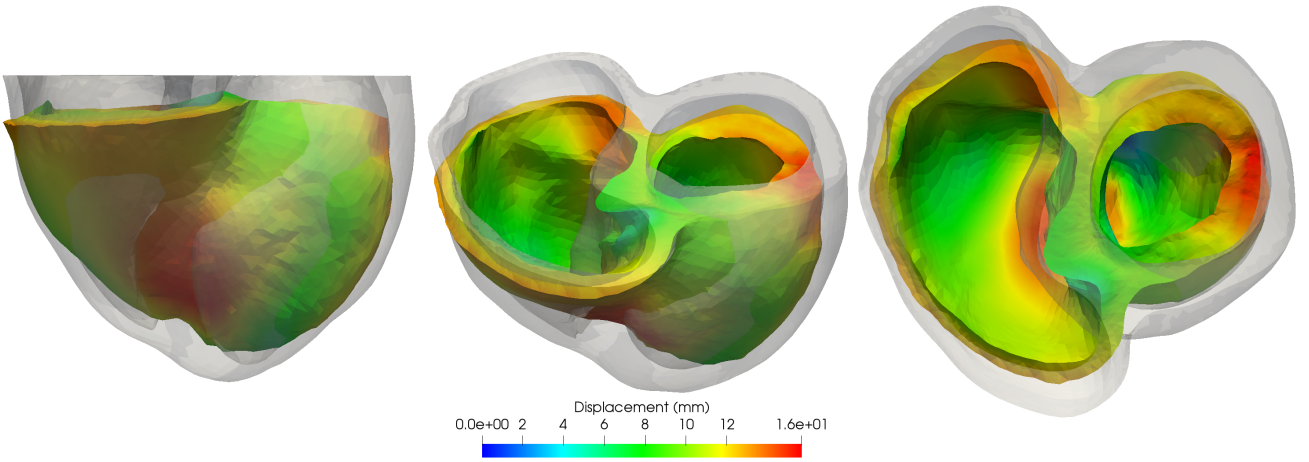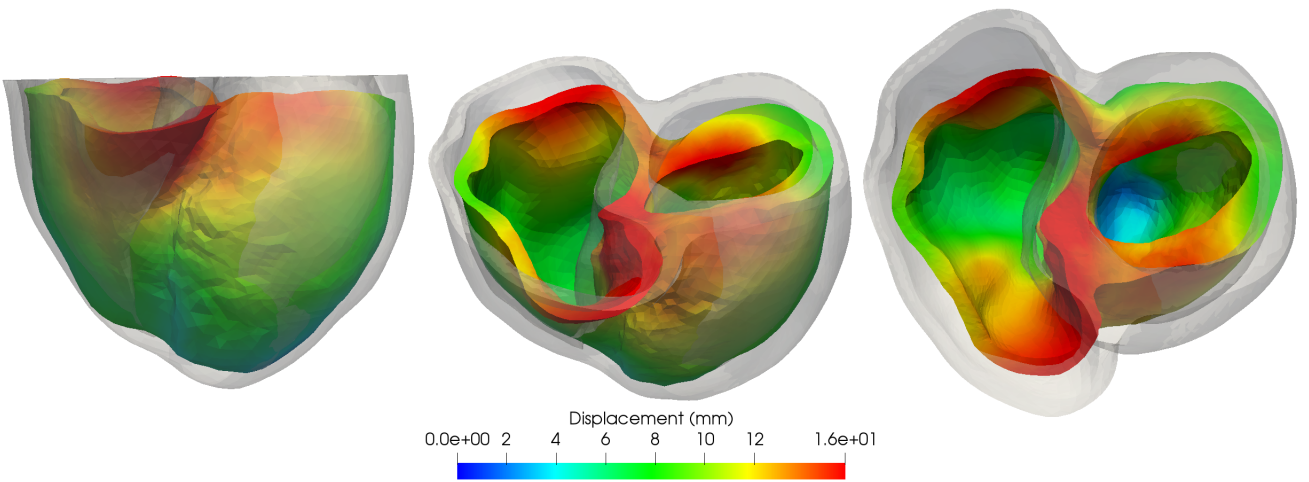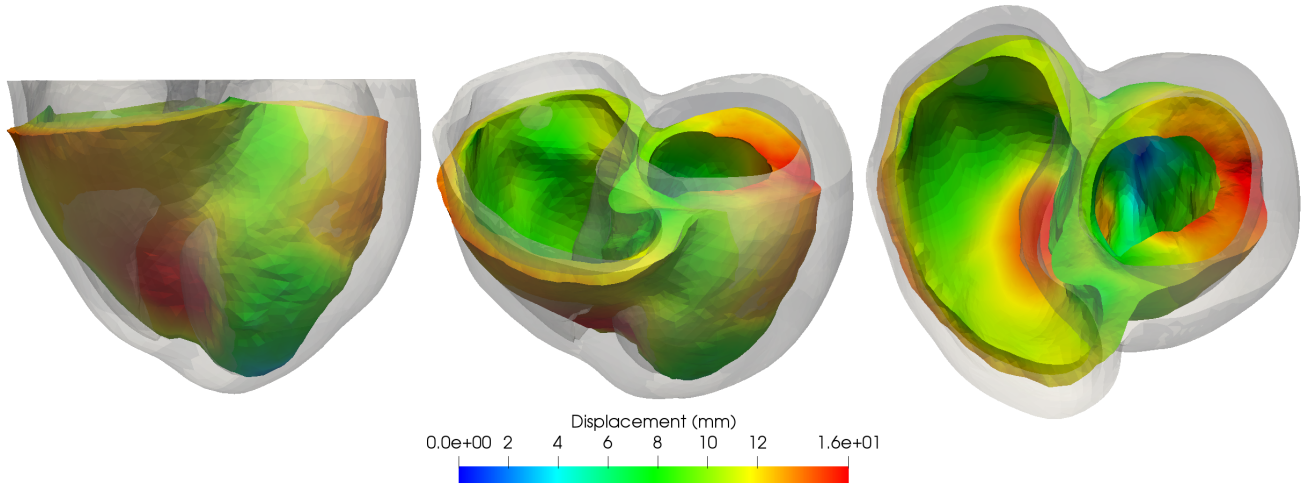
Figure 6.21: Myocardium displacement magnitude of mesh (b) with setting 1 at $t = 0.20$.
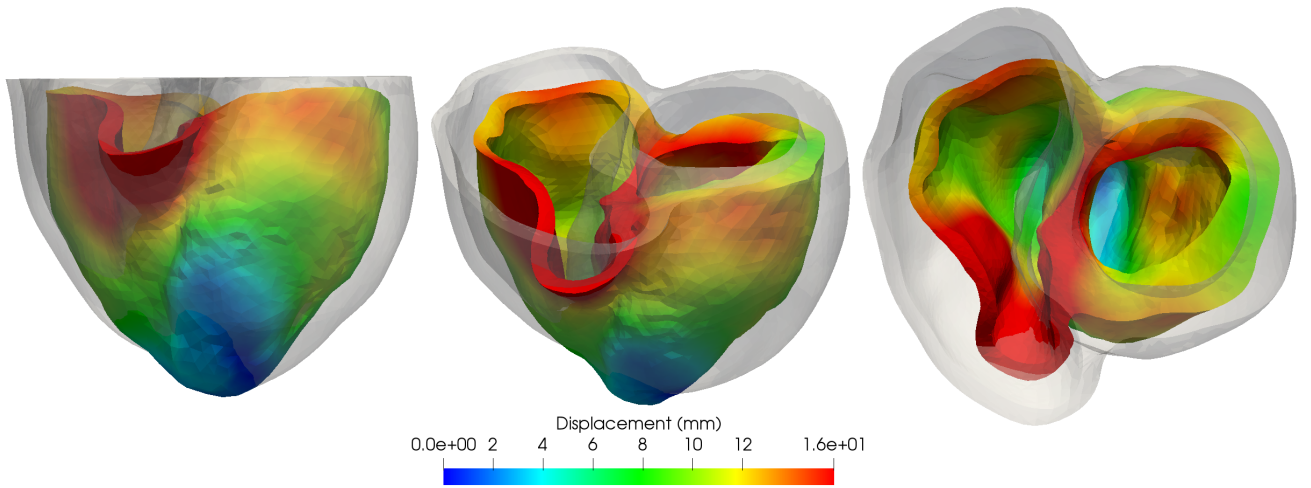
Figure 6.22: Myocardium displacement magnitude of mesh (b) with setting 2 at $t = 0.20$.

from 133 ml (LV) and 125 ml (RV), contracting until the values of 67 ml (LV) and 76 ml (RV). For the geometry (b) the endocardial volumes start from 133 ml (LV) and 125 ml (RV), contracting until the values of 58 ml (LV) and 75 ml (RV). We can then compute the stroke volume (SV), which is the value obtained by subtracting end-systolic volume (ESV) from end-diastolic volume (EDV) for a given ventricle:

$$SV = EDV - ESV$$

Therefore we have, for the mesh (a), a SV = 66 ml for the left ventricle and a SV = 49 ml for the right. For the mesh (b) we have a SV = 75 ml for the left ventricle and a SV = 50 ml for the right. Comparing these results with the ones presented in [65, 66], which are SV = 94 ml ($\pm$15 ml) for the right ventricle and SV = 95 ml ($\pm$14 ml) for the left ventricle in healthy 70-kg man, we can conclude that in our simulations both ventricles are contracting less than the usual ones, this behaviour happens with both our geometries. The myocardium volume ranges between 143 ml and 215 ml in mesh (a), between 133 ml and 215 ml in mesh (b). In contrast, the pV loops resulting from the simulation with the

setting 2 (see Fig. 6.28) confirm that the different fibres and sheets orientations lead to a distinct response in the cardiac phases.

In Table 6.4 we report the average number of Newton iterations to solve (4.8), the average number of subiterations for the first isochoric phase, the average number of GM-RES iterations and the average time spent for both the resolution of the linear system and to run the simulation. The results show that with both geometries the setting 2 require more computational efforts to be solved (T^{tot}), and in particular each problem needs in average more time/iterations.

We conclude this section by explaining which is the behaviour of the simulation if we change the most representative parameters used in the electromechanical model (see Table 6.3). This is done modifying the value of one parameter meanwhile keeping all the others fixed. We proceed in this way to try to isolate the influence of each single parameter.

- α and $\widehat{\mu}_A$: introduced in the activation model in (3.9), they control the contraction of the myocardium, triggered by the calcium concentration. The value of $\widehat{\mu}_A$ changes depending on the phase of the cardiac cycle (see Table 6.3). Instead, the value of α is fixed during all the simulation;

- Robin boundary condition coefficients: introduced in (3.4), they play a role in simulating the interaction with the pericardium. If we increase their value we have registered a stiffer behaviour, if we decrease it we have a geometry more inclined to deformations. We can notice that in our case the coefficient $K_\perp^{epi,RV}$ is bigger than $K_\perp^{epi,LV}$;

- B: introduced in (3.6), larger is the bulk modulus, the "stronger" is the enforcement of the incompressibility constraint. We have to highlight that, as suggested in the work [79], the choice of this together with the Robin boundary condition coefficients is responsible of the rotation of the ventricles;

- Windkessel parameters (R, C): introduced in (4.16), as these coefficients are involved only in the ejection phases, they influence the pressure and volume evolution. R is responsible of the maximal value of the pressure in the systolic phase (larger is the coefficient, the higher is the maximum), on the other hand C determines when this pick is reached.

Figure 6.23: Fibres dynamics of mesh (a) with setting 1. First column: $t = 0.12$; second column: $t = 0.17$; third column: $t = 0.20$.

Mesh	Setting	$\overline{N}^N$	$\overline{N}_I^{iso}$	$\overline{N}^G$	$\overline{T}^{sol}$	T^{tot}
(a)	1	3.22	2.03	31	0.6288	7h 42m
	2	3.43	2.22	43	0.7153	8h 21m
(b)	1	3.23	2.01	33	0.6578	7h 50m
	2	3.46	2.31	49	0.7346	8h 32m

Table 6.4: Computational setting, from left to right: average number of Newton iterations per timestep; average number of subiterations for the first isochoric phase; average number of GMRES iterations; average time spent (in seconds) for the resolution of the linear system; wall time for the simulation.
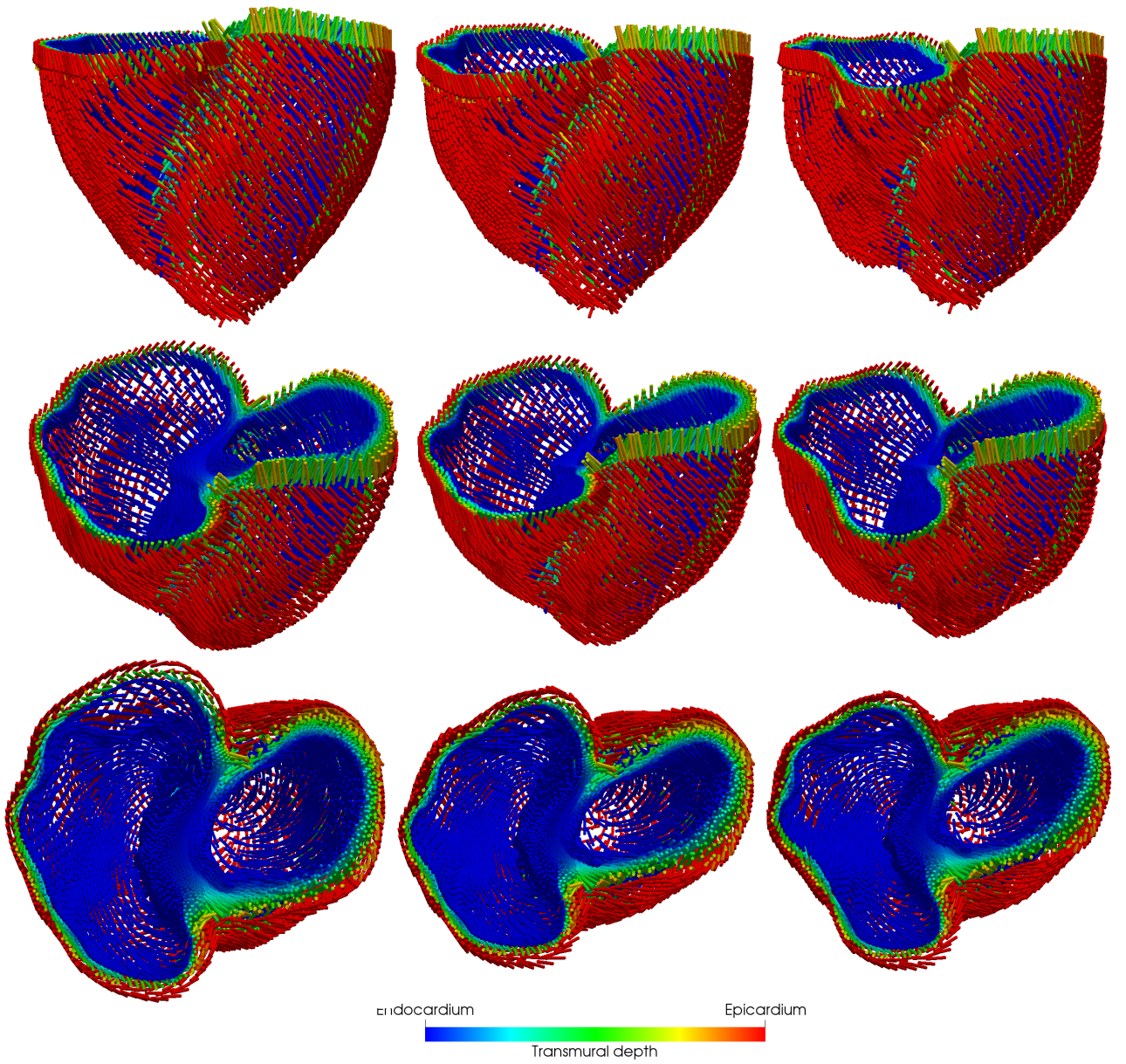
Figure 6.24: Fibres dynamics of mesh (a) with setting 2. First column: $t = 0.12$; second column: $t = 0.17$; third column: $t = 0.20$.
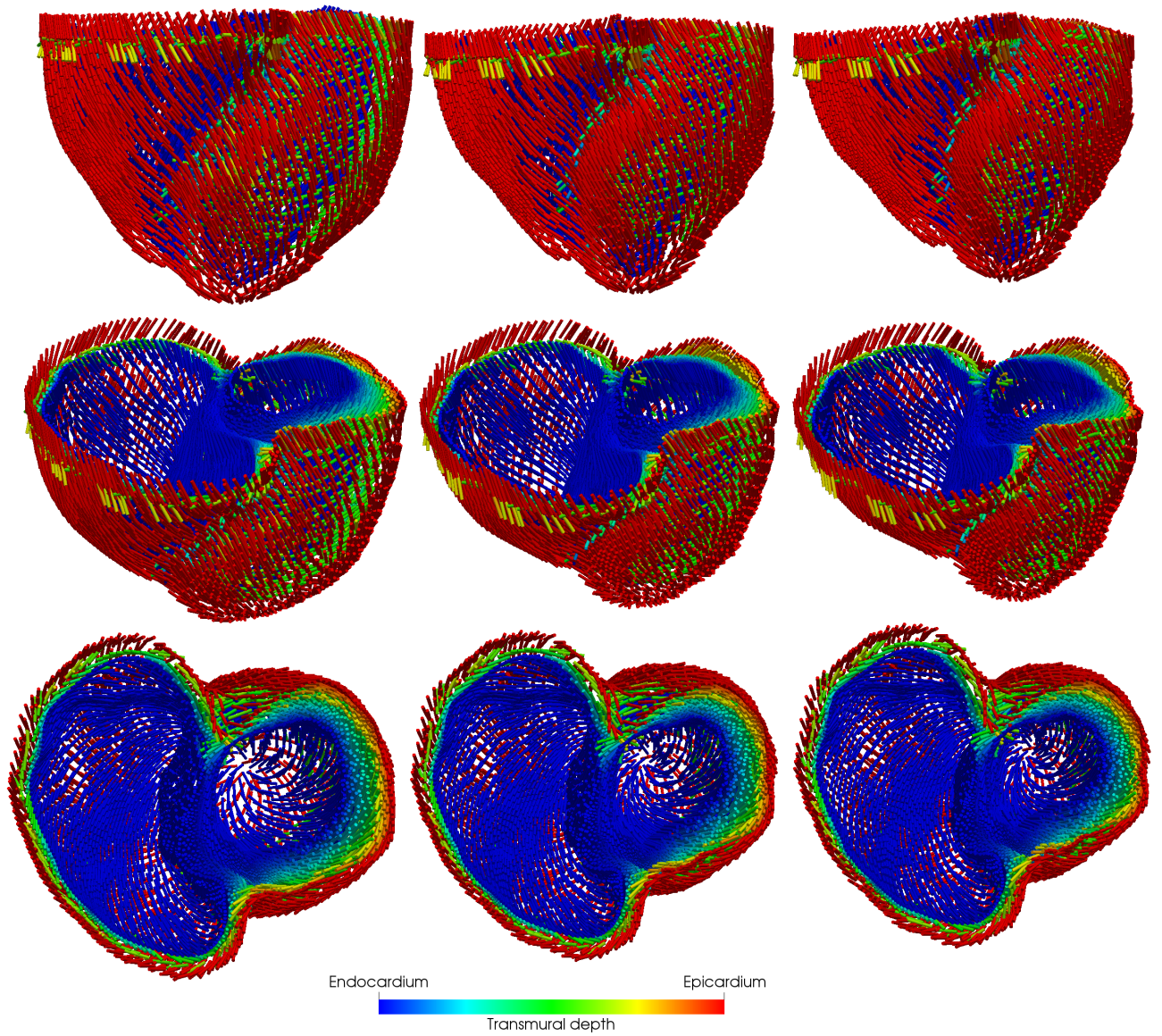
Figure 6.25: Fibres dynamics of mesh (b) with setting 1. First column: $t = 0.12$; second column: $t = 0.17$; third column: $t = 0.20$.
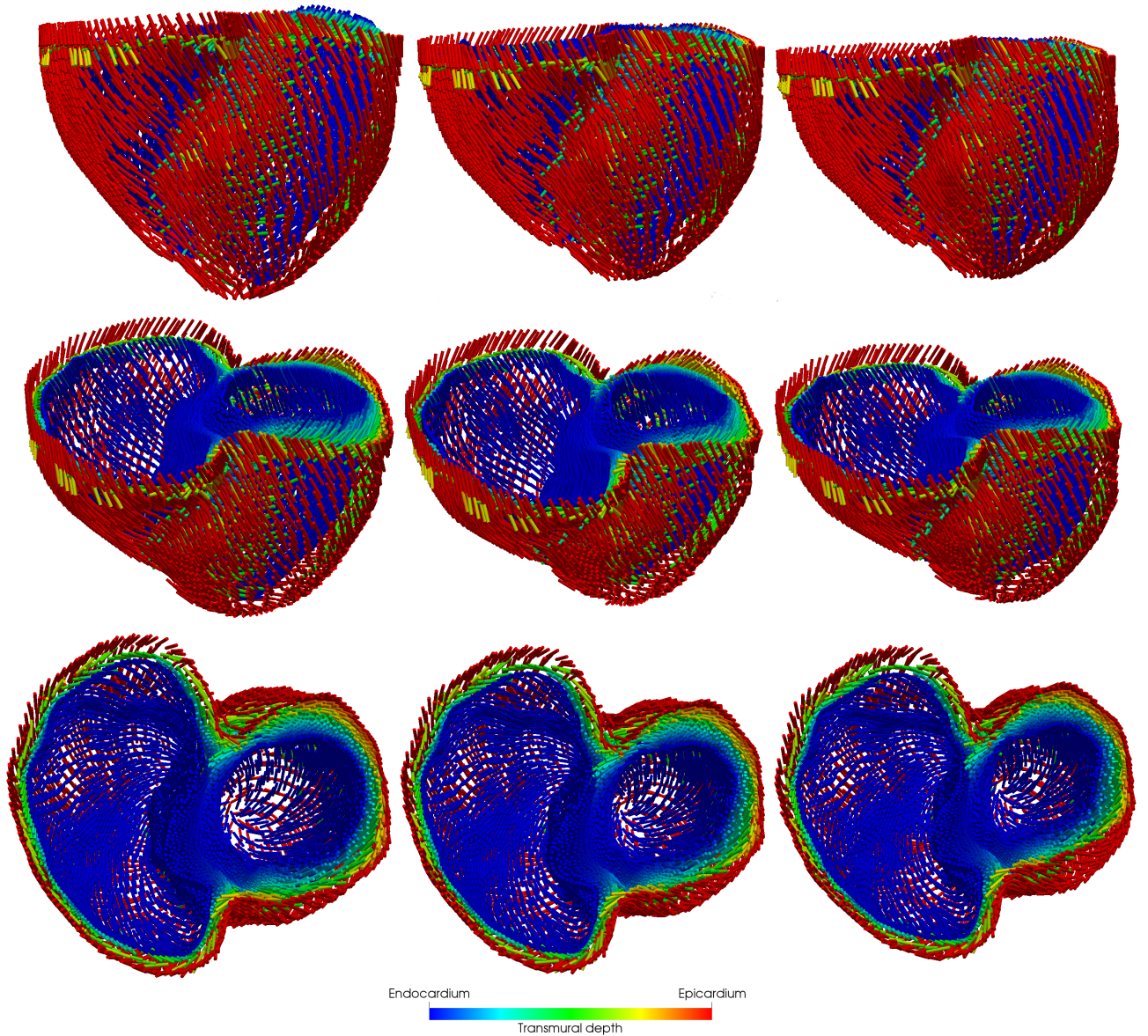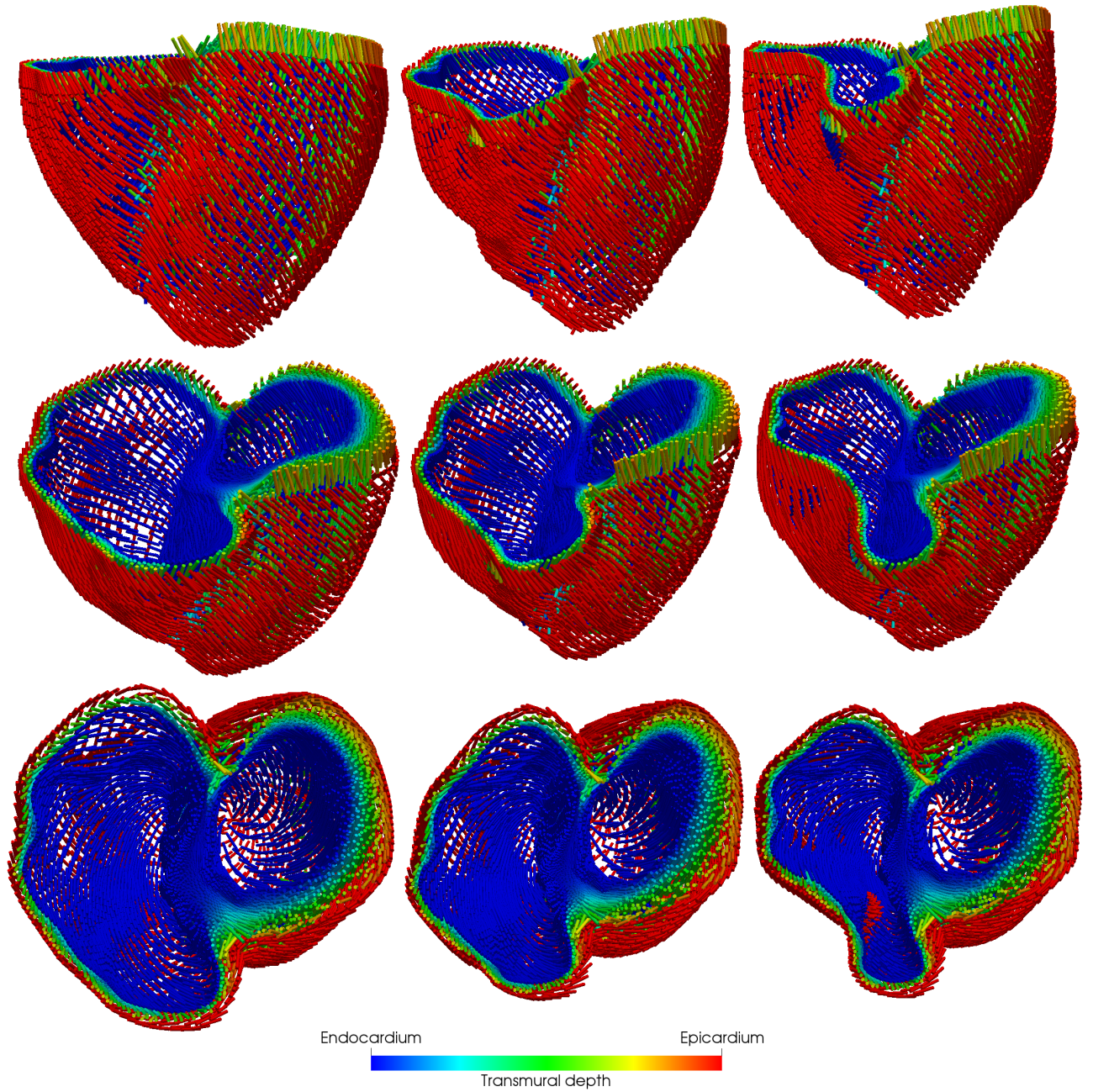
Figure 6.26: Fibres dynamics of mesh (b) with setting 2. First column: $t = 0.12$; second column: $t = 0.17$; third column: $t = 0.20$.
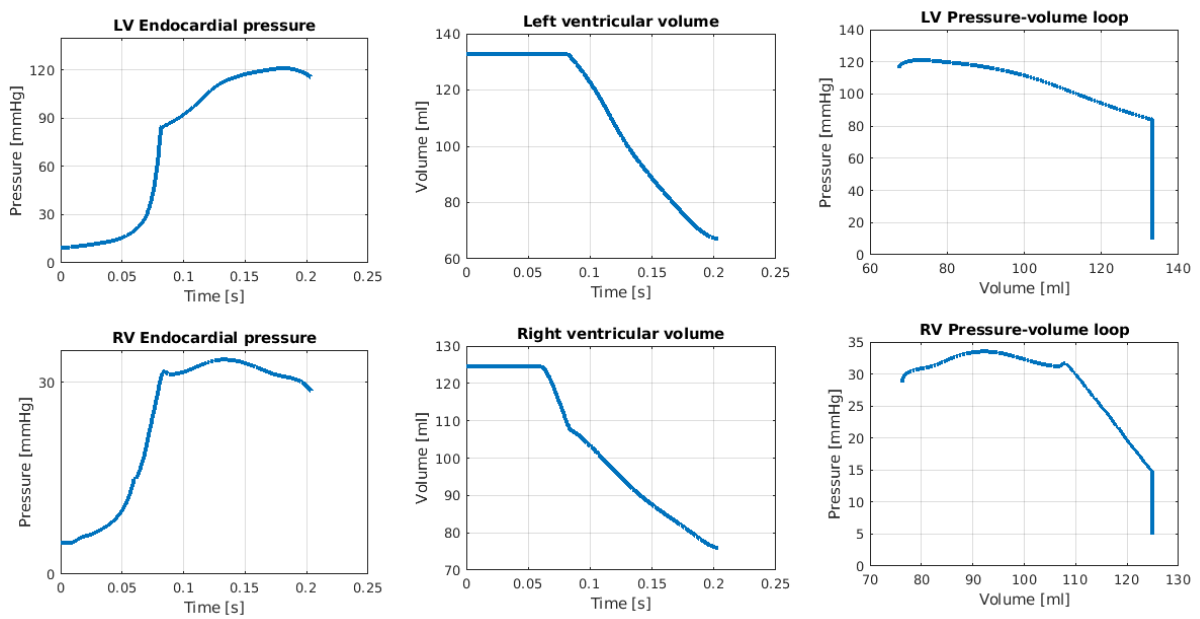
Figure 6.27: Evolution of pressures and volumes over time and pV loops for mesh (a) with setting 1.
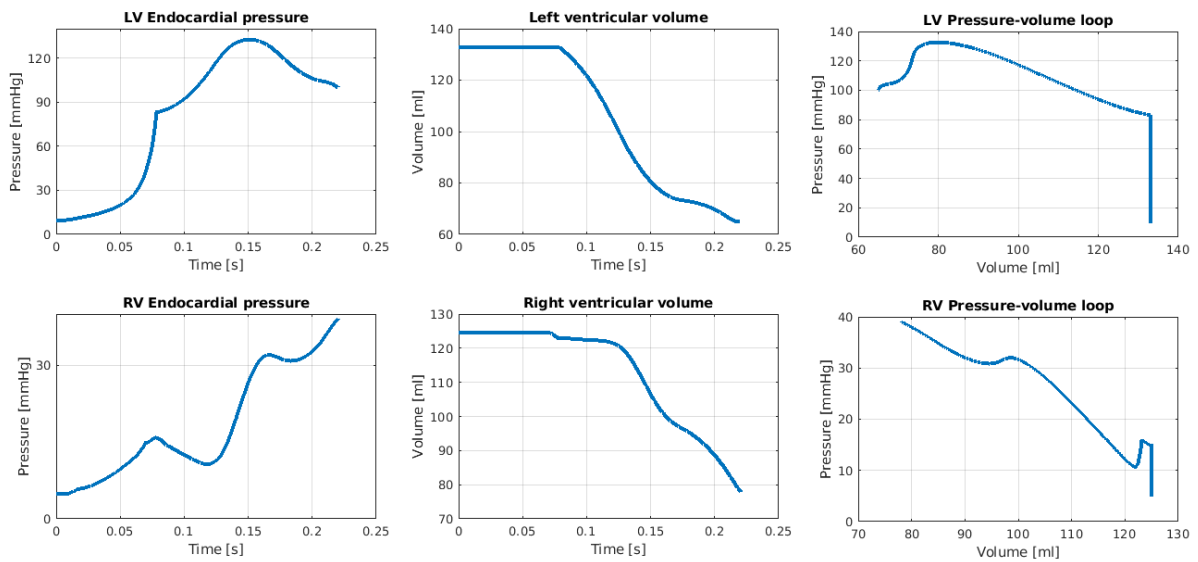
Figure 6.28: Evolution of pressures and volumes over time and pV loops for mesh (a) with setting 2.
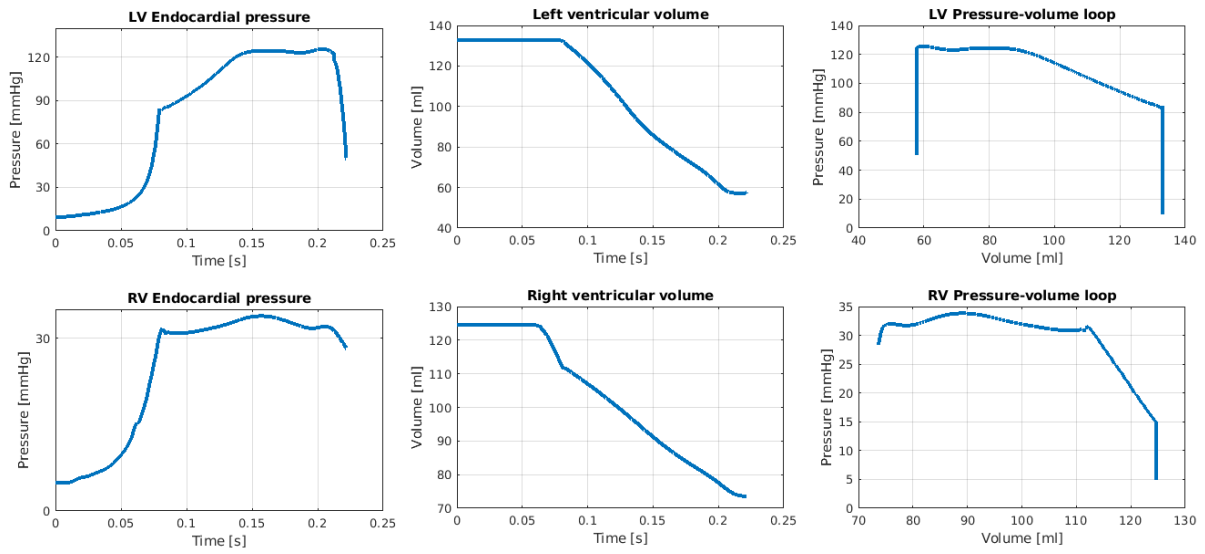
Figure 6.29: Evolution of pressures and volumes over time and pV loops for mesh (b) with setting 1.
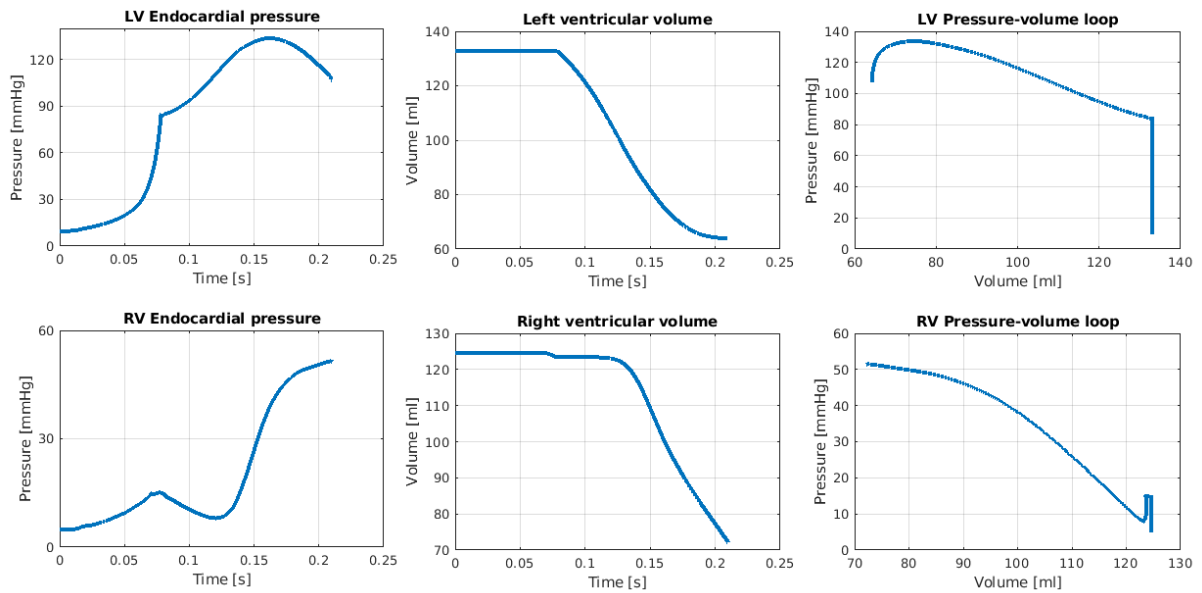
Figure 6.30: Evolution of pressures and volumes over time and pV loops for mesh (b) with setting 2.

7 Conclusions

In this work, we have proposed a mathematical and numerical modelling of the electromechanics of the human ventricles with the intention of addressing an accurate description of the systolic phases.

After a brief description of the quantitative as features of heart physiology we have first discussed the stand-alone mathematical models that are apt to represent the cardiac sub-systems: the propagation of the electrical transmembrane potential, the ionic current models for the action potential, the activation model for the fibres contraction, the model that describes the passive mechanical response of the cardiac tissue, a technique to take into account the fluid-structure interaction. This interaction of the myocardium with the blood inside the ventricular chambers was included in the description by prestressing the geometry and by solving additional 0D problems for the fluid. Integrating all these models together is essential to correctly describe the bi-ventricle functionality.

We address the coupled electromechanical problem in bi-ventricle geometries by means of a monolithic scheme, an extension of the work done in [38] for the left ventricle only. The global coupled system is tremendously challenging to be analysed mathematically and solved numerically.

After describing the mathematical models used to achieve our goal, we have carried on with the numerical discretization. We projected our infinite dimension models into suitable finite spaces in which we can apply ad hoc algorithms to obtain a discrete solution. We concluded this part with a characterization of the cardiac cycle highlighting the joint behaviour of the ventricles during a full heartbeat. Moreover, we showed the evolution of the pressures and volumes through the, so called, Wiggers diagram, useful to validate our models and simulations.

Before proceeding with the numerical results, we explained the essential part of patient–specific mesh generation, starting from a complete human heart, up to the ventricular geometry adopted for our work. After having a suitable mesh, we exploited the Laplace-Dirichlet Rule-Based algorithm to perform the fibres and sheets vector fields.

Finally, we have spanned different numerical simulations with the aim of validating the suitability of the chosen models to address situations of clinical relevance. We can briefly summarise the obtained results here:

- the fibres and sheets configuration is an essential ingredient for the simulation of the electromechanics of the human ventricles. We have just shown how changing their orientation, keeping fixed all the other parameters, will produce a completely pressure and volume evolution. The RV endocardial pressure over time and the pV loops using the setting 2 have a non-physiological behaviour with both mesh (a) and (b). Moreover, we can conclude that the fibres and sheets orientations play a role in the rigidity of the structure, enlarging or preventing deformations. Thus a detailed study focused on the myocardial fibres distribution and its role in the electromechanical modelling of the bi-ventricle is needed;

- the difference in the thickness of the septum between the two geometries has a

strong influence in the displacement magnitude, since a thinner septum turns out to be less rigid and more inclined to large deformation;

• there is a lack of data concerning the right ventricle. Most of the experiments (e.g. pressure–volume measurements by conductance catheter [103]) have been made on the left ventricle since it is easier to proceed with in-vivo measurement without any consequence for the patient. This does not let us to make satisfactory comparison with medical data for the right ventricle;

We can suggest some of the straightforward developments to the model section, such as the asynchronous activation due to the Purkinje network, the difference between the left and right cardiac tissue structure, the cardiac perfusion and its coupling with coronary flow, the location of infarcted tissue in the myocardium to have pathological situations, the joint modelling with the atria, the heart-torso coupling to have a simulation of an ECG, a finer description of the fluid-dynamics happening in the ventricles, a research of more sophisticated models for the approximation of different phases of the cardiac cycle.

Furthermore, it will be important to have some improvement also from the numerical point of view: increase the polynomial degree of the FEM approximation, move from a monolithic algorithm to a staggered one, which means to use different temporal grids for the electrophysiology and the mechanics. Moreover this has a physical sense, since the two phenomena happen at distinct time scales, it is reasonable to use different time steps for their solution. This last method will considerably reduce the overall computational time.

The current and future directions in the computational modelling of the total heart functions are: high-speed parallel computing and high-defined imaging to speed up the computations in realistic and patient–specific heart geometries using highly-detailed physiological models, parameter estimation and "big data" analysis, uncertainty quantification, prevention of pathological situation.

When we will be able to improve the computational power, we will have the possibility to focus on personalization of models and real-time simulations. We will have a tool to assist doctors in the daily crucial decisions that they face with cardiopathic patients. It will be of extreme importance a development of an accurate mathematical simulator that could provide cardiologists and cardio-surgeons with powerful, reliable and non-invasive investigations, which can potentially improve both the therapeutic treatment phase and the surgical intervention phase, thus saving time, money, patients' examinations and significantly reducing the risk for failure.

Bibliography

[1] J. Ahrens, B. Geveci, and C. Law. *ParaView: An End-User Tool for Large Data Visualization, Visualization Handbook.* 2005.

[2] R.R. Aliev and A.V. Panfilov. A simple two-variable model of cardiac excitation. *Chaos, Solitons & Fractals*, 7(3):293–301, 1996.

[3] D. Ambrosi, G. Arioli, F. Nobile, and A. Quarteroni. Electromechanical coupling in cardiac dynamics: the active strain approach. *SIAM Journal on Applied Mathematics*, 71(2):605–621, 2011.

[4] D. Ambrosi and S. Pezzuto. Active stress vs. active strain in mechanobiology: constitutive issues. *Journal of Elasticity*, 107(2):199–212, 2012.

[5] H. J. Arevalo, F. Vadakkumpadan, E. Guallar, A. Jebb, P. Malamas, K. C. Wu, and N. A. Trayanova. Arrhythmia risk stratification of patients after myocardial infarction using personalized heart models. *Nature Communications*, 7, 2016.

[6] T. Arts, K. D. Costa, J. W. Covell, and A. D. McCulloch. Relating myocardial laminar architecture to shear strain and muscle fiber orientation. *American Journal of Physiology - Heart and Circulatory Physiology*, 280(5):H2222–H2229, 2001.

[7] C.M. Augustin, A. Neic, M. Liebmann, A.J. Prassl, S.A. Niederer, G. Haase, and G. Plank. Anatomically accurate high resolution modeling of human whole heart electromechanics: a strongly scalable algebraic multigrid solver method for nonlinear deformation. *Journal of Computational Physics*, 305:622–646, 2016.

[8] B. Baillargeon, N. Rebelo, D.D. Fox, Robert L. Taylor, and E. Kuhl. The living heart project: a robust and integrative simulator for human heart function. *European Journal of Mechanics-A/Solids*, 48:38–47, 2014.

[9] L. Barbarotta. A mathematical and numerical study of the left ventricular contraction based on the reconstruction of a patient specific geometry. Master thesis, Politecnico di Milano, Italy, 2014.

[10] L. Barbarotta, S. Rossi, L. Dedè, and A. Quarteroni. A transmurally heterogeneous orthotropic activation model for ventricular contraction and its numerical validation. *MOX report*, (62), 2017.

[11] J. Bayer, R. Blake, G. Plank, and N. Trayanova. A novel rule-based algorithm for assigning myocardial fiber orientation to computational heart models. *Annals of biomedical engineering*, 40:2243–54, 05 2012.

[12] M. Bendahmane, R. Bürger, and R. Ruiz-Baier. A finite volume scheme for cardiac propagation in media with isotropic conductivities. *Mathematics and Computers in Simulation*, 80(9):1821–1840, 2010.

[13] M. J. Bishop, G. Plank, R. A. B. Burton, J. E. Schneider, D. J. Gavaghan, V. Grau, and P. Kohl. Development of an anatomically detailed mri-derived rabbit ventricular model and assessment of its impact on simulations of electrophysiological function. *American Journal of Physiology - Heart and Circulatory Physiology*, 298(2):H699–H718, 2010.

[14] R. Bordas, V. Grau, R.A.B. Burton, P. Hales, J.E. Schneider, D. Gavaghan, P. Kohl, and B. Rodriguez. Integrated approach for the study of anatomical variability in the cardiac purkinje system: from high resolution mri to electrophysiology simulation. In *Engineering in Medicine and Biology Society (EMBC), 2010 Annual International Conference of the IEEE*, pages 6793–6796. IEEE, 2010.

[15] W. Boron and E. Boulpaep. *Medical Physiology*, volume 2. Saunders, 2002.

[16] P.H.M. Bovendeerd, T. Arts, J.M. Huyghe, D.H. van Campen, and R.S. Reneman. Dependence of local left ventricular wall mechanics on myocardial fiber orientation: A model study. *Journal of Biomechanics*, 25(10):1129 – 1140, 1992.

[17] J. I. Brenner, K. R. Baker, and M. A. Berman. Prediction of left ventricular pressure in infants with aortic stenosis. *Heart*, 44(4):406–410, 1980.

[18] W.L. Briggs, V.E. Henson, and S.F. McCormick. *A Multigrid Tutorial*. SIAM, 2000.

[19] A. Bueno-Orovio, E.M. Cherry, and F.H. Fenton. Minimal model for human ventricular action potentials in tissue. *Journal of Theoretical Biology*, 253(3):544–560, 2008.

[20] E. Burman and A. Ern. The discrete maximum principle for stabilized finite element methods. In *Numerical Mathematics and Advanced Applications*, pages 557–566. Springer, 2003.

[21] P. Causin, J.F. Gerbeau, and F. Nobile. Added-mass effect in the design of partitioned algorithms for fluid–structure problems. *Computer Methods in Applied Mechanics and Engineering*, 194(42):4506–4527, 2005.

[22] R. Chabiniok, V.Y. Wang, M. Hadjicharalambous, L. Asner, J. Lee, M. Sermesant, E. Kuhl, A.A. Young, P. Moireau, M.P. Nash, et al. Multiphysics and multiscale modelling, data–model fusion and integration of organ physiology in the clinic: ventricular cardiac mechanics. *Interface Focus*, 6(2):15–83, 2016.

[23] D. Chapelle, M. Fernández, J.F. Gerbeau, P. Moireau, J. Sainte-Marie, and N. Zemzemi. Numerical simulation of the electromechanical activity of the heart. *Functional Imaging and Modeling of the Heart*, pages 357–365, 2009.

[24] A. Cheng, F. Langer, F. Rodriguez, J.C. Criscione, G.T. Daughters, D.C. Miller, and N.B. Ingels. Transmural cardiac strains in the lateral wall of the ovine left ventricle. *American Journal of Physiology-Heart and Circulatory Physiology*, 288(4):H1546–H1556, 2005.

[25] P. Cignoni, M. Callieri, M. Corsini, M. Dellepiane, F. Ganovelli, and G. Ranzuglia. *MeshLab: an Open-Source Mesh Processing Tool.* The Eurographics Association, 2008.

[26] P. Colli Franzone, L. F. Pavarino, and G. Savaré. Computational electrocardiology: mathematical and numerical modeling. In *Complex Systems in Biomedicine*, pages 187–241. Springer, 2006.

[27] P. Colli Franzone, L.F. Pavarino, and S. Scacchi. *Mathematical Cardiac Electrophysiology*, volume 13. Springer, 2014.

[28] P. Coupé, J. V Manjón, V. Fonov, J. Pruessner, M. Robles, and D.L. Collins. Patch-based segmentation using expert priors: Application to hippocampus and ventricle segmentation. *NeuroImage*, 54(2):940–954, 2011.

[29] S. Doll and K. Schweizerhof. On the development of volumetric strain energy functions. *Journal of Applied Mechanics*, 67(1):17–21, 2000.

[30] M. Dupraz, S. Filippi, A. Gizzi, A. Quarteroni, and R. Ruiz-Baier. Finite element and finite volume-element simulation of pseudo-ecgs and cardiac alternans. *Mathematical Methods in the Applied Sciences*, 38(6):1046–1058, 2015.

[31] T.S.E. Eriksson, A.J. Prassl, G. Plank, and G.A. Holzapfel. Influence of myocardial fiber/sheet orientations on left ventricular mechanical contraction. *Mathematics and Mechanics of Solids*, 18(6):592–606, 2013.

[32] M. Fedele, E. Faggiano, L. Barbarotta, F. Cremonesi, L. Formaggia, and S. Perotto. Semi-automatic three-dimensional vessel segmentation using a connected component localization of the region-scalable fitting energy. In *Image and Signal Processing and Analysis (ISPA), 2015 9th International Symposium on*, pages 72–77. IEEE, 2015.

[33] M. Fedele, E. Faggiano, L. Dedè, and A. Quarteroni. A patient specific aortic valve model based on moving resistive immersed surfaces. *Biomech Model Mechanobiol*, 16(5):1779–1803, 2017.

[34] F. H. Fenton, E. M. Cherry, and L. Glass. Cardiac arrhythmia. *Scholarpedia*, 3(7):1665, 2008.

[35] L. Formaggia, A. Quarteroni, and A. Veneziani. *Cardiovascular Mathematics: Modeling and Simulation of the Circulatory System*, volume 1. Springer Science & Business Media, 2010.

[36] M.W. Gee, C.M. Siefert, J.J. Hu, R.S. Tuminaro, and M.G. Sala. ML 5.0 smoothed aggregation user's guide. Technical report, Technical Report SAND2006-2649, Sandia National Laboratories, 2006.

[37] L. Geerts, P. Bovendeerd, K. Nicolay, and T. Arts. Characterization of the normal cardiac myofiber field in goat measured with mr-diffusion tensor imaging. *American Journal of Physiology - Heart and Circulatory Physiology*, 283(1):H139–H145, 2002.

[38] A. Gerbi, L. Dedè, and A. Quarteroni. A monolithic algorithm for the simulation of cardiac electromechanics in the human left ventricle, technical report. *MOX report*, 51, 2017.

[39] C. Geuzaine and J.-F. Remacle. *Gmsh: a three-dimensional finite element mesh generator with built-in pre- and post-processing facilities*, volume 79. 2009.

[40] A. L. Goldberger, L. A. N. Amaral, L. Glass, J. M. Hausdorff, P. C. Ivanov, R. G. Mark, J. E. Mietus, G. B. Moody, C. Peng, and H. E. Stanley. Physiobank, physiotoolkit, and physionet. *Circulation*, 101(23):e215–e220, 2000.

[41] A.M. Gordon, A.F. Huxley, and F.J. Julian. The variation in isometric tension with sarcomere length in vertebrate muscle fibres. *The Journal of Physiology*, 184(1):170, 1966.

[42] J.M. Guccione, A.D. McCulloch, and L.K. Waldman. Passive material properties of intact ventricular myocardium determined from a cylindrical model. *Journal of Biomechanical Engineering*, 113(1):42–55, 1991.

[43] V. Gurev, T. Lee, J. Constantino, H. Arevalo, and Trayanova N. A. Models of cardiac electromechanics based on individual hearts imaging data: Image-based electromechanical models of the heart. *Biomechanics and Modeling in Mechanobiology*, 10(3):295–306, 2011.

[44] S. Göktepe and E. Kuhl. Electromechanics of the heart: a unified approach to the strongly coupled excitation–contraction problem. *Computational Mechanics*, 45(2-3):227–243, 2010.

[45] R.M. Haralick and L.G. Shapiro. Image segmentation techniques. *Computer Vision, Graphics, and Image Processing*, 29(1):100–132, 1985.

[46] M.A. Heroux et al. An overview of the trilinos project. *ACM Transactions on Mathematical Software (TOMS)*, 31(3):397–423, 2005.

[47] A.L. Hodgkin and A.F. Huxley. A quantitative description of membrane current and its application to conduction and excitation in nerve. *The Journal of Physiology*, 117(4):500–544, 1952.

[48] G.A. Holzapfel and R.W. Ogden. Constitutive modelling of passive myocardium: a structurally based framework for material characterization. *Philosophical Transactions of the Royal Society of London A: Mathematical, Physical and Engineering Sciences*, 367(1902):3445–3475, 2009.

[49] C. Hoogendoorn, N. Duchateau, D. Sanchez-Quintana, T. Whitmarsh, F. M. Sukno, M. De Craene, K. Lekadir, and A. F. Frangi. A high-resolution atlas and statistical model of the human heart from multislice ct. *IEEE Transactions on Medical Imaging*, 32(1):28–44, Jan 2013.

[50] D. A. Hooks, M. L. Trew, B. J. Caldwell, G. B. Sands, I. J. LeGrice, and B. H. Smaill. Laminar arrangement of ventricular myocytes influences electrical behavior of the heart. *Circulation Research*, 101(10):e103–e112, 2007.

[51] M.C. Hsu and Y. Bazilevs. Blood vessel tissue prestress modeling for vascular fluid–structure interaction simulation. *Finite Elements in Analysis and Design*, 47(6):593–599, 2011.

[52] P.J. Hunter, M.P. Nash, and G.B. Sands. Computational electromechanics of the heart. *Computational Biology of the Heart*, 12:347–407, 1997.

[53] R. E. Idekerand, W. Kong, and S. Pogwizd. Purkinje fibers and arrhythmias. pacing and clinical electrophysiology. *Pacing Clin Electrophysiol.*, 32(3), 2009.

[54] I. Isgum, M. Staring, A. Rutten, M. Prokop, M.A. Viergever, and B. Van Ginneken. Multi–atlas–based segmentation with local decision fusion – application to cardiac and aortic segmentation in ct scans. *IEEE transactions on medical imaging*, 28(7):1000–1010, 2009.

[55] J.P Keener and J. Sneyd. Mathematica physiology - systems physiology. *Scholarpedia*, 2, 1998.

[56] D.E. Keyes, L.C. McInnes, C. Woodward, W. Gropp, E. Myra, M. Pernice, J. Bell, J. Brown, A. Clo, and J. Connors. Multiphysics simulations: Challenges and opportunities. *The International Journal of High Performance Computing Applications*, 27(1):4–83, 2013.

[57] S.B. Knisley, N. Trayanova, and F. Aguel. Roles of electric field and fiber structure in cardiac electric stimulation. *Biophysical Journal*, 77(3):1404–1417, 1999.

[58] S. Land, S.A. Niederer, and N.P. Smith. Efficient computational methods for strongly coupled cardiac electromechanics. *IEEE Transactions on Biomedical Engineering*, 59(5):1219–1228, 2012.

[59] E.H. Lee and D.T. Liu. Finite–strain elastic–plastic theory with application to plane–wave analysis. *Journal of Applied Physics*, 38(1):19–27, 1967.

[60] H.Y. Lee, N.C.F. Codella, M.D. Cham, Jonathan W. Weinsaft, and Y. Wang. Automatic left ventricle segmentation using iterative thresholding and an active contour model with adaptation on short-axis cardiac mri. *IEEE Transactions on Biomedical Engineering*, 57(4):905–913, 2010.

[61] I. J. LeGrice, B. H. Smaill, L. Z. Chai, S. G. Edgar, J. B. Gavin, and P. J. Hunter. Laminar structure of the heart: ventricular myocyte arrangement and connective tissue architecture in the dog. *American Journal of Physiology - Heart and Circulatory Physiology*, 269(2):H571–H582, 1995.

[62] C. Luo and Y. Rudy. A model of the ventricular cardiac action potential. Depolarization, repolarization, and their interaction. *Circulation Research*, 68(6):1501–1526, 1991.

[63] C. Luo and Y. Rudy. A dynamic model of the cardiac ventricular action potential. I. Simulations of ionic currents and concentration changes. *Circulation Research*, 74(6):1071–1096, 1994.

[64] Golob M., Moss RL., and Chesler N.C. Cardiac tissue structure, properties, and performance: A materials science perspective. *Annals of biomedical engineering*, 42(10):2003–2013, 2014.

[65] A. M. Maceira, S. K. Prasad, M. Khan, and D. J. Pennell. Normalized left ventricular systolic and diastolic function by steady state free precession cardiovascular magnetic resonance. *Journal of Cardiovascular Magnetic Resonance*, 8(3):417–426, 2006.

[66] A. M. Maceira, S. K. Prasad, M. Khan, and D. J. Pennell. Reference right ventricular systolic and diastolic function normalized to age, gender and body surface area from steady-state free precession cardiovascular magnetic resonance. *European Heart Journal*, 27(23):2879–2888, 2006.

[67] A. Melendo, A. Coll, M. Pasenau, E. Escolano, and A. Monros. www.gidhome.com, 2016. [Online; accessed Jun-2016].

[68] M. P. Nash and A. V. Panfilov. Electromechanical model of excitable tissue to study reentrant cardiac arrhythmias. *Progress in Biophysics and Molecular Biology*, 2:501–522, 2004.

[69] S. A. Niederer and N. P. Smith. An improved numerical method for strong coupling of excitation and contraction models in the heart. *Progress in Biophysics and Molecular Biology*, 96(1):90 – 111, 2008.

[70] S.A. Niederer et al. Verification of cardiac tissue electrophysiology simulators using an n-version benchmark. *Philosophical Transactions of the Royal Society A*, 369(1954):4331–4351, 2011.

[71] F. Nobile, A. Quarteroni, and R. Ruiz-Baier. An active strain electromechanical model for cardiac tissue. *International Journal for Numerical Methods in Biomedical Engineering*, 28(1):52–71, 2012.

[72] D. Noble. A modification of the hodgkin—huxley equations applicable to purkinje fibre action and pacemaker potentials. *The Journal of Physiology*, 160(2):317–352, 1962.

[73] R. W. Ogden. *Non-linear elastic deformations*. Courier Corporation, 1997.

[74] J.H. Omens, K.D. May, and A.D. McCulloch. Transmural distribution of three–dimensional strain in the isolated arrested canine left ventricle. *American Journal of Physiology–Heart and Circulatory Physiology*, 261(3):918–928, 1991.

[75] P. Pathmanathan, S.J. Chapman, D.J. Gavaghan, and J.P. Whiteley. Cardiac electromechanics: the effect of contraction model on the mathematical problem and accuracy of the numerical scheme. *The Quarterly Journal of Mechanics and Applied Mathematics*, 27(11):1751–1770, 2010.

[76] M. Pennacchio, G. Savaré, and P. Colli Franzone. Multiscale modeling for the bioelectric activity of the heart. *SIAM Journal on Mathematical Analysis*, 37(4):1333–1370, 2005.

[77] J. Peters, O. Ecabert, C. Meyer, H. Schramm, R. Kneser, A. Groth, and J. Weese. Automatic whole heart segmentation in static magnetic resonance image volumes. *Medical Image Computing and Computer-Assisted Intervention–MICCAI*, (1):402–410, 2007.

[78] S. Pezzuto. Mechanics of the heart: constitutive issues and numerical experiments. PhD thesis, Politecnico di Milano, Italy, 2013.

[79] S. Pezzuto and D. Ambrosi. Active contraction of the cardiac ventricle and distortion of the microstructural architecture. *International Journal for Numerical Methods in biomedical Engineering*, 30(12):1578–1596, 2014.

[80] M. Potse, B. Dubé, J. Richer, A. Vinet, and R.M. Gulrajani. A comparison of monodomain and bidomain reaction-diffusion models for action potential propagation in the human heart. *IEEE Transactions on Biomedical Engineering*, 53(12):2425–2435, 2006.

[81] A. Quarteroni. *Numerical Models for Differential Problems*, volume 2. 2014.

[82] A. Quarteroni, T. Lassila, S. Rossi, and R. Ruiz-Baier. Integrated heart - coupling multiscale and multiphysics models for the simulation of the cardiac function. *Computer Methods in Applied Mechanics and Engineering*, 314:345–407, 2017.

[83] A. Quarteroni, A. Manzoni, and C. Vergara. The cardiovascular system: Mathematical modelling, numerical algorithms and clinical applications. *Acta Numerica*, 26:365–590, 2017.

[84] A. Quarteroni, R. Sacco, and F. Saleri. *Numerical Mathematics*, volume 37. Springer Science & Business Media, 2010.

[85] A. Quarteroni, S. Sacco, and F. Saleri. *Numerical Mathematics*, volume 37. Springer-Verlag Berlin Heidelberg, 2007.

[86] A. N. Redington, H. H. Gray, M. E.Hodson, M. L. Rigby, and P. J. Oldershaw. Characterisation of the normal right ventricular pressure-volume relation by biplane angiography and simultaneous micromanometer pressure measurements. *Heart*, 59(1):23–30, 1988.

[87] F. Regazzoni, L. Dedè, and A. Quarteroni. Active contraction of cardiac cells: a model for sarcomere dynamics with cooperative interactions. *MOX report 48/2017*, 2017.

[88] J. Rijeken, P.H.M. Bovendeerd, A.J.G. Schoofs, D.H. van Campen, and T. Arts. Optimization of cardiac fiber orientation for homogeneous fiber strain at beginning of ejection.

[89] D. E. Roberts, L. T. Hersh, and A. M. Scher. Influence of cardiac fiber orientation on wavefront voltage, conduction velocity, and tissue resistivity in the dog. *Circulation Research*, 44(5):701–712, 1979.

[90] D. Romero, R. Sebastian, B.H. Bijnens, V. Zimmerman, P.M. Boyle, E.J. Vigmond, and A.F. Frangi. Effects of the Purkinje system and cardiac geometry on biventricular pacing: a model study. *Annals of Biomedical Engineering*, 38(4):1388–1398, 2010.

[91] S. Rossi. Anisotropic modeling of cardiac mechanical activation. PhD thesis, EPFL, Switzerland, 2014.

[92] S. Rossi, T. Lassila, R. Ruiz-Baier, A. Sequeira, and A. Quarteroni. Thermodynamically consistent orthotropic activation model capturing ventricular systolic wall thickening in cardiac electromechanics. *European Journal of Mechanics-A/Solids*, 48:129–142, 2014.

[93] S. Rossi, R. Ruiz-Baier, L.F. Pavarino, and A. Quarteroni. Orthotropic active strain models for the numerical simulation of cardiac biomechanics. *International Journal for Numerical Methods in Biomedical Engineering*, 28(6-7):761–788, 2012.

[94] R. Ruiz-Baier, A. Gizzi, S. Rossi, C. Cherubini, A. Laadhari, S. Filippi, and A. Quarteroni. Mathematical modelling of active contraction in isolated cardiomyocytes. *Mathematical Medicine and Biology*, 31(3):259–283, 2014.

[95] Y. Saad. *Iterative Methods for Sparse Linear Systems*. SIAM, 2003.

[96] J.E. Saffitz, H.L. Kanter, K.G. Green, T.K. Tolley, and E.C. Beyer. Tissue-specific determinants of anisotropic conduction velocity in canine atrial and ventricular myocardium. *Circulation Research*, 74(6):1065–1070, 1994.

[97] J. Sainte-Marie, D. Chapelle, R. Cimrman, and M. Sorine. Modeling and estimation of the cardiac electromechanical activity. *Computers & Structures*, 84(28):1743–1759, 2006.

[98] C. Sansour. On the physical assumptions underlying the volumetric-isochoric split and the case of anisotropy. *European Journal of Mechanics-A/Solids*, 27(1):28–39, 2008.

[99] P.P. Sengupta, J. Korinek, M. Belohlavek, J. Narula, M.A. Vannan, A. Jahangir, and B.K. Khandheria. Left ventricular structure and function. *Journal of the American College of Cardiology*, 48(10):1988–2001, 2006.

[100] F. Sheehan and A. Redington. The right ventricle: anatomy, physiology and clinical imaging. *Heart*, 94(11):1510–1515, 2008.

[101] J.C. Simo and R.L. Taylor. Quasi-incompressible finite elasticity in principal stretches. continuum basis and numerical algorithms. *Computer Methods in Applied Mechanics and Engineering*, 85(3):273–310, 1991.

[102] N.P. Smith, D.P. Nickerson, E.J. Crampin, and P.J. Hunter. Multiscale computational modelling of the heart. *Acta Numerica*, 13:371–431, 2004.

[103] P. Steendijk, S. A. F. Tulner, M. Wiemer, R. A. Bleasdale, J. J. Bax, E. E. Van Der Wall, J. Vogt, and M. J. Schalij. Pressure–volume measurements by conductance catheter during cardiac resynchronization therapy. *European Heart Journal Supplements*, 6:D35–D42, 2004.

[104] D. D. Streeter, H. M. Spotnitz, D. P. Patel, J. Ross, and E. H. Sonneblick. Fiber orientation in the canine left ventricle during diastole and systole. *Circulation Research*.

[105] D.D. Streeter, W.E. Powers, M.A. Ross, and F. Torrent-Guasp. Three dimensional fiber orientation in the mammalian left ventricular wall,. *Cardiovascular System Dynamics*, pages 73–84, 1978.

[106] D. Sung, R. W. Mills, J. Schettler, S. M. Narayan, J. H. Omens, and A. D. McCulloch. Ventricular filling slows epicardial conduction and increases action potential duration in an optical mapping study of the isolated rabbit heart. *Journal of Cardiovascular Electrophysiology*, 14(7):739–749, 2003.

[107] A. Tagliabue, L. Dedè, and A. Quarteroni. Complex blood flow patterns in an idealized left ventricle: a numerical study. *Chaos: An Interdisciplinary Journal of Nonlinear Science*, 27(9):093939, 2017.

[108] A. Tagliabue, L. Dedè, and A. Quarteroni. Fluid dynamics of an idealized left ventricle: the extended Nitsche's method for the treatment of heart valves as mixed time varying boundary conditions. *International Journal for Numerical Methods in Fluids*, 85(3):135–164, 2017.

[109] K. Takizawa, Y. Bazilevs, and T.E. Tezduyar. Space–time and ale-vms techniques for patient-specific cardiovascular fluid–structure interaction modeling. *Archives of Computational Methods in Engineering*, 19(2):171–225, 2012.

[110] K.H.W.J. Ten Tusscher, D. Noble, P.J. Noble, and A.V. Panfilov. A model for human ventricular tissue. *American Journal of Physiology-Heart and Circulatory Physiology*, 286(4):H1573–H1589, 2004.

[111] F. Torrent-Guasp, M. J. Kocica, A. F. Corno, M. Komeda, F. Carreras-Costa, A. Flotats, J. Cosin-Aguillar, and H. Wen. Towards new understanding of the heart structure and function. *European Journal of Cardio-thoracic Surgery*, 27(2):191–201, 2005.

[112] N.A. Trayanova. Whole-heart modeling applications to cardiac electrophysiology and electromechanics. *Circulation Research*, 108(1):113–128, 2011.

[113] N.A. Trayanova, J. Constantino, and V. Gurev. Models of stretch-activated ventricular arrhythmias. *Journal of Electrocardiology*, 43(6):479–485, 2010.

[114] C. Trentin, E. Faggiano, M. Conti, and F. Auricchio. An automatic tool for thoracic aorta segmentation and 3d geometric analysis. In *International Symposium on Image and Signal Processing and Analysis (ISPA)*, pages 60–65, 2015.

[115] T.P. Usyk, I.J. LeGrice, and A.D. McCulloch. Computational model of three-dimensional cardiac electromechanics. *Computing and Visualization in Science*, 4(4):249–257, 2002.

[116] F. Vadakkumpadan, H. Arevalo, C. Ceritoglu, M. Miller, and N. Trayanova. Image-based estimation of ventricular fiber orientations for personalized modeling of cardiac electrophysiology. *IEEE transactions on medical imaging*, 31(5):1051–1060, 2012.

[117] M. Vendelin, P. H. M. Bovendeerd, J. Engelbrecht, and T. Arts. Optimizing ventricular fibers: uniform strain or stress, but not atp consumption, leads to high efficiency. *American Journal of Physiology - Heart and Circulatory Physiology*, 283(3):H1072–H1081, 2002.

[118] C. Vergara, M. Lange, S. Palamara, T. Lassila, A.F. Frangi, and A. Quarteroni. A coupled 3D–1D numerical monodomain solver for cardiac electrical activation in the myocardium with detailed purkinje network. *Journal of Computational Physics*, 308:218–238, 2016.

[119] C. Vergara, S. Palamara, D. Catanzariti, F. Nobile, E. Faggiano, C. Pangrazzi, M. Centonze, M. Maines, A. Quarteroni, and G. Vergara. Patient-specific generation of the Purkinje network driven by clinicalm easurements of a normal propagation. *Medical and Biological Engineering and Computing*, 52(10):813, 2014.

[120] Frederick J. Vetter, Stephen B. Simons, Sergey Mironov, Christopher J. Hyatt, and Arkady M. Pertsov. Epicardial fiber organization in swine right ventricle and its impact on propagation. *Circulation Research*, 96(2):244–251, 2005.

[121] H. Watanabe, S. Sugiura, H. Kafuku, and T. Hisada. Multiphysics simulation of left ventricular filling dynamics using fluid-structure interaction finite element method. *Biophysical Journal*, 87(3):2074–2085, 2004.

[122] N. Westerhof, J.W. Lankhaar, and B.E. Westerhof. The arterial windkessel. *Medical & biological engineering & computing*, 47(2):131–141, 2009.

[123] J. Wong and E. Kuhl. Generating fibre orientation maps in human heart models using poisson interpolation. *Computer Methods in Biomechanics and Biomedical Engineering*, 17(11):1217–1226, 2014.

[124] F.C. Yin, C.C. Chan, and R.M. Judd. Compressibility of perfused passive myocardium. *American Journal of Physiology-Heart and Circulatory Physiology*, 271(5):H1864–H1870, 1996.

[125] Y. Zheng, A. Barbu, B. Georgescu, M. Scheuering, and D. Comaniciu. Fast automatic heart chamber segmentation from 3D CT data using marginal space learning and steerable features. In *International Conference on Computer Vision (ICCV)*, pages 1–8. IEEE, 2007.

[126] X. Zhuang, K.S. Rhode, R.S. Razavi, D.J. Hawkes, and S. Ourselin. A registration-based propagation framework for automatic whole heart segmentation of cardiac MRI. *IEEE Transactions on Medical Imaging*, 29(9):1612–1625, 2010.